Application of block copolymer thin film as a platform for electroless deposition and biosensor

by

Zeinab Harandizadeh

B.S., University of Esfahan, 2007
M.S., University of Esfahan, 2011

AN ABSTRACT OF A DISSERTATION

submitted in partial fulfillment of the requirements for the degree

DOCTOR OF PHILOSOPHY

Department of Chemistry
College of Arts and Sciences

KANSAS STATE UNIVERSITY
Manhattan, Kansas

2020

Abstract

This dissertation describes the applications of nanostructured thin films derived from diblock copolymers, polystyrene-block-poly(methylmethacrylate) (PS-*b*-PMMA) and polystyrene-block-poly(ethylene oxide) with a photocleavable ortho-nitrobenzyl ester (ONB) group (PS-*hv*-PEO). PS-*b*-PMMA was used to obtain nanostructured surfaces for testing silver electroless deposition (ELD) with novel sensitization solution, and to prepare gold electrodes coated with nanoporous thin films as platforms for stem-loop probe-based electrochemical DNA (E-DNA) sensors. For the ELD project, thin PS-*b*-PMMA films on silicon underwent thermal annealing at 190 ^{o}C under vacuum condition to induce microphase separation. The thin films were exposed to deep UV for degradation of PMMA and cross-linking of PS, and then washed with acetic acid and water to remove degraded PMMA. The efficiency of silver deposition was compared between nanoscale trenched and ridges obtained on the surfaces of the resulting films. In the E-DNA project, thin films with vertically-oriented nanopores were prepared on gold substrates in the same way as the ELD project except for the temperature for the thermal annealing (170 ^{o}C).

In the ELD project, our goal was to achieve a spatially controlled deposition of silver nanoparticles on nanostructured surfaces derived from PS-*b*-PMMA by ELD. We examined stannous acetate ($Sn(OAc)_2$) (0.5 mM) in dimethyl sulfoxide (DMSO) as a new sensitizer, and compared it with conventional aqueous stannous chloride ($SnCl_2$) ($\geq$ 5 mM). We hypothesized that Sn^{2+}, and thus silver nanoparticles, would be preferentially deposited on nanotrenches formed as a result of the removal of PMMA microdomains due to the higher density of surface -COOH group. However, AFM images revealed that silver nanoparticles were preferentially deposited on nanoridges originating from PS microdomains. The result indicated that silver deposition was controlled by the diffusion of Ag ions toward the surface. Sensitization with $Sn(OAc)_2$/DMSO was efficient at a low $Sn(OAc)_2$ concentration due to the reduction of Sn(II) hydroxide formation. In addition, the DMSO solution swelled the polymer, increasing the immobilization of Sn(II) at the polymer film.

In the E-DNA sensor project, we used PS-*b*-PMMA-derived thin films with vertical cylindrical nanopores to investigate the effects of DNA nanoconfinement on the performance of stem-loop probe-based E-DNA sensors. Gold substrates coated with PS-*b*-PMMA-derived thin nanoporous films (30 nm thick), as well as those without thin films were used as working electrodes. We evaluated the effects of pore size on the sensor performance by using thin films with uniform pore sizes (14, 20, 30 nm). The very thin film (30 nm) permitted counter ions to reach the bottom of the electrode easily, giving a reversible faradaic current in cyclic voltammetry (CV) measurements. The high pore density of these films (570–1220 pores/μm^2) let us immobilize a large number of probe DNA molecules on the electrode and thus record a high faradic current. The stem-loop DNA probe was labeled with a terminal methylene blue (MB) redox tag and immobilized onto the gold surface. The faradaic current of the MB decreased by the hybridization of the DNA probe with its target DNA, which was measured at different target concentrations and at different scan rates using CV to assess the hybridization efficiency and the electron transfer rate constant of the MB tag. We observed a current decrease at lower target concentrations for film-coated electrodes as compared with film-free electrodes, indicating the improvement of the limit of detection by electrode coating with a nanoporous film. This result was explained by the manipulated dynamic properties of the MB tag, as suggested by larger changes in its apparent electron transfer rate constant and/or enhanced hybridization within the nanopores. We also assessed the sensor performance in a whole cow blood sample. The sensors with thin film showed

smaller interference from redox-active components in whole cow blood, suggesting that the nanopores of the thin film sterically prevented the entry of relatively large interferents.

In the third project, we prepared vertically-oriented PEO microdomains in a thin PS-*hv*-PEO film on a gold substrate via solvent vapor annealing (benzene/H_2O for 3 h). The thin film was irradiated by UV light to photocleave the ONB group and then removed the cleaved PEO in methanol-water solution to obtain a thin film with cylindrical pores (pore diameter: 25 nm) with surface -COOH groups. Apparent -COOH density on the films before amidation was 0.30 ± 0.08 COOH/nm^2, which was lower than expected, suggesting that the pores did not reach the bottom of the thin film. Subsequently, amidation of the surface -COOH with propargylamine was explored using 1-ethyl-3-(3-dimethylaminopropyl) carbodiimide hydrochloride (EDC) and N-hydroxysuccinimide (NHS) in 4-(2-hydroxyethyl)-1-piperazineethanesulfonic acid (HEPES) buffer (0.1 M, pH 7). The maximum amidation yield obtained was 58-68%. We tried to increase the reaction yield by trying different amidation methods, but we could not attain the reaction yield higher than 68%. The amidated sample was examined for click reaction with Azide-fluor 545, but the immobilization of the fluorescent dye on the pore surface was unclear.

Application of block copolymer thin film as a platform for electroless deposition and biosensor

by

Zeinab Harandizadeh

B.S., University of Esfahan, 2007
M.S., University of Esfahan, 2011

A DISSERTATION

submitted in partial fulfillment of the requirements for the degree

DOCTOR OF PHILOSOPHY

Department of Chemistry
College of Arts and Sciences

KANSAS STATE UNIVERSITY
Manhattan, Kansas

2020

Approved by:

Major Professor
Dr. Takashi Ito

Copyright

Abstract

This dissertation describes the applications of nanostructured thin films derived from diblock copolymers, polystyrene-block-poly(methylmethacrylate) (PS-*b*-PMMA) and polystyrene-block-poly(ethylene oxide) with a photocleavable ortho-nitrobenzyl ester (ONB) group (PS-*hv*-PEO). PS-*b*-PMMA was used to obtain nanostructured surfaces for testing silver electroless deposition (ELD) with novel sensitization solution, and to prepare gold electrodes coated with nanoporous thin films as platforms for stem-loop probe-based electrochemical DNA (E-DNA) sensors. For the ELD project, thin PS-*b*-PMMA films on silicon underwent thermal annealing at 190 ^{o}C under vacuum condition to induce microphase separation. The thin films were exposed to deep UV for degradation of PMMA and cross-linking of PS, and then washed with acetic acid and water to remove degraded PMMA. The efficiency of silver deposition was compared between nanoscale trenched and ridges obtained on the surfaces of the resulting films. In the E-DNA project, thin films with vertically-oriented nanopores were prepared on gold substrates in the same way as the ELD project except for the temperature for the thermal annealing (170 ^{o}C).

In the ELD project, our goal was to achieve a spatially controlled deposition of silver nanoparticles on nanostructured surfaces derived from PS-*b*-PMMA by ELD. We examined stannous acetate ($Sn(OAc)_2$) (0.5 mM) in dimethyl sulfoxide (DMSO) as a new sensitizer, and compared it with conventional aqueous stannous chloride ($SnCl_2$) ($\geq$ 5 mM). We hypothesized that Sn^{2+}, and thus silver nanoparticles, would be preferentially deposited on nanotrenches formed as a result of the removal of PMMA microdomains due to the higher density of surface -COOH group. However, AFM images revealed that silver nanoparticles were preferentially deposited on nanoridges originating from PS microdomains. The result indicated that silver deposition was controlled by the diffusion of Ag ions toward the surface. Sensitization with $Sn(OAc)_2$/DMSO was efficient at a low $Sn(OAc)_2$ concentration due to the reduction of Sn(II) hydroxide formation. In addition, the DMSO solution swelled the polymer, increasing the immobilization of Sn(II) at the polymer film.

In the E-DNA sensor project, we used PS-*b*-PMMA-derived thin films with vertical cylindrical nanopores to investigate the effects of DNA nanoconfinement on the performance of stem-loop probe-based E-DNA sensors. Gold substrates coated with PS-*b*-PMMA-derived thin nanoporous films (30 nm thick), as well as those without thin films were used as working electrodes. We evaluated the effects of pore size on the sensor performance by using thin films with uniform pore sizes (14, 20, 30 nm). The very thin film (30 nm) permitted counter ions to reach the bottom of the electrode easily, giving a reversible faradaic current in cyclic voltammetry (CV) measurements. The high pore density of these films (570–1220 pores/μm^2) let us immobilize a large number of probe DNA molecules on the electrode and thus record a high faradic current. The stem-loop DNA probe was labeled with a terminal methylene blue (MB) redox tag and immobilized onto the gold surface. The faradaic current of the MB decreased by the hybridization of the DNA probe with its target DNA, which was measured at different target concentrations and at different scan rates using CV to assess the hybridization efficiency and the electron transfer rate constant of the MB tag. We observed a current decrease at lower target concentrations for film-coated electrodes as compared with film-free electrodes, indicating the improvement of the limit of detection by electrode coating with a nanoporous film. This result was explained by the manipulated dynamic properties of the MB tag, as suggested by larger changes in its apparent electron transfer rate constant and/or enhanced hybridization within the nanopores. We also assessed the sensor performance in a whole cow blood sample. The sensors with thin film showed

smaller interference from redox-active components in whole cow blood, suggesting that the nanopores of the thin film sterically prevented the entry of relatively large interferents.

In the third project, we prepared vertically-oriented PEO microdomains in a thin PS-*hv*-PEO film on a gold substrate via solvent vapor annealing (benzene/H_2O for 3 h). The thin film was irradiated by UV light to photocleave the ONB group and then removed the cleaved PEO in methanol-water solution to obtain a thin film with cylindrical pores (pore diameter: 25 nm) with surface -COOH groups. Apparent -COOH density on the films before amidation was 0.30 ± 0.08 COOH/nm^2, which was lower than expected, suggesting that the pores did not reach the bottom of the thin film. Subsequently, amidation of the surface -COOH with propargylamine was explored using 1-ethyl-3-(3-dimethylaminopropyl) carbodiimide hydrochloride (EDC) and N-hydroxysuccinimide (NHS) in 4-(2-hydroxyethyl)-1-piperazineethanesulfonic acid (HEPES) buffer (0.1 M, pH 7). The maximum amidation yield obtained was 58-68%. We tried to increase the reaction yield by trying different amidation methods, but we could not attain the reaction yield higher than 68%. The amidated sample was examined for click reaction with Azide-fluor 545, but the immobilization of the fluorescent dye on the pore surface was unclear.

.

Table of Contents

List of Figures

List of Tables

Acknowledgments

I would first like to declare my appreciation to my advisor, Professor Takashi Ito. He convincingly guided me to be a professional. His guidance helped me in all the time of research and writing of this thesis. Without his support, the goal of this dissertation would not have been realized and reached. The door of Prof. Ito's office was always open whenever I had a question about my research.

I would also like to acknowledge my Ph.D. committee members, Profs. Jun Li, Ryan Rafferty, and Keith Hohn. I am really grateful to them for their insightful comments and suggestions during my third-semester exam, preliminary exam, and final defense. I also thank Dr. Jocelyn McDonald for being the outside chairperson of my final defense presentation. My sincere thanks go to Prof. Hohn and Dr. Jingyi Xie for XPS measurements and analysis, Mikaela Moore for her help with Ag ELD on SAMs, Dr. Yi Yi (Indiana University, Bloomington) for providing PS-*hv*-PEO, and Prof. Rebecca Lai (University of Nebraska, Lincoln) for her suggestions on the selection of target and probe DNA. I had terrific lab-mates and friends. In particular, I appreciate Dr. Govinda Ghimire for teaching me how to operate the AFM instrument and Dr. Herman Coceancigh for teaching me some useful Excel tips and also for establishing an experimental setup for solvent vapor annealing in the PS-*hv*-PEO project. I am grateful to all the faculty and staff members of the Chemistry Department at Kansas State University, including Michael Hinton, Jim Hodgson, Ron Jackson, Tobe Eggers, Mary Dooley and Kimberly Ross, for their support and assistance.

I acknowledge the US Department of Energy (DE-SC0002362) for partial financial support of the Ag-ELD project, and the U.S. National Science Foundation (CHE-1709285) and the Terry

C. Johnson Center for Basic Cancer Research for financial support of the E-DNA sensor and PS-*hv*-PEO projects.

I must declare my profound gratitude to my parents, Asghar and Ferdows, and my husband, Mohammad Sadegh for providing me with unfailing support and continuous encouragement throughout my life and years of study. They were next to me when I need them and supported me spiritually. I could not reach this accomplishment without them. Last but not least, I am really grateful to have Zahra, my daughter, who has been the light of my life for the last two years. She has given me extra happiness and motivation to get things done.

Dedication

To my inspiring and caring parents, Asghar and Ferdows, my loving husband Mohammad Sadegh, and my little angel Zahra.

Chapter 1 - General Introduction

Our life is surrounded by polymers in the form of natural polymer or synthetic polymer. Natural polymers are made by nature, such as silk, wool, DNA, cellulose, natural rubber, natural lacquer, and starches. Also, there are tons of synthetic polymer which are manufactured in factories or laboratories, for example, nylon, polyethylene, polyester, Teflon, and epoxy resin, silicone. Block copolymers (BCPs) are one of the important categories of synthetic polymer which contain distinct monomer units that are covalently bonded together and make distinct blocks along the polymer chain. Nowadays, there is a considerable demand to prepare and use block copolymer self-assembling systems because they can form well-ordered structures with different morphology by controlling molecular parameters. Figure 1.1[1] shows the number of publications related to BCP between 1960 and 2017.

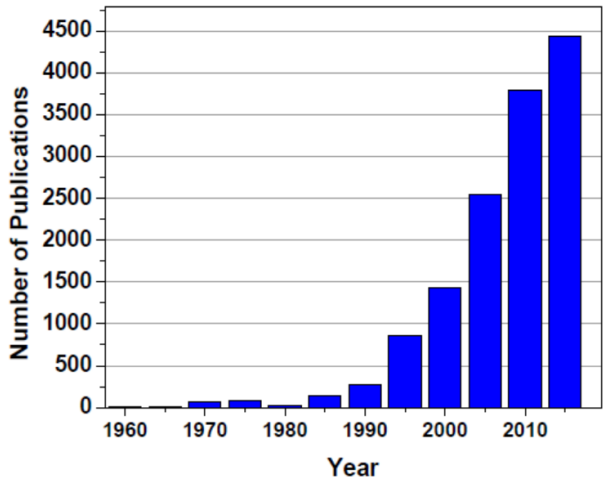

Figure 1.1: The number of published paper regarding BCPs over the past 5 decades[1]

Self-assembling block copolymers play an essential role in society and industry. They can be used as a separation membrane,[2] as a photovoltaic active layer,[3] as a mask for lithographic

applications,[4] as an anti-reflection coating,[5] in a biosensors technology,[6] and for drug delivery applications.[7] Block copolymers (BCP) can be used for selective deposition of metals to one of the blocks. Kamcev et al. reported the chemical modification of polystyrene-*block*-poly(methylmethacrylate) thin film and using this template for selective deposition of organometallic precursors.[8] This application was one of our motivations to chose PS-*b*-PMMA derived thin film for selective electroless deposition of silver nanoparticles on removed PMMA domains. As our group reported, removed PMMA domains have more -COOH density in comparison to PS domains.[9] We anticipated that Sn^{2+} will be deposited on PMMA domains (through chemical binding between Sn^{2+} and oxygen in -COOH group) more than PS domain and we could deposit silver nanoparticles on PMMA domains selectively. Block copolymers can be used at biosensor areas to prepare nanoelectrodes such as recessed nanodisk-array electrodes. Recessed nanodisk array electrodes have several advantages over other electrodes. It can increase mass transport of interested molecule toward electrode which results in amplification of faradaic current, increasing of sensitivity, decreasing of the limit of detection, increasing of signal to noise ratio, and reduction of the ohmic drop.[10–13] PS-*b*-PMMA derived thin films were good candidates to prepare recessed nanodisk array electrodes for biosensor application due to having adjustable vertical cylindrical pores. Also, thin film thickness can be reached to the nm scale (30 nm), which helps to mass transport of DNA molecules toward the underlying electrode. PS-*b*-PMMA derived thin films can also act as a size-exclusive filter[14] in electrochemistry. We took advantage of this property of PS-*b*-PMMA derived thin films to make a sensor for the measurement of interested target molecules in an undiluted blood sample. Those were our motivation to design and conduct the second project. Polystyrene-*block*-poly(ethylene oxide) is another block copolymer which is selected in this dissertation. This block copolymer with a photocleavable ortho-nitrobenzyl ester

(ONB) group was used to prepare PS-*hv*-PEO derived thin film. Gamys et al. synthesized PS-*hv*-PEO with ONB groups.[15] They prepared polymer thin film and used solvent annealing in benzene/water vapor for 4 h. Then they exposed thin film to UV light (λ= 300 nm). The prepared thin film with vertical cylindrical pore had amine group attached to the pore wall. This thin film was used to immobilize Coumarin 343, (a fluorescent dye) inside pore. Inspired by this study, we designed a project to used another PS-*hv*-PEO with ONB groups to prepare well order thin film with vertical cylindrical pores via solvent annealing. We anticipated to have -COOH group attached to the wall after exposing the thin film to UV irradiation. This thin film could undergo amidation reaction to functionalize the nanopore surface. The final step was to immobilize dye molecules to the wall via click reaction.

This dissertation is composed of seven chapters. The first chapter describes a general introduction and the motivation of projects, followed by the dissertation outline. The second chapter summarizes backgrounds on copolymer structure, block copolymer self-assembly, and methods used to prepare their thin film. The structures of polystyrene-*block*-polymethylmethacrylate (PS-*b*-PMMA) and polystyrene-*block*-poly(ethylene oxide) (PS-*b*-PEO) are briefly explained. Another part of this chapter describes electroless deposition method and electrochemical biosensors. The third chapter describes all of the characterization methods used in the thesis studies, including spectroscopic ellipsometry, atomic force microscopy (AFM), X-Ray photoelectron spectroscopy (XPS), fluorescence spectroscopy and cyclic voltammetry. The fourth chapter describes the first project regarding silver electroless deposition on PS-*b*-PMMA derived thin film using $Sn(OAc)_2$/DMSO as a sensitizer solution. The fifth chapter describes the second project in which PS-*b*-PMMA derived thin nanoporous film was used as a platform for stem-loop probe-based electrochemical DNA sensors. The sixth chapter describes the third project which

aims to characterize nanoporous thin films from photocleavable polystyrene-*b*-poly(ethylene oxide). The seventh chapter is about the general conclusion of three projects and possible future directions.

Reference

(1) Feng, H.; Lu, X.; Wang, W.; Kang, N.-G.; Mays, J. W. Block Copolymers: Synthesis, Self-Assembly, and Applications. *Polymers* **2017**, *9* (10), 494. https://doi.org/10.3390/polym9100494.

(2) Zhang, Y.; Almodovar-Arbelo, N. E.; Weidman, J. L.; Corti, D. S.; Boudouris, B. W.; Phillip, W. A. Fit-for-Purpose Block Polymer Membranes Molecularly Engineered for Water Treatment. *npj Clean Water* **2018**, *1* (1), 1–14. https://doi.org/10.1038/s41545-018-0002-1.

(3) Mitchell, V. D.; Jones, D. J. Advances toward the Effective Use of Block Copolymers as Organic Photovoltaic Active Layers. *Polym. Chem.* **2018**, *9* (7), 795–814. https://doi.org/10.1039/C7PY01878A.

(4) Ferrarese Lupi, F.; Giammaria, T. J.; Volpe, F. G.; Lotto, F.; Seguini, G.; Pivac, B.; Laus, M.; Perego, M. High Aspect Ratio PS-b-PMMA Block Copolymer Masks for Lithographic Applications. *ACS Appl. Mater. Interfaces* **2014**, *6* (23), 21389–21396. https://doi.org/10.1021/am506391n.

(5) Joo, W.; Kim, H. J.; Kim, J. K. Broadband Antireflection Coating Covering from Visible to Near Infrared Wavelengths by Using Multilayered Nanoporous Block Copolymer Films. *Langmuir* **2010**, *26* (7), 5110–5114. https://doi.org/10.1021/la9035858.

(6) Guo, T.; Gao, J.; Qin, X.; Zhang, X.; Xue, H. A Novel Glucose Biosensor Based on Hierarchically Porous Block Copolymer Film. *Polymers (Basel)* **2018**, *10* (7). https://doi.org/10.3390/polym10070723.

(7) Rösler, A.; Vandermeulen, G. W. M.; Klok, H.-A. Advanced Drug Delivery Devices via Self-Assembly of Amphiphilic Block Copolymers. *Advanced Drug Delivery Reviews* **2001**, *53* (1), 95–108. https://doi.org/10.1016/S0169-409X(01)00222-8.

(8) Kamcev, J.; Germack, D. S.; Nykypanchuk, D.; Grubbs, R. B.; Nam, C.-Y.; Black, C. T. Chemically Enhancing Block Copolymers for Block-Selective Synthesis of Self-Assembled Metal Oxide Nanostructures. *ACS Nano* **2013**, *7* (1), 339–346. https://doi.org/10.1021/nn304122b.

(9) Li, F.; Diaz, R.; Ito, T. Quantitative Investigation of Surface Functionalization of Cylindrical Nanopores Derived from Polystyrene-Poly(Methylmethacrylate) Diblock Copolymers. *RSC Adv.* **2011**, *1* (9), 1732–1736. https://doi.org/10.1039/C1RA00471A.

(10) Huang, X.-J.; O'Mahony, A. M.; Compton, R. G. Microelectrode Arrays for Electrochemistry: Approaches to Fabrication. *Small* **2009**, *5* (7), 776–788. https://doi.org/10.1002/smll.200801593.

(11) M. Arrigan, D. W. Nanoelectrodes, Nanoelectrode Arrays and Their Applications. *Analyst* **2004**, *129* (12), 1157–1165. https://doi.org/10.1039/B415395M.

(12) Bond, A. M.; Luscombe, D.; Oldham, K. B.; Zoski, C. G. A Comparison of the Chronoamperometric Response at Inlaid and Recessed Disc Microelectrodes. *Journal of*

Electroanalytical Chemistry and Interfacial Electrochemistry **1988**, *249* (1), 1–14. https://doi.org/10.1016/0022-0728(88)80345-0.

(13) Ito, T.; Audi, A. A.; Dible, G. P. Electrochemical Characterization of Recessed Nanodisk-Array Electrodes Prepared from Track-Etched Membranes. *Anal. Chem.* **2006**, *78* (19), 7048–7053. https://doi.org/10.1021/ac061043m.

(14) Ito, T.; Ghimire, G. Electrochemical Applications of Microphase-Separated Block Copolymer Thin Films. *ChemElectroChem* **2018**, *5* (20), 2937–2953. https://doi.org/10.1002/celc.201800576.

(15) Gamys, C. G.; Schumers, J.-M.; Vlad, A.; Fustin, C.-A.; Gohy, J.-F. Amine-Functionalized Nanoporous Thin Films from a Poly(Ethylene Oxide)-Block-Polystyrene Diblock Copolymer Bearing a Photocleavable o-Nitrobenzyl Carbamate Junction. *Soft Matter* **2012**, *8* (16), 4486–4493. https://doi.org/10.1039/C2SM07056A.

Chapter 2 - Background

A layer of material with a thickness range from a nanometer to several micrometers is defined as a thin film. Thin films have different properties comparing bulk material because their properties depend on their deposition method and the number of interrelated parameters. Thin films have several industrial applications, including as a protective layer,[1] conductive layers,[2] photoactive layers,[3] gas separation membranes,[4] and optical layers.[5] Thin films can be used in biomedicine to improve the adhesion and proliferation of specific eukaryotic cells,[6] and tailoring of biomaterials surfaces.[7] Polymer thin films are one of the important categories of thin film that can be found anywhere such as adhesives, packaging, paints, electronic device, sensors, separation membranes for fuel cell, electrodes in batteries.[8]

In this research, two block copolymers, polystyrene-*block*-poly(methylmethacrylate) (PS-*b*-PMMA) and photocleavable polystyrene-*block*-poly(ethylene oxide) PS-*hv*-PEO, were used. We used PS-*b*-PMMA to make thin-films with horizontal nanoscale trench structures of uniform widths and those with vertical cylindrical nanopores with uniform pore sizes by removing cylindrical PMMA microdomains. The former films were used as substrates to demonstrate a DMSO solution of $Sn(OAc)_2$ as a new sensitizer for electroless deposition of silver nanoparticles. We hypothesized that the use of the nanostructured surfaces helped us to obtain silver nanoparticles with the desired size and morphology. Also, silver nanoparticles on the horizontal nanostructures can be measured using AFM. The latter films with vertical nanopores were used as platforms for folding-based electrochemical DNA (E-DNA) sensors based on stem-loop probe DNA. Here, the sensor performance was compared for three different films of different pore diameters. PS-*hv*-PEO, which is polystyrene-*block*-poly(ethylene oxide) (PS-*b*-PEO) with a photocleavable *o*-nitrobenzyl ester junction, was used to evaluate the physical environment of

nanopores obtained after removing PEO microdomains on chemical recognition with anion receptor. I tried to investigate the chemistry of the nanopore surface, including the determination of surface -COOH density, the assessment of amidation efficiency, and the demonstration of click reaction on alkyne-modified nanopore surfaces.

2.1. Copolymer[9]

A copolymer is a polymer that contains two or more different types of monomers (for example, A and B). When one type of monomer is polymerized and made up a macromolecule, the macromolecule is called a homopolymer (Figure 2.1.1). When the two or more monomers (for instance A and B) are involved in building up a polymer, the macromolecule is called a copolymer. Based on monomer arrangement, four different copolymers can be synthesized, including random copolymer, alternating copolymer, graft copolymer, and block copolymer. In a random copolymer, the two monomers may follow any random distribution of the monomers, as shown in Figure 2.1.2 When Monomer A and Monomer B are arranged in an alternating fashion along the polymer chain, they produce an alternating copolymer (the ratio of Monomers A and B is 1:1), as depicted in Figure 2.1.3. When Monomer B made up a chain by incorporated together and then is grafted onto a polymer chain of Monomer A, the copolymer is called graft copolymer (Figure 2.1.4). A copolymer is made up of uninterrupted sequences of each Monomers A and B called block copolymer (BCP), as shown in Figure 2.1.5.

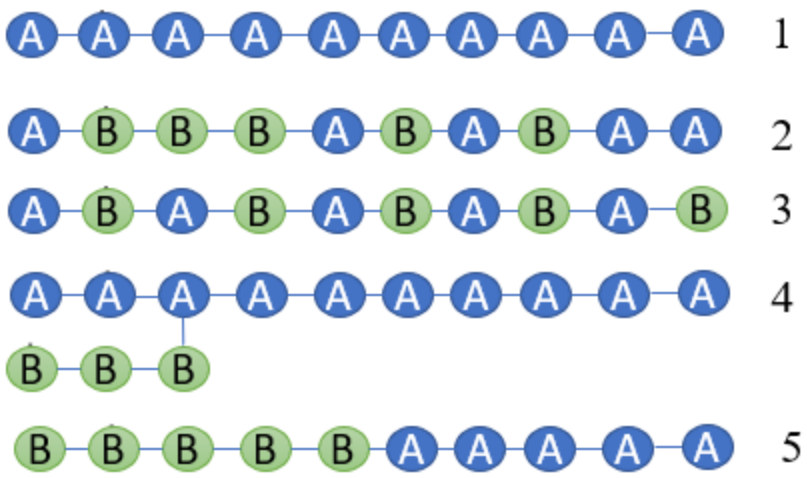

Figure 2.1: Structures of the different types of polymers.

2.1.2. Block Copolymer Self Assembly

Nowadays, block copolymers are an essential aspect of polymer science due to their applications in diverse scientific and technological areas. They can be used for membrane filtration,[10–12] for heterogeneous catalysis,[13] as photovoltaic materials,[14,15] as chemical sensors,[16] as templates for the formation of nanomaterials with favorable size and shapes,[10,17] and masks for lithographic applications.[18,19] Block copolymers are a class of polymers with two or more different homopolymers connected end to end covalently.[20] If a block copolymer possesses two different homopolymers, it is called diblock copolymer. If three different blocks make a block copolymer, then it considers as a triblock copolymer. If microphase separation occurs between different polymer segments, microdomains of a certain morphology with uniform size (10-100 nm) are formed.[20,21] The morphology is controlled by the volume fraction of one block (f) and repulsion interaction strength of different blocks, which is represented by χN. Here, χ is the Flory-Huggins segmental interaction parameter (proportional to the unfavorable interactions between different blocks and inversely proportional to temperature), and N is the total number of repeating units (the

degree of polymerization).[22–24] Different theories were developed to predict the microdomain structures. In the 1970s, Helfand and Wasserman explained the phase behaviors of a BCP with a strong segregation limit ($\chi N > 100$) using self-consistent field theory (SCFT), which considered the stretching and conformation of the polymer chain.[25–27] Then, the SCFT theory was extended for a weak segregation limit ($\chi N < 10$).[28] Finally, mean field theory (MFT) was developed by unifying the weak and strong segregation theories and adding $10 < \chi N < 100$ regime. Therefore, MFT can cover all range of χN from $\chi N < 10$, $10 < \chi N < 100$ to $\chi N > 100$.[29] According to MFT, the phase behavior of a linear diblock copolymer depends on χN and f, as depicted in Figure 2.2.[30] Under thermodynamic equilibrium, linear diblock copolymers form different morphologies including spherical (S), cylindrical (C), gyroid (G) and lamellar (L) (Figure 2.2). [30] The phase diagram can be used to estimate a microdomain morphology from a synthesized linear diblock copolymer. Spherical microdomains will be obtained from a linear diblock copolymer with f_A of 0.1 – 0.2 and cylindrical morphology can be obtained when f_A is 0.3 – 0.4. Temperature (T) is one of the parameters which can affect BCP phase separation due to effect on χ according to Equation 2.1.[31]

$$\chi = A + B/T \qquad (eq.2.1)$$

where A and B are constants. Equation 2.1 shows a decrease in χ at higher T. When χN becomes sufficiently small, the BCP cannot stay phase-separated and undergo an order to disorder transition (ODT).

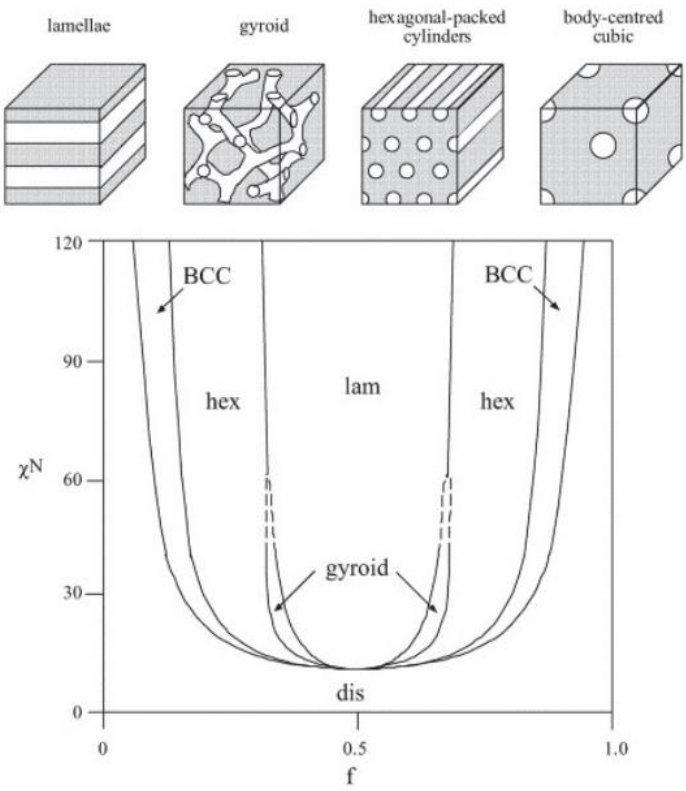

Figure 2.2: Phase diagram for linear AB diblock copolymers. Calculated using self-consistent mean-field theory: spherical, cylindrical, gyroid, and lamellar. Adapted with permission from ref (30), Copyright © 2005 Elsevier Ltd.

2.2. Preparation of Block Copolymer Thin Films[32]

Thin films of a BCP show different phase behaviors in a comparison with its bulk materials because of interfacial interactions, confinement effects between substrate/polymer, and air/polymer interface. In order to utilize BCPs in the fabrication of nanostructures, a thin film of a BCP must be deposited on a substrate. Deposition of the thin BCP film on the substrate can be done using different methods, including drop-casting, dip-coating, and spin-coating. In the drop-casting, a BCP is dissolved in an appropriate solvent then a solution drop is placed on the substrate and let the drop to dry. An obtained film is non-uniform, which is the remarkable drawback of this method. In the dip-coating, the substrate surface is covered by a BCP solution by dipping the substrate into the BCP solution. In the next step, the sample covered by the BCP solution is pulled up and let solvent to evaporate. This method is useful for generating thickness gradients and for

preparing a thin film of a vast area. Here, three critical parameters, including withdraw speed, temperature, solvent volatility, can affect in the generation of thickness gradients. The most common method for fabricating a thin BCP film on a substrate is spin-coating, in which drops of BCP solution are placed on the top of the substrate and spun at high speed (1000-5000 rpm), causing excess solution to flow off the substrate.[33] In this method, film thickness depends on the spinning velocity, a concentration of the polymer solution, molar mass, and molar mass distribution of the BCP.[34] When the solvent evaporates fast, the BCP chain goes into a nonequilibrium, disorganized state. Therefore, spin-coating speed should be controlled carefully.[35]

The resulting thin film is annealed, either by heating or by solvent vapor treatment, to increase the mobility of the polymer chains and to produce a well-ordered morphology based on the microphase separation of the BCP. In the thermal annealing method, a thin BCP film is heated at a temperature above the glass transition temperature (T_g) of both blocks for a required time. The heating is carried out under vacuum condition or inert atmosphere to avoid any undesired chemical reactions.[36] This annealing method is not effective for BCPs with high χ or high molar mass, and the heating of BCPs is needed for an extended period of time. In 1998, the solvent vapor annealing (SVA) was reported for the first time by Albalak et al to improve the long-range order of polystyrene-polybutadiene-polystyrene triblock copolymers.[37] The method got famous when the Russell group used it. They applied SVA using THF as a solvent for PS-*b*-PEO to form highly ordered hexagonally packed PEO microdomains.[38] For SVA, a thin BCP film on the substrate is exposed to the solvent vapor at a temperature below the glass transition temperature of both blocks. Solvent vapor permeates the polymer domains and leads to swelling of the film due to thermodynamic driving forces correlated with the mixing entropy and dilution of the unfavorable

interfaces between segments. SVA time required to get BCP swollen is determined by mass transport of solvent into the thin film.[39]

Solvent vapor acts as a plasticizer and enhances BCP chain mobility dramatically to reduce T_g.[40] Also, trapping of solvent inside a thin BCP film causes dilution of the polymer chains and decreasing of the interaction parameter (χ).[41] The selection of the solvent for SVA is the main factor to be considered because of the interactions between the molecules, the substrate, and the solvent. The excellent solvent is the one that has a higher affinity toward one of the blocks. Guo et al. reported obtaining different microdomain morphologies of blended thin films of two poly(styrene-*b*-butadiene) (PS-*b*-PB, Table 2.1) using three different SVA solvents.[42] Spheres-between-cylinders morphology was obtained using cyclohexane as a solvent. The spherical PB domains were obtained when benzene was used as a solvent. Finally, the morphology of the in-plane cylindrical and spherical PS domains in the PB matrix was observed by choosing heptane as a solvent. Heptane is selective to the PB segment, while cyclohexane shows preferential affinity toward the PB segment. Benzene has preferential affinity toward the PS segment (Figure 2.3).[42] SVA is more useful for high molecular weight BCPs in comparison to thermal annealing. Also, it can help to decrease the annealing time.[40]

Table 2-1: Properties of different PS-*b*-PB

sample	$M_{n,PS}{}^{a} \times 10^{-3}$ (Da)	$M_{n,PB}{}^{a} \times 10^{-3}$ (Da)	N^{b}	$w_{PS}{}^{c}$	$f_{PS}{}^{d}$	M_w/M_n
S_1B_1	37.3	99.8[e]	2207	0.272[f]	0.241	1.002
S_2B_2	63.5	33.0	1222	0.658	0.621	1.09

[a] M_n is the average molecular weight of the PS or PB. [b] N, is the polymerization degree of the diblock. [c] w_{PS}, weight fraction of PS. [d] f_{PS}, PS block volume fraction. Adapted with permission from ref (42), Copyright © 2008, American Chemical Society

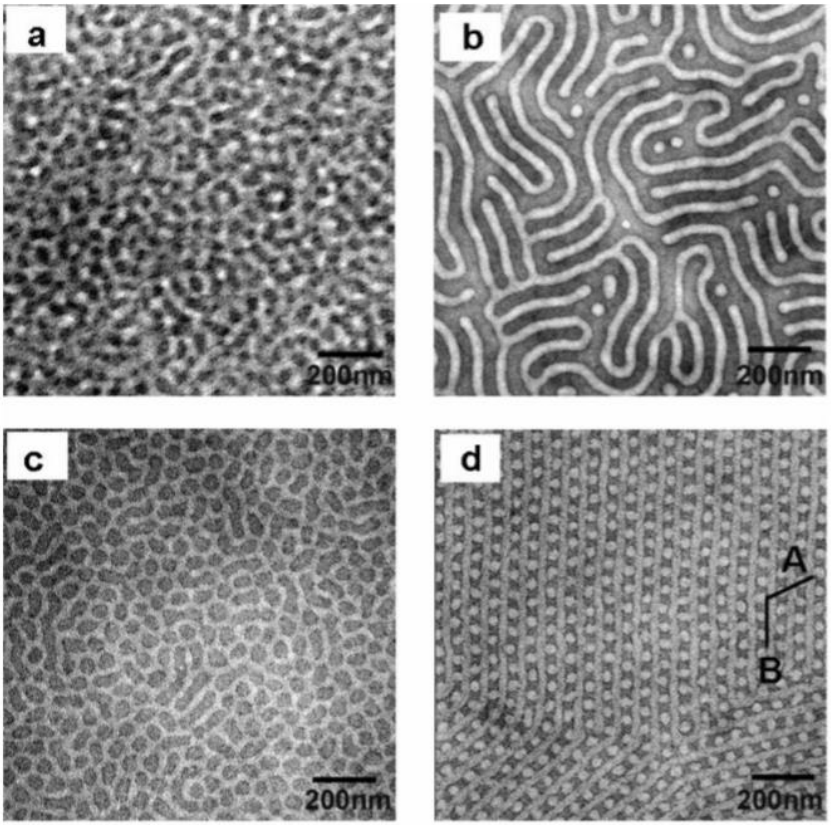

Figure 2.3: TEM morphologies of the spin-coated S_1B_1/S_2B_2 (50/50) blend thin films. (a) An as-cast film. After SVA for 12 h in the saturated vapor (b) heptane; (c) benzene; (d) cyclohexane. Adapted with permission from **r**ef (42), Copyright © 2008, American Chemical Society

In this thesis, we used a spin-coating method to obtain a very uniform and homogenous film, which is a remarkable advantage of this method. Also, this method helps us to prepare a thin film of desired thickness. The thermal annealing technique was used to prepare thin PS-*b*-PMMA films with vertical and horizontal cylindrical PMMA microdomains. The SVA method was used to prepare thin PS-*hv*-PEO films with vertical cylindrical domains because PS-*hv*-PEO is sensitive to thermal degradation.[43] In contrast, PS-*b*-PMMA can tolerate thermal annealing in a range of ~ 100 ^{o}C to ~ 250 ^{o}C.[44]

2.2.1. Properties of PS-*b*-PMMA

Polystyrene-*block*-polymethylmethacrylate (PS-*b*-PMMA) has been used most widely among BCPs due to its properties, because those having different molecular weights with narrow molecular weight distributions of each block are commercially available, and because its PMMA can be degraded selectively. In addition, the similar surface energies of PS and PMMA helps to control domain orientation.[43]

The chemical structure of PS-*b*-PMMA is shown in Figure 2.4. It is built from polystyrene (PS) and polymethylmethacrylate (PMMA) as two different polymer segments.[45]

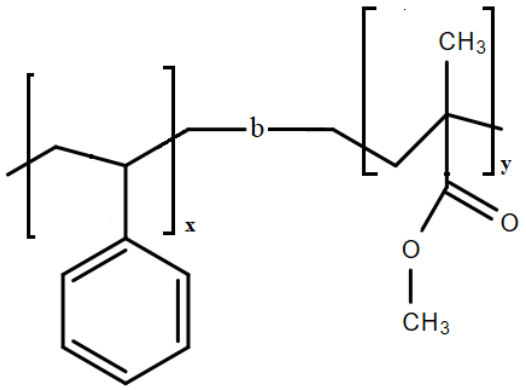

Figure 2.4: Chemical structure of PS-*b*-PMMA.

PS-*b*-PMMA usually undergoes thermal annealing at temperatures between 160 ^{o}C and 250 ^{o}C, which is above the glass transition temperature of PS (100 ^{o}C) and the glass transition temperature of PMMA (115 ^{o}C).[46] The resulting BCP films are treated by wet etching (with chemicals) or dry etching by plasma to remove one of the polymer segments. The most common method used to remove PMMA domains from thin PS-*b*-PMMA film is an exposure of the thin film to deep UV light following by immersing the thin film in acetic acid. This method is called a

wet etching method.[47] The photodegradation properties of PS and PMMA are entirely different. PMMA segments undergo chain scission, and polymer degradation occurs as soon as exposed to deep UV irradiation.[48] PS domains experience cross-linking (leads to increase in the insolubility of the PS segment), chain scission, and oxidation due to exposure to UV irradiation.[48] However, under optimizing condition, cross-linking can dominate for PS.[49] Russell's group applied 25 J/cm^2 deep UV irradiation for degradation of PMMA domains and then removed PMMA domains using acetic acid to obtain cylinder morphology as shown in Figure 2.5.[49] They used Si substrate and coated the substrate with a random copolymer. The random copolymer had 0.6 fraction of styrene. They considered this surface as a neutral surface.

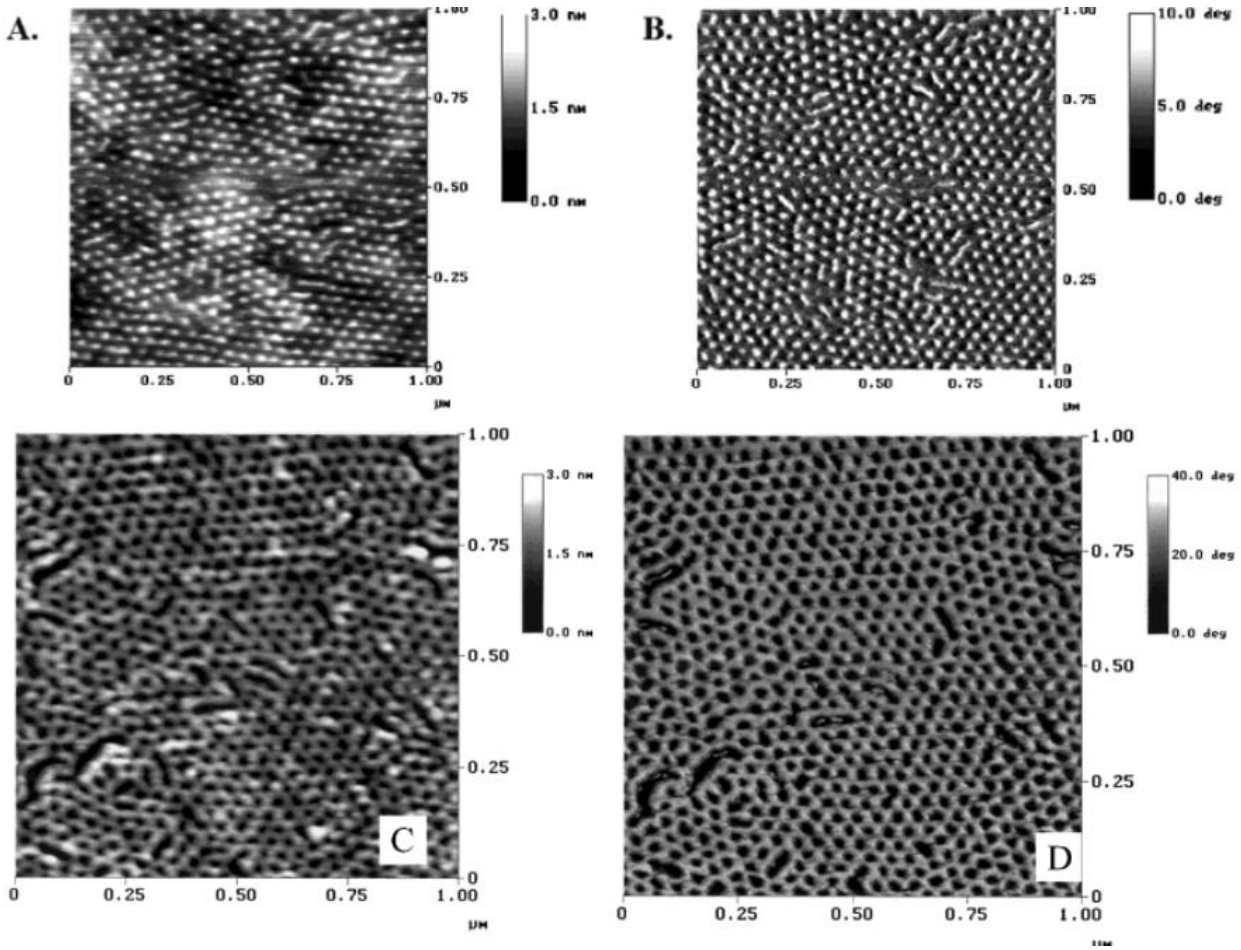

Figure 2.5: Tapping mode AFM (a) height and (b) phase images obtained from a thin film (40 nm) of PS-*b*-PMMA on a neutral substrate (after annealing at 170 ^{o}C). (c) Height and (d) phase

images of the film after removal of the PMMA, which show cylindrical pores. Adapted with permission from ref (49), Copyright © 2000 Wiley

The χ value of PS-*b*-PMMA is 0.043 (at room temperature) and has a weak dependence on temperature. It means ODT is very small for this polymer. Knowing χ helps to control microphase separation and the physical properties of a polymer.[44] The A and B parameters in equation 2.1 are -0.6577 and 3942, respectively, according to equation 2.2.[50]

$$N\chi_F = -0.6577 + 3942.1/T \qquad \text{eq.2.2}$$

.

2.2.2. Properties of PS-*b*-PEO

Polystyrene-*block*-poly(ethylene oxide**) (**PS-*b*-PEO) has drawn much attention because it forms vertical cylindrical domains from the surface to the bottom of the thin film using solvent vapor annealing.[51,52] Solvent vapor annealing can be performed using the vapor of one single solvent or mixture of two solvents at room temperature in a closed chamber for a specific time.[53] However, it is not easy to remove PEO domains selectively from a well-ordered PS-*b*-PEO film. For removing the PEO segment selectively, harsh chemicals such as HI[54] or synthesis of triblock copolymers such as PS-*b*-PMMA-*b*-PEO is needed.[55] The other way to remove PEO segment is to insert a photocleavable linker such as *o*-nitrobenzyl ester moiety between PS and PEO segments to make PS-*hv*-PEO. The *o*-nitrobenzyl ester in PS-*hv*-PEO can be cleaved under 365nm UV light. The PEO segment can be extracted in a methanol-water mixture to obtain nanoporous thin film.[56]

The chemical structure of PS-*b*-PEO is shown in Figure 2.6.[43] Two segments of this block copolymer are PS (one glassy block) and PEO (rubbery block). PS segment is water-insoluble, while PEO is water-soluble. Phase separation can be performed by taking advantage of this difference. The χ value of PS-*b*-PEO is ~ 0.077 (at room temperature), which consider as a high Flory–Huggins parameter.[43]

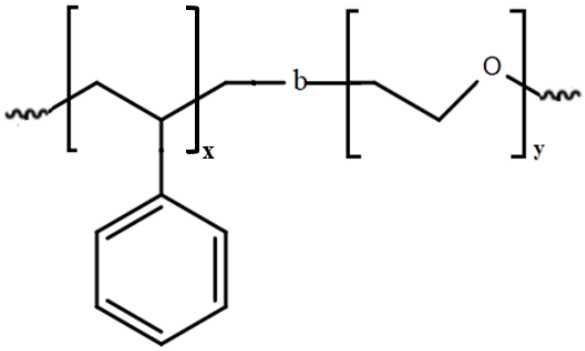

Figure 2.6: Chemical structure of PS-*b*-PEO

2.3. Electroless Deposition

Electroless deposition has been used to produce mirrors by forming a thin silver film on glass for decades.[57] Electroless metal deposition on surfaces is very efficient. Therefore, the nanotechnology researcher decided to use this method for metal deposition on small complicated geometries that cannot be covered using a vapor deposition method.[58] Electroless deposition was applied to metalize interior surfaces of microstructured optical fibres,[59] to fabricate surface-enhanced Raman scattering surface,[60] and surface plasmon resonance sensors.[61] Electroless deposition method can be defined as an autocatalytic deposition of a uniform and continuous layer of metal on a surface. In this method, metal ions (as complex compounds) are reduced on catalytic metal particles immobilized on a sample surface by a reducing agent. Electron transfer from the reducing agent to metal ions should be slow; otherwise, metal ions are reduced to the metal in bulk solution instead of on the surface. The electroless deposition bath contains a metal salt, a complexing agent, a reducing agent, a sensitizer, and a solvent. The complexing agent is added to the bath to stabilize the metal ion to get homogenous deposition after adding the reducing agent. The reaction mechanism in ELD can be explained based on a combination of two reactions. One

of the reactions is the reduction of the metal ion, and the second one is the oxidation of the reducing agent. Both reactions are shown below:[62]

$$M^{n+} + ne \longrightarrow M$$
$$R \longrightarrow O + ne$$

This method needs several steps, including substrate cleaning, sensitization, activation, ELD, substrate rinsing, and substrate drying.[63] The sensitization and activation steps are very important steps because these steps help to enhance the rate of metal ion reduction on the surface.[64] In the sensitization step, Sn^{2+} ions are immobilized on the substrate surface. Anchored Sn^{2+} ions serve as a reducing agent for the activation step. In the activation step, nanometal islands are formed on the surface due to the reduction of M^{n+} to M^0 via oxidation of Sn^{2+} to Sn^{4+}. These nanometal islands serve as a catalytic site on the surface for the ELD step. In the ELD step, metal ions are reduced to metal by the reducing agent.[65]

This method does not need to use any complicated or expensive instrument and an external power source. The method can be applied for conductive or nonconductive surfaces such as plastic[66] and track-etched membranes.[67] Electroless deposition of different metals was reported, including nickel,[68,69] palladium,[60] gold,[70] platinum,[70] silver,[71,72] copper,[73,74] iron,[75] and cobalt.[76] Here we focused on the silver electroless deposition. A silver electroless deposition method has been widely used to coat a glass surface with a silver layer. First, a glass substrate was cleaned by acetone and alcohol to remove any grease and contaminants from its surface. Then the cleaned glass substrate was immersed in a sensitization solution containing $SnCl_2$. Sn^{2+} adsorbed on the surface of the glass. The adsorbed Sn^{2+} reduces Ag^+ to give metallic silver particles on the glass substrate. The reaction between Sn^{2+} and Ag^+ is shown below.[62]

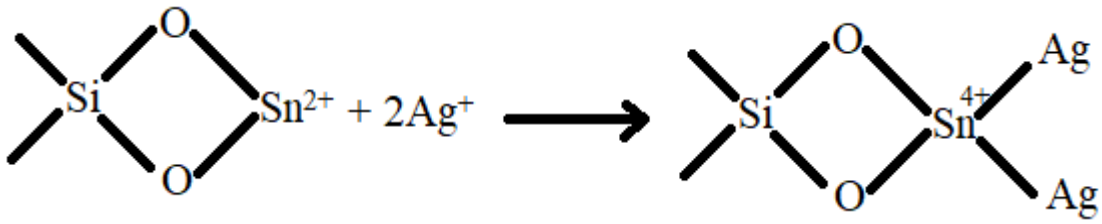

The metallic silver particles act as a catalyst for the reduction of silver ions after adding a reducing agent to an ELD bath. This silver ELD method on glass can be generalized to other surfaces. For example, Kobayashi et al. used sensitization and activation steps to deposit silver nanoparticles on silica colloid. For this purpose, they added $SnCl_2$ and CF_3COOH to silica colloids in a mixture of water/methanol solution. $SnCl_2$ in acidic solution acted as a sensitizer and Sn^{2+} attached to SiO_2 surface. Then an ammoniacal $AgNO_3$ solution was added to a solution containing sensitized SiO_2 colloids. Metallic Ag was deposited on the colloidal SiO_2 as a result of the reduction of Ag^+ ions by the attached Sn^{2+}(Figure 2.7).[77] The Ag deposition step can be repeated to get desired deposited nanoparticles on colloidal SiO_2.

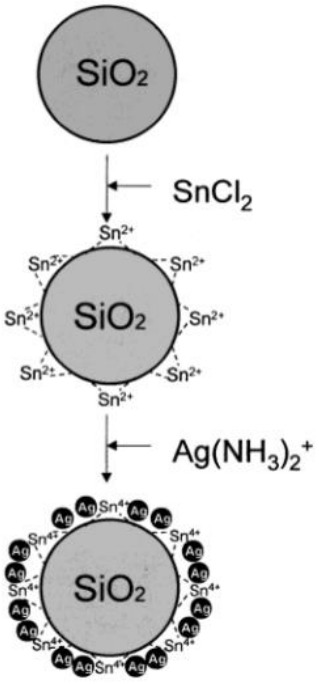

Figure 2.7: Sensitization and activation step for deposition of silver nanoparticles on colloidal SiO_2. Adapted with permission from Ref (76), Copyright © 2001, American Chemical Society

Several reducing agents, including glucose,[78] hydrazine-hydrate,[79] sodium potassium tartrate,[80] dimethylamino borane,[81] and formaldehyde[82] were selected for silver ELD. The selection of a reducing agent should be made very carefully because the metal deposition rate depends on the type of reducing agent. For instance, the deposition rate is fast using formaldehyde which leads to the formation of cloudy metal film on the substrate which can be peeled.[62]

2.4. Electrochemical DNA Biosensor

2.4.1 DNA Molecule

Deoxyribonucleic acid (DNA) structure was specified in 1953.[83] DNA molecule is an organic compound made up of nucleotides that covalently bound together. A DNA molecule includes two long polynucleotide chains called DNA strands, which are connected through hydrogen bonds. The structure of a nucleotide includes a sugar molecule called deoxyribose, a phosphate group, and one of the nitrogen bases. The nitrogen bases can be adenine (A), thymine (T), cytosine (C), and guanine (G). Sugar and phosphate make the backbone of a DNA molecule.[83] Figure 2.8 shows the structure of a DNA molecule in the form of three-dimensional structure called double helix.[84]

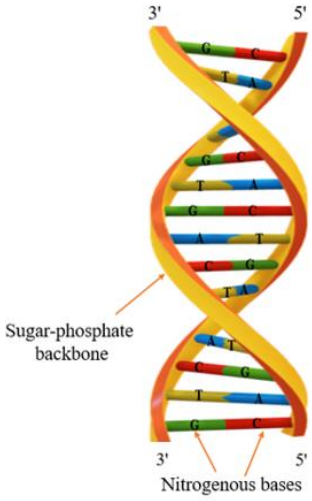

Figure 2.8: DNA structure. In the form of double helix.

DNA molecules have different nucleotide order; therefore, each DNA molecule can carry different biological information. The human DNA sequence undergoes mutation during life because of radiation, viruses, mutagenic chemicals, etc. Some of the mutations lead to serious diseases such as different types of cancers. It is very important to get a better knowledge of the effect of the mutation on human life. One of the tools which can help to get better knowledge about these mutations is biosensors based on DNA, RAN and peptide nucleic acids. These molecules bind to target molecules with a complementary base sequence. DNA biosensors are rapid and sensitive sensor to detect genetic disease.[85]

2.4.2. Electrochemical DNA Biosensor

Biosensors are analytical devices that attracted lots of attention over the past decades due to their vast applications. They can be used for clinical diagnosis,[86] food and environmental quality control,[87] forensic chemistry,[88] and agricultural industry.[89] Clark and Lyons developed the first glucose oxidase biosensor in 1962 to measure glucose.[90] There are different kinds of biosensors

including electrochemical biosensor,[91] optical biosensor,[92] piezoelectric biosensors[93,94] and thermal biosensor.[95] Figure 2.9[91] shows the main elements of a biosensor, which translates biological response into an electrical signal. The main elements include three parts: The first element is a sensitive biological sensor called bioreceptor (single-strand DNA, RNA, antibodies, enzymes, tissue, cell receptor, …). The second component is a transducer (detector). A transducer converts one form of signal to another readable form. The transducer changes the signal, which comes from the interaction of the analyte with a bioreceptor to the physicochemical response such as an optical signal, piezoelectric signal, electrochemical signal, electrochemiluminescence response, etc. The third part is associated electronics (amplifier, processor and a display unit).[91] First, the bioreceptor elements are immobilized on the sensor surface by physical adsorption (van der Waals forces, electrostatic interaction, etc.), covalent binding, matrix entrapment and membrane entrapment.[96,97] Second, the immobilized bioreceptors capture analytes. The bound analytes generate a signal which can be translated to an electrical signal that is readable by electronic component (Figure 2.10).[98]

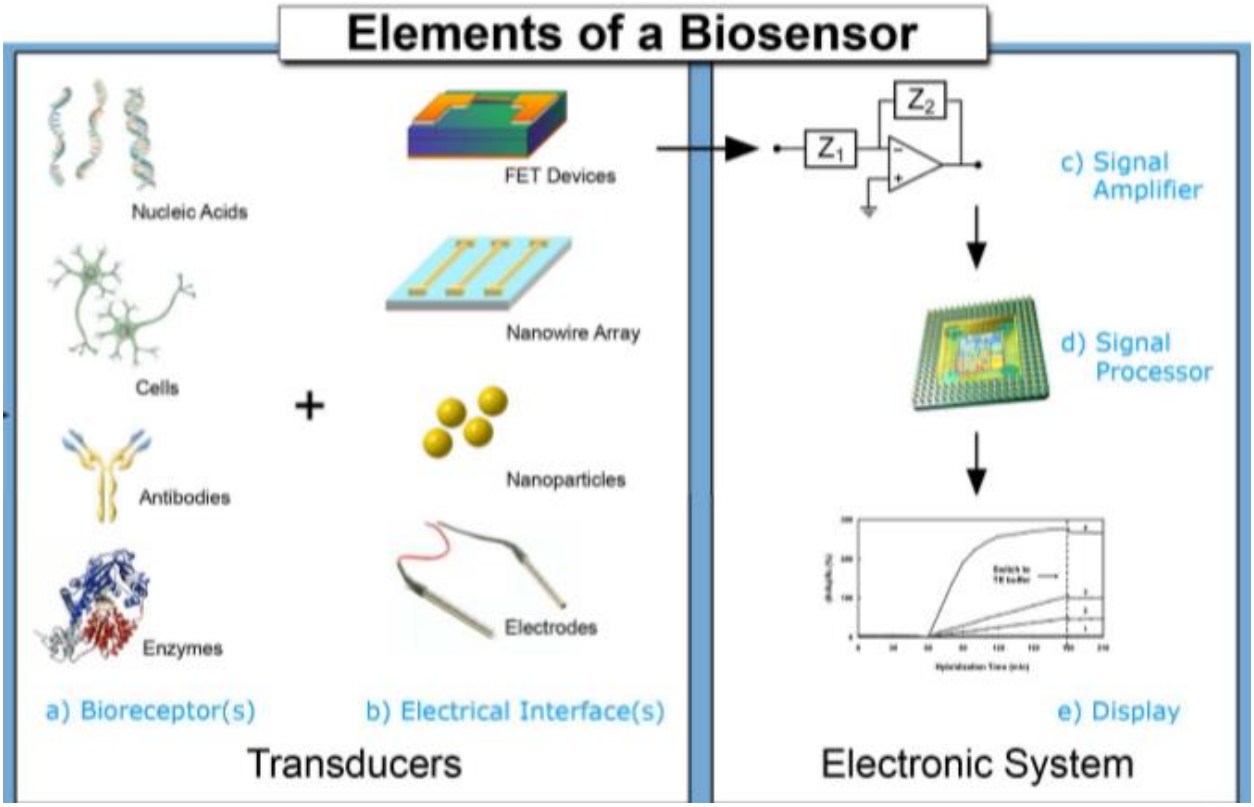

Figure 2.9: Three main elements in a biosensor.[90]

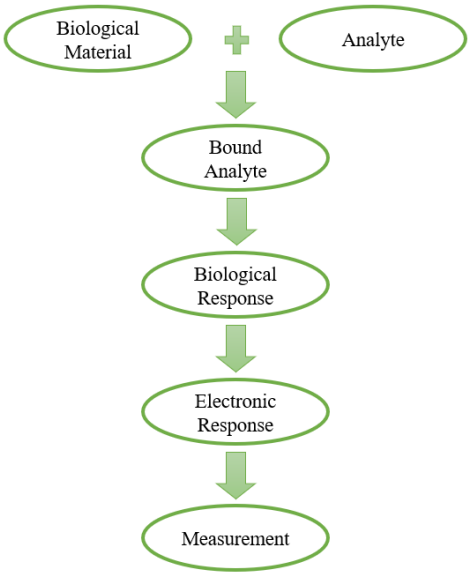

Figure 2.10: General work process in a biosensor.

Figure 2.11 shows a typical electrochemical biosensor. This type of sensor is based on a reaction between probe molecules immobilized on the sensor surface and target molecules. The reaction generates or consumes electrons and generates a signal.[99] A sensor can be based on a two-electrode or three-electrode configuration. An electrochemical biosensor based on a two-electrode system has a working electrode and reference electrode or counter electrode. Biosensor with three-electrode arrangement has a working electrode, a counter electrode and a reference electrode.[100]

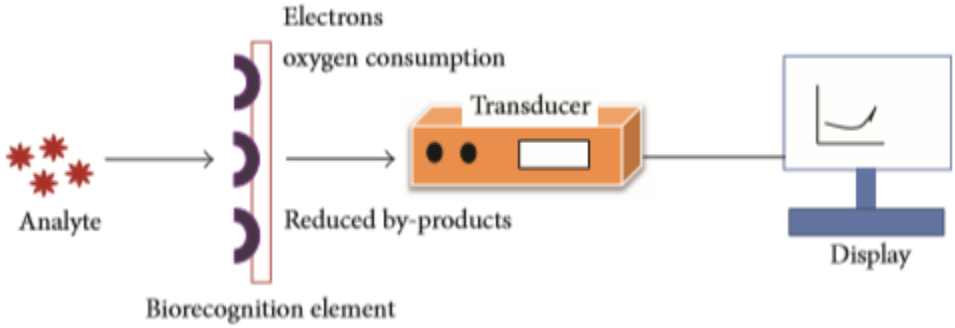

Figure 2.11: A typical electrochemical biosensor.[98]

Electrochemical DNA (E-DNA) sensors are one type of electrochemical biosensor. Like other biosensors, probe molecules are immobilized on the electrode surface. The electrode can be gold,[101] nanoporous alumina,[102] carbon paste electrode,[103], etc. Probe DNA molecules can be stem-loop probe (SLP), linear probe (LP), or pseudoknot DNA.[104] E-DNA sensors can be divided into hybridization-based DNA detection (Figure 2.12 A-D),[105] or enzymatic-based DNA detection (Figure 2.12 E, F).[105] For the first category, target and probe molecules are nucleotides. The signal response strongly depends on the affinity of probe and target molecule to each other. This affinity can be controlled by changing probe design and environmental conditions. In enzyme-based DNA detection, DNA-related enzymes are immobilized on the surface. When target molecules are introduced into the sensor, the number of enzymes increases or decreases due to the reaction

between target molecules and enzymes (such as deletion/fusion of the target DNA). The change in enzyme level causes signal amplification or reduction. This type of sensor is the ideal detection for mismatch DNA, because each enzyme reacts with a DNA with specific sequence .[105]

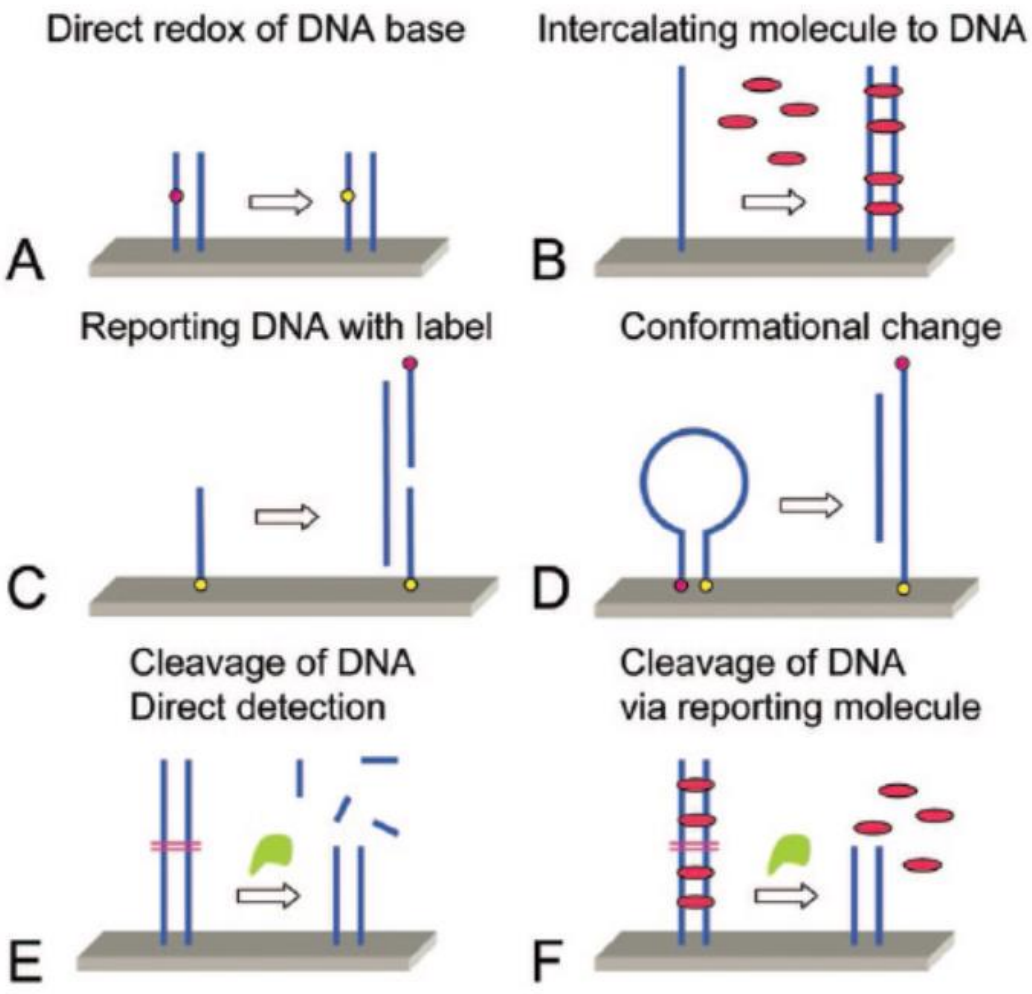

Figure 2.12: Different types of electrochemical DNA sensors. A) Nucleotide bases undergo direct oxidation or reduction. B) single/duplex stands undergo intercalating complex due to adding target molecules. C) Detection of specific DNA with labeled reporting molecules. D) Detection of target species based on conformational change of probe DNA E) Direct detection of target molecules after cleavage of probe DNA through enzymatic process. F) Detection of an extra labeled reporter after specific DNA enzymatic process.[105] Adapted with permission from ref (104), Copyright © 1969, Springer Nature.

There is another way to categorized E-DNA sensors that are based on a detection method that can be indirect detection and direct detection. The indirect detection method is also known as a labeled detection method. It needs to have electroactive mediators, such as ferrocene,[106,107] methylene blue (MB),[108–111] redox-active enzymes,[112] redox intercalators, or nanoparticles.[113] These kinds of E-DNA sensors generate current and electrical impedance signals that are associated with changes in redox kinetic, mass transport, or molecular conformation.[105] This kind of sensor is sensitive and selective; however, the preparation step is time-consuming and costly because it needs the labeling process. Also, this kind of sensor is not suitable for real-time detection.

A direct detection method called a label-free detection method that does not need any redox-active labeling molecules. This method is based on intrinsic electroactivity of DNA, the oxidation of free guanine or adenine bases of DNA probe, that is different before and after hybridization with thymine and cytosine bases of DNA target.[114] After the hybridization step, the number of free guanines and adenine bases decreases, resulting in a decrease in the oxidation/reduction current of the bases.[115]

Although the direct detection method is simple and reagentless, it is sometimes difficult to use because the oxidation of DNA bases is strongly affected by the solution conditions. In addition, these sensors suffer from current signals from other oxidation reactions because of the high oxidation potentials of the guanine bases.[116] In this thesis, a stem-loop DNA molecule tagged with methylene blue was selected as a probe DNA to build a hybridization-based DNA sensor with an indirect detection method.

2.5. Reference

(1) Dudney, N. J. Addition of a Thin-Film Inorganic Solid Electrolyte (Lipon) as a Protective Film in Lithium Batteries with a Liquid Electrolyte. *Journal of Power Sources* **2000**, *89* (2), 176–179. https://doi.org/10.1016/S0378-7753(00)00427-4.

(2) Daza, O. G.; Reádigos, A. A.-C.; Campos, J.; Nair, M. T. S.; Nair, P. K. Formation of Conductive Cdo Thin Films on Photoconductive Cds Thin Films for Window Layer Applications in Solar Cells. *Mod. Phys. Lett. B* **2001**, *15* (17n19), 609–612. https://doi.org/10.1142/S0217984901002117.

(3) Zandi, O.; M. Klahr, B.; W. Hamann, T. Highly Photoactive Ti-Doped α-Fe 2 O 3 Thin Film Electrodes: Resurrection of the Dead Layer. *Energy & Environmental Science* **2013**, *6* (2), 634–642. https://doi.org/10.1039/C2EE23620F.

(4) Wessling, M.; Lidon Lopez, M.; Strathmann, H. Accelerated Plasticization of Thin-Film Composite Membranes Used in Gas Separation. *Separation and Purification Technology* **2001**, *24* (1), 223–233. https://doi.org/10.1016/S1383-5866(01)00127-7.

(5) Xi, J.-Q.; Schubert, M. F.; Kim, J. K.; Schubert, E. F.; Chen, M.; Lin, S.-Y.; Liu, W.; Smart, J. A. Optical Thin-Film Materials with Low Refractive Index for Broadband Elimination of Fresnel Reflection. *Nature Photon* **2007**, *1* (3), 176–179. https://doi.org/10.1038/nphoton.2007.26.

(6) Arias, C. J.; Surmaitis, R. L.; Schlenoff, J. B. Cell Adhesion and Proliferation on the "Living" Surface of a Polyelectrolyte Multilayer. *Langmuir* **2016**, *32* (21), 5412–5421. https://doi.org/10.1021/acs.langmuir.6b00784.

(7) Pinho, A. C.; Piedade, A. P. Zeta Potential, Contact Angles, and AFM Imaging of Protein Conformation Adsorbed on Hybrid Nanocomposite Surfaces. *ACS Appl. Mater. Interfaces* **2013**, *5* (16), 8187–8194. https://doi.org/10.1021/am402302r.

(8) Hung, M.-K.; Wang, Y.-H.; Lin, C.-H.; Lin, H.-C.; Lee, J.-T. Synthesis and Electrochemical Behaviour of Nitroxide Polymer Brush Thin-Film Electrodes for Organic Radical Batteries. *Journal of Materials Chemistry* **2012**, *22* (4), 1570–1577. https://doi.org/10.1039/C1JM13911H.

(9) Krevelen, D. W. van; Nijenhuis, K. te; Te Nijenhuis, K.; W, V. K. *Properties of Polymers: Their Correlation with Chemical Structure; Their Numerical Estimation and Prediction from Additive Group Contributions*; Elsevier Science & Technology: Oxford, NETHERLANDS, THE, 2009.

(10) Olson, D. A.; Chen, L.; Hillmyer, M. A. Templating Nanoporous Polymers with Ordered Block Copolymers. *Chem. Mater.* **2008**, *20* (3), 869–890. https://doi.org/10.1021/cm702239k.

(11) Li, Y.; Ito, T. Size-Exclusion Properties of Nanoporous Films Derived from Polystyrene−Poly(Methylmethacrylate) Diblock Copolymers Assessed Using Direct Electrochemistry of Ferritin. *Anal. Chem.* **2009**, *81* (2), 851–855. https://doi.org/10.1021/ac802201w.

(12) Yang, S. Y.; Ryu, I.; Kim, H. Y.; Kim, J. K.; Jang, S. K.; Russell, T. P. Nanoporous Membranes with Ultrahigh Selectivity and Flux for the Filtration of Viruses. *Advanced Materials* **2006**, *18* (6), 709–712. https://doi.org/10.1002/adma.200501500.

(13) Durkee, D. A.; Eitouni, H. B.; Gomez, E. D.; Ellsworth, M. W.; Bell, A. T.; Balsara, N. P. Catalysts from Self-Assembled Organometallic Block Copolymers. *Advanced Materials* **2005**, *17* (16), 2003–2006. https://doi.org/10.1002/adma.200500352.

(14) Guo, C.; Lin, Y.-H.; Witman, M. D.; Smith, K. A.; Wang, C.; Hexemer, A.; Strzalka, J.; Gomez, E. D.; Verduzco, R. Conjugated Block Copolymer Photovoltaics with near 3% Efficiency through Microphase Separation. *Nano Lett.* **2013**, *13* (6), 2957–2963. https://doi.org/10.1021/nl401420s.

(15) B. Darling, S. Block Copolymers for Photovoltaics. *Energy & Environmental Science* **2009**, *2* (12), 1266–1273. https://doi.org/10.1039/B912086F.

(16) Guenther, M.; Kuckling, D.; Corten, C.; Gerlach, G.; Sorber, J.; Suchaneck, G.; Arndt, K.-F. Chemical Sensors Based on Multiresponsive Block Copolymer Hydrogels. *Sensors and Actuators B: Chemical* **2007**, *126* (1), 97–106. https://doi.org/10.1016/j.snb.2006.10.054.

(17) Nuxoll, E. E.; Hillmyer, M. A.; Wang, R.; Leighton, C.; Siegel, R. A. Composite Block Polymer−Microfabricated Silicon Nanoporous Membrane. *ACS Appl. Mater. Interfaces* **2009**, *1* (4), 888–893. https://doi.org/10.1021/am900013v.

(18) Bang, J.; Jeong, U.; Ryu, D. Y.; Russell, T. P.; Hawker, C. J. Block Copolymer Nanolithography: Translation of Molecular Level Control to Nanoscale Patterns. *Advanced Materials* **2009**, *21* (47), 4769–4792. https://doi.org/10.1002/adma.200803302.

(19) Bates, C. M.; Maher, M. J.; Janes, D. W.; Ellison, C. J.; Willson, C. G. Block Copolymer Lithography. *Macromolecules* **2014**, *47* (1), 2–12. https://doi.org/10.1021/ma401762n.

(20) Schacher, F. H.; Rupar, P. A.; Manners, I. Functional Block Copolymers: Nanostructured Materials with Emerging Applications. *Angewandte Chemie International Edition* **2012**, *51* (32), 7898–7921. https://doi.org/10.1002/anie.201200310.

(21) Hamley, I. W. Structure and Flow Behaviour of Block Copolymers. *J. Phys.: Condens. Matter* **2001**, *13* (33), R643–R671. https://doi.org/10.1088/0953-8984/13/33/201.

(22) Matsen, M. W.; Bates, F. S. Origins of Complex Self-Assembly in Block Copolymers. *Macromolecules* **1996**, *29* (23), 7641–7644. https://doi.org/10.1021/ma960744q.

(23) Fried, J. R. *Polymer Science and Technology*, 2nd ed.; Prentice Hall Professional Technical Reference: Upper Saddle River, NJ, 2003.

(24) Bates, F. S.; Fredrickson, G. H. Block Copolymer Thermodynamics: Theory and Experiment. *Annual Review of Physical Chemistry* **1990**, *41* (1), 525–557. https://doi.org/10.1146/annurev.pc.41.100190.002521.

(25) Helfand, E.; Wasserman, Z. R. Block Copolymer Theory. 4. Narrow Interphase Approximation. *Macromolecules* **1976**, *9* (6), 879–888. https://doi.org/10.1021/ma60054a001.

(26) Meier, D. J. Theory of Block Copolymers. I. Domain Formation in A-B Block Copolymers. *Journal of Polymer Science Part C: Polymer Symposia* **1969**, *26* (1), 81–98. https://doi.org/10.1002/polc.5070260106.

(27) Helfand, E. Block Copolymer Theory. III. Statistical Mechanics of the Microdomain Structure. *Macromolecules* **1975**, *8* (4), 552–556. https://doi.org/10.1021/ma60046a032.

(28) Leibler, L. Theory of Microphase Separation in Block Copolymers. *Macromolecules* **1980**, *13* (6), 1602–1617. https://doi.org/10.1021/ma60078a047.

(29) Matsen, M. W.; Bates, F. S. Unifying Weak- and Strong-Segregation Block Copolymer Theories. *Macromolecules* **1996**, *29* (4), 1091–1098. https://doi.org/10.1021/ma951138i.

(30) Castelletto, V.; Hamley, I. W. Morphologies of Block Copolymer Melts. *Current Opinion in Solid State and Materials Science* **2004**, *8* (6), 426–438. https://doi.org/10.1016/j.cossms.2005.06.001.

(31) Russell, T. P.; Hjelm, R. P.; Seeger, P. A. Temperature Dependence of the Interaction Parameter of Polystyrene and Poly(Methyl Methacrylate). *Macromolecules* **1990**, *23* (3), 890–893. https://doi.org/10.1021/ma00205a033.

(32) Kim, H.-C.; Park, S.-M.; Hinsberg, W. D. Block Copolymer Based Nanostructures: Materials, Processes, and Applications to Electronics. *Chem. Rev.* **2010**, *110* (1), 146–177. https://doi.org/10.1021/cr900159v.

(33) Zhang, X.; F. Douglas, J.; L. Jones, R. Influence of Film Casting Method on Block Copolymer Ordering in Thin Films. *Soft Matter* **2012**, *8* (18), 4980–4987. https://doi.org/10.1039/C2SM07308K.

(34) Schubert, D. W.; Dunkel, T. Spin Coating from a Molecular Point of View: Its Concentration Regimes, Influence of Molar Mass and Distribution. *Mat Res Innovat* **2003**, *7* (5), 314–321. https://doi.org/10.1007/s10019-003-0270-2.

(35) Gu, X.; Gunkel, I.; Russell, T. P. Pattern Transfer Using Block Copolymers. *Philosophical Transactions of the Royal Society A: Mathematical, Physical and Engineering Sciences* **2013**, *371* (2000), 20120306. https://doi.org/10.1098/rsta.2012.0306.

(36) Hashimoto, T.; Bodycomb, J.; Funaki, Y.; Kimishima, K. The Effect of Temperature Gradient on the Microdomain Orientation of Diblock Copolymers Undergoing an Order−Disorder Transition. *Macromolecules* **1999**, *32* (3), 952–954. https://doi.org/10.1021/ma981249s.

(37) Albalak, R. J.; Capel, M. S.; Thomas, E. L. Solvent Swelling of Roll-Cast Triblock Copolymer Films. *Polymer* **1998**, *39* (8), 1647–1656. https://doi.org/10.1016/S0032-3861(97)00497-7.

(38) Kim, S. H.; Misner, M. J.; Xu, T.; Kimura, M.; Russell, T. P. Highly Oriented and Ordered Arrays from Block Copolymers via Solvent Evaporation. *Advanced Materials* **2004**, *16* (3), 226–231. https://doi.org/10.1002/adma.200304906.

(39) Hui, C. -Y.; Wu, K. -C.; Lasky, R. C.; Kramer, E. J. Case-II Diffusion in Polymers. I. Transient Swelling. *Journal of Applied Physics* **1987**, *61* (11), 5129–5136. https://doi.org/10.1063/1.338287.

(40) Sinturel, C.; Vayer, M.; Morris, M.; Hillmyer, M. A. Solvent Vapor Annealing of Block Polymer Thin Films. *Macromolecules* **2013**, *46* (14), 5399–5415. https://doi.org/10.1021/ma400735a.

(41) Campbell, I. P.; He, C.; Stoykovich, M. P. Topologically Distinct Lamellar Block Copolymer Morphologies Formed by Solvent and Thermal Annealing. *ACS Macro Lett.* **2013**, *2* (10), 918–923. https://doi.org/10.1021/mz400269k.

(42) Guo, R.; Huang, H.; Chen, Y.; Gong, Y.; Du, B.; He, T. Effect of the Nature of Annealing Solvent on the Morphology of Diblock Copolymer Blend Thin Films. *Macromolecules* **2008**, *41* (3), 890–900. https://doi.org/10.1021/ma701979q.

(43) Gu, X.; Gunkel, I.; Russell, T. P. Pattern Transfer Using Block Copolymers. *Philosophical Transactions of the Royal Society A: Mathematical, Physical and Engineering Sciences* **2013**, *371* (2000), 20120306. https://doi.org/10.1098/rsta.2012.0306.

(44) Zhao, Y.; Sivaniah, E.; Hashimoto, T. SAXS Analysis of the Order−Disorder Transition and the Interaction Parameter of Polystyrene-Block-Poly(Methyl Methacrylate). *Macromolecules* **2008**, *41* (24), 9948–9951. https://doi.org/10.1021/ma8013004.

(45) Gu, X.; Gunkel, I.; Russell, T. P. Pattern Transfer Using Block Copolymers. *Philosophical Transactions of the Royal Society A: Mathematical, Physical and Engineering Sciences* **2013**, *371* (2000), 20120306. https://doi.org/10.1098/rsta.2012.0306.

(46) Mansky, P.; Russell, T. P.; Hawker, C. J.; Mays, J.; Cook, D. C.; Satija, S. K. Interfacial Segregation in Disordered Block Copolymers: Effect of Tunable Surface Potentials. *Physical Review Letters* **1997**, *79*, 237–240. https://doi.org/10.1103/PhysRevLett.79.237.

(47) Farrell, R. A.; Petkov, N.; Shaw, M. T.; Djara, V.; Holmes, J. D.; Morris, M. A. Monitoring PMMA Elimination by Reactive Ion Etching from a Lamellar PS-b-PMMA Thin Film by Ex Situ TEM Methods. *Macromolecules* **2010**, *43* (20), 8651–8655. https://doi.org/10.1021/ma101827u.

(48) Ranby, B.; Rabek, J. . *Photodegradation, Photo-oxidation and Photostabilization of Polymers*; Wiley-Interscience: New York, 1975.

(49) Thurn-Albrecht, T.; Steiner, R.; DeRouchey, J.; Stafford, C. M.; Huang, E.; Bal, M.; Tuominen, M.; Hawker, C. J.; Russell, T. P. Nanoscopic Templates from Oriented Block Copolymer Films. *Advanced Materials* **2000**, *12* (11), 787–791. https://doi.org/10.1002/(SICI)1521-4095(200006)12:11<787::AID-ADMA787>3.0.CO;2-1.

(50) Ahn, H.; Ryu, D. Y.; Kim, Y.; Kwon, K. W.; Lee, J.; Cho, J. Phase Behavior of Polystyrene-b-Poly(Methyl Methacrylate) Diblock Copolymer. *Macromolecules* **2009**, *42* (20), 7897–7902. https://doi.org/10.1021/ma901313a.

(51) Kim, S. H.; Misner, M. J.; Xu, T.; Kimura, M.; Russell, T. P. Highly Oriented and Ordered Arrays from Block Copolymers via Solvent Evaporation. *Advanced Materials* **2004**, *16* (3), 226–231. https://doi.org/10.1002/adma.200304906.

(52) Kim, S. H.; Misner, M. J.; Russell, T. P. Solvent-Induced Ordering in Thin Film Diblock Copolymer/Homopolymer Mixtures. *Advanced Materials* **2004**, *16* (23–24), 2119–2123. https://doi.org/10.1002/adma.200306577.

(53) Peng, J.; Han, Y.; Knoll, W.; Kim, D. H. Development of Nanodomain and Fractal Morphologies in Solvent Annealed Block Copolymer Thin Films. *Macromolecular Rapid Communications* **2007**, *28* (13), 1422–1428. https://doi.org/10.1002/marc.200700206.

(54) Mao, H.; Hillmyer, M. A. Nanoporous Polystyrene by Chemical Etching of Poly(Ethylene Oxide) from Ordered Block Copolymers. *Macromolecules* **2005**, *38* (9), 4038–4039. https://doi.org/10.1021/ma050008z.

(55) Bang, J.; Kim, S. H.; Drockenmuller, E.; Misner, M. J.; Russell, T. P.; Hawker, C. J. Defect-Free Nanoporous Thin Films from ABC Triblock Copolymers. *J. Am. Chem. Soc.* **2006**, *128* (23), 7622–7629. https://doi.org/10.1021/ja0608141.

(56) Zhao, H.; Gu, W.; Sterner, E.; Russell, T. P.; Coughlin, E. B.; Theato, P. Highly Ordered Nanoporous Thin Films from Photocleavable Block Copolymers. *Macromolecules* **2011**, *44* (16), 6433–6440. https://doi.org/10.1021/ma201416b.

(57) Curtis, H. D. METHODS OF SILVERING MIRRORS. *PASP* **1911**, *23* (135), 13. https://doi.org/10.1086/122040.

(58) Malureanu, R.; Zalkovskij, M.; Andryieuski, A.; Lavrinenko, A. V. Controlled Ag Electroless Deposition in Bulk Structures with Complex Three-Dimensional Profiles. *J. Electrochem. Soc.* **2010**, *157* (12), K284–K288. https://doi.org/10.1149/1.3502640.

(59) Boehm, J.; François, A.; Ebendorff-Heidepriem, H.; Monro, T. M. Chemical Deposition of Silver for the Fabrication of Surface Plasmon Microstructured Optical Fibre Sensors. *Plasmonics* **2011**, *6* (1), 133–136. https://doi.org/10.1007/s11468-010-9178-z.

(60) Roy, A.; Singha, S. S.; Majumder, S.; Singha, A.; Banerjee, S.; Satpati, B. Electroless Deposition of Pd Nanostructures for Multifunctional Applications as Surface-Enhanced Raman Scattering Substrates and Electrochemical Nonenzymatic Sensors. *ACS Appl. Nano Mater.* **2019**, *2* (4), 2503–2514. https://doi.org/10.1021/acsanm.9b00420.

(61) Shi, S.; Wang, L.; Wang, A.; Huang, R.; Ding, L.; Su, R.; Qi, W.; He, Z. Bioinspired Fabrication of Optical Fiber SPR Sensors for Immunoassays Using Polydopamine-Accelerated Electroless Plating. *J. Mater. Chem. C* **2016**, *4* (32), 7554–7562. https://doi.org/10.1039/C6TC02149B.

(62) Mallory, G. O.; Hajdu, J. B. *Electroless Plating: Fundamentals and Applications*; Noyes Publications/William Andrew Pub., 1990.

(63) Tongxiang, L.; Wenli, G.; Yinghui, Y.; Chunhe, T. Electroless Plating of Silver on Graphite Powders and the Study of Its Conductive Adhesive. *International Journal of Adhesion and Adhesives* **2008**, *28* (1), 55–58. https://doi.org/10.1016/j.ijadhadh.2007.03.006.

(64) Montazer, M.; Allahyarzadeh, V. Electroless Plating of Silver Nanoparticles/Nanolayer on Polyester Fabric Using AgNO3/NaOH and Ammonia. *Ind. Eng. Chem. Res.* **2013**, *52* (25), 8436–8444. https://doi.org/10.1021/ie400804n.

(65) Paunovic, M.; Schlesinger, M. *Fundamentals of Electrochemical Deposition*; John Wiley & Sons, Ltd, 2005; Vol. 8.

(66) Nagaya, S.; Nishikiori, H. Preparation of Dye-Adsorbing ZnO Thin Films by Electroless Deposition and Their Photoelectrochemical Properties. *ACS Appl. Mater. Interfaces* **2013**, *5* (18), 8841–8844. https://doi.org/10.1021/am4026483.

(67) De Leo, M.; Pereira, F. C.; Moretto, L. M.; Scopece, P.; Polizzi, S.; Ugo, P. Towards a Better Understanding of Gold Electroless Deposition in Track-Etched Templates. *Chem. Mater.* **2007**, *19* (24), 5955–5964. https://doi.org/10.1021/cm071703j.

(68) Popescu, S. M.; Barlow, A. J.; Ramadan, S.; Ganti, S.; Ghosh, B.; Hedley, J. Electroless Nickel Deposition: An Alternative for Graphene Contacting. *ACS Appl. Mater. Interfaces* **2016**, *8* (45), 31359–31367. https://doi.org/10.1021/acsami.6b08290.

(69) Lee, C.-C.; Chou, T.-C. Effects of Magnetic Field on the Electroless Nickel/Cobalt Deposition. *Ind. Eng. Chem. Res.* **1998**, *37* (5), 1815–1820. https://doi.org/10.1021/ie970706a.

(70) Lahiri, A.; Lu, T.; Behrens, N.; Borisenko, N.; Li, G.; Endres, F. Hydrofluoric Acid-Free Electroless Deposition of Metals on Silicon in Ionic Liquids and Its Enhanced Performance in Lithium Storage. *ACS Appl. Mater. Interfaces* **2017**, *9* (13), 11350–11355. https://doi.org/10.1021/acsami.7b01404.

(71) Cauchy, X.; Klemberg-Sapieha, J.-E.; Therriault, D. Synthesis of Highly Conductive, Uniformly Silver-Coated Carbon Nanofibers by Electroless Deposition. *ACS Appl. Mater. Interfaces* **2017**, *9* (34), 29010–29020. https://doi.org/10.1021/acsami.7b06526.

(72) Brevnov, D. A.; Olson, T. S.; López, G. P.; Atanassov, P. Electroless Deposition of Silver by Galvanic Displacement on Aluminum Alloyed with Copper. *J. Phys. Chem. B* **2004**, *108* (45), 17531–17536. https://doi.org/10.1021/jp047096u.

(73) Azzaroni, O.; Zheng, Z.; Yang, Z.; Huck, W. T. S. Polyelectrolyte Brushes as Efficient Ultrathin Platforms for Site-Selective Copper Electroless Deposition. *Langmuir* **2006**, *22* (16), 6730–6733. https://doi.org/10.1021/la060891+.

(74) Zangmeister, C. D.; van Zee, R. D. Electroless Deposition of Copper onto 4-Mercaptobenzoic Acid Self-Assembled on Gold. *Langmuir* **2003**, *19* (19), 8065–8068. https://doi.org/10.1021/la026801s.

(75) Dinderman, M. A.; Dressick, W. J.; Kostelansky, C. N.; Price, R. R.; Qadri, S. B.; Schoen, P. E. Electroless Plating of Iron onto Cellulose Fibers. *Chem. Mater.* **2006**, *18* (18), 4361–4368. https://doi.org/10.1021/cm060649o.

(76) Djokić, S. S. Electroless Deposition of Cobalt Using Hydrazine as a Reducing Agent. *J. Electrochem. Soc.* **1997**, *144* (7), 2358–2363. https://doi.org/10.1149/1.1837818.

(77) Kobayashi, Y.; Salgueiriño-Maceira, V.; Liz-Marzán, L. M. Deposition of Silver Nanoparticles on Silica Spheres by Pretreatment Steps in Electroless Plating. *Chem. Mater.* **2001**, *13* (5), 1630–1633. https://doi.org/10.1021/cm001240g.

(78) Suzuki, Y.; Ogasawara, H. Reduction Position Controlled Electroless Silver Deposition on Glass Substrate via a Silver Seed Layer Itself. *aap* **2016**, *4*, 51–58. https://doi.org/10.12988/aap.2016.6911.

(79) Shacham-Diamand, Y.; Inberg, A.; Sverdlov, Y.; Croitoru, N. Electroless Silver and Silver with Tungsten Thin Films for Microelectronics and Microelectromechanical System Applications. *J. Electrochem. Soc.* **2000**, *147* (9), 3345–3349. https://doi.org/10.1149/1.1393904.

(80) Lu, Y.; Jiang, S.; Huang, Y. Ultrasonic-Assisted Electroless Deposition of Ag on PET Fabric with Low Silver Content for EMI Shielding. *Surface and Coatings Technology* **2010**, *204* (16), 2829–2833. https://doi.org/10.1016/j.surfcoat.2010.02.061.

(81) Arai, S.; Fujii, J. Electroless Deposition of Silver on Multiwalled Carbon Nanotubes Using Iodide Bath. *J. Electrochem. Soc.* **2011**, *158* (8), D506–D510. https://doi.org/10.1149/1.3599066.

(82) Srikanth, C. K.; Jeevanandam, P. Electroless Deposition of Silver on Synthesized Calcite via Surface Modification. *Applied Surface Science* **2009**, *255* (16), 7153–7157. https://doi.org/10.1016/j.apsusc.2009.03.049.

(83) Watson, J. D.; Crick, F. H. C. Molecular Structure of Nucleic Acids: A Structure for Deoxyribose Nucleic Acid. *Nature* **1953**, *171* (4356), 737–738. https://doi.org/10.1038/171737a0.

(84) Alberts, B.; Johnson, A.; Lewis, J.; Raff, M.; Roberts, K.; Walter, P. *Molecular Biology of the Cell*, 4th ed.; New York: Garland Science, 2002; Vol. The Structure and Function of DNA.

(85) Sohrabi, N.; Valizadeh, A.; Farkhani, S. M.; Akbarzadeh, A. Basics of DNA Biosensors and Cancer Diagnosis. *Artificial Cells, Nanomedicine, and Biotechnology* **2016**, *44* (2), 654–663. https://doi.org/10.3109/21691401.2014.976707.

(86) Wang, J. Electrochemical Glucose Biosensors. *Chem. Rev.* **2008**, *108* (2), 814–825. https://doi.org/10.1021/cr068123a.

(87) Avramescu, A.; Andreescu, S.; Noguer, T.; Bala, C.; Andreescu, D.; Marty, J.-L. Biosensors Designed for Environmental and Food Quality Control Based on Screen-Printed Graphite Electrodes with Different Configurations. *Anal Bioanal Chem* **2002**, *374* (1), 25–32. https://doi.org/10.1007/s00216-002-1312-0.

(88) Yáñez-Sedeño, P.; Agüí, L.; Villalonga, R.; Pingarrón, J. M. Biosensors in Forensic Analysis. A Review. *Anal. Chim. Acta* **2014**, *823*, 1–19. https://doi.org/10.1016/j.aca.2014.03.011.

(89) Andres, R. T.; Narayanaswamy, R. Fibre-Optic Pesticide Biosensor Based on Covalently Immobilized Acetylcholinesterase and Thymol Blue. *Talanta* **1997**, *44* (8), 1335–1352. https://doi.org/10.1016/S0039-9140(96)02071-1.

(90) Clark, L. C.; Lyons, C. Electrode Systems for Continuous Monitoring in Cardiovascular Surgery. *Ann. N. Y. Acad. Sci.* **1962**, *102*, 29–45. https://doi.org/10.1111/j.1749-6632.1962.tb13623.x.

(91) Grieshaber, D.; MacKenzie, R.; Vörös, J.; Reimhult, E. Electrochemical Biosensors - Sensor Principles and Architectures. *Sensors (Basel)* **2008**, *8* (3), 1400–1458.

(92) Damborský, P.; Švitel, J.; Katrlík, J. Optical Biosensors. *Essays Biochem* **2016**, *60* (1), 91–100. https://doi.org/10.1042/EBC20150010.

(93) Ye, J.; Letcher, S. V.; Rand, A. G. Piezoelectric Biosensor for Detection of Salmonella Typhimurium. *Journal of Food Science* **1997**, *62* (5), 1067–1086. https://doi.org/10.1111/j.1365-2621.1997.tb15039.x.

(94) Pohanka, M. Overview of Piezoelectric Biosensors, Immunosensors and DNA Sensors and Their Applications. *Materials (Basel)* **2018**, *11* (3). https://doi.org/10.3390/ma11030448.

(95) Zheng, Y.-H.; Hua, T.-C.; Xu, F. A Novel Thermal Biosensor Based on Enzyme Reaction for Pesticides Measurement. *J Environ Sci (China)* **2005**, *17* (4), 615–619.

(96) Ali, J.; Najeeb, J.; Asim Ali, M.; Farhan Aslam, M.; Raza, A. Biosensors: Their Fundamentals, Designs, Types and Most Recent Impactful Applications: A Review. *J Biosens Bioelectron* **2017**, *08* (01). https://doi.org/10.4172/2155-6210.1000235.

(97) Liébana, S.; Drago, G. A. Bioconjugation and Stabilisation of Biomolecules in Biosensors. *Essays Biochem* **2016**, *60* (1), 59–68. https://doi.org/10.1042/EBC20150007.

(98) Malhotra, S.; Verma, A.; Tyagi, N.; Kumar, V. BIOSENSORS: PRINCIPLE, TYPES AND APPLICATIONS. *International Journal of Advance Research and Innovative Ideas in Education* **2017**, *3* (2), 3639–3644.

(99) Dhull, V.; Gahlaut, A.; Dilbaghi, N.; Hooda, V. Acetylcholinesterase Biosensors for Electrochemical Detection of Organophosphorus Compounds: A Review. *Biochem Res Int* **2013**, *2013*, 731501. https://doi.org/10.1155/2013/731501.

(100) Liu, C. C. Electrochemical Based Biosensors. *Biosensors* **2012**, *2* (3), 269–272. https://doi.org/10.3390/bios2030269.

(101) Idili, A.; Amodio, A.; Vidonis, M.; Feinberg-Somerson, J.; Castronovo, M.; Ricci, F. Folding-upon-Binding and Signal-on Electrochemical DNA Sensor with High Affinity and Specificity. *Anal. Chem.* **2014**, *86* (18), 9013–9019. https://doi.org/10.1021/ac501418g.

(102) Rai, V.; Deng, J.; Toh, C.-S. Electrochemical Nanoporous Alumina Membrane-Based Label-Free DNA Biosensor for the Detection of Legionella Sp. *Talanta* **2012**, *98*, 112–117. https://doi.org/10.1016/j.talanta.2012.06.055.

(103) Erdem, A.; Kerman, K.; Meric, B.; Akarca, U. S.; Ozsoz, M. DNA Electrochemical Biosensor for the Detection of Short DNA Sequences Related to the Hepatitis B Virus. *Electroanalysis* **1999**, *11* (8), 586–587. https://doi.org/10.1002/(SICI)1521-4109(199906)11:8<586::AID-ELAN586>3.0.CO;2-J.

(104) Cash, K. J.; Heeger, A. J.; Plaxco, K. W.; Xiao, Y. Optimization of a Reusable, DNA Pseudoknot-Based Electrochemical Sensor for Sequence-Specific DNA Detection in Blood Serum. *Anal. Chem.* **2009**, *81* (2), 656–661. https://doi.org/10.1021/ac802011d.

(105) Wei, F.; Lillehoj, P. B.; Ho, C.-M. DNA Diagnostics: Nanotechnology-Enhanced Electrochemical Detection of Nucleic Acids. *Pediatr. Res.* **2010**, *67* (5), 458–468. https://doi.org/10.1203/PDR.0b013e3181d361c3.

(106) Zuo, X.; Song, S.; Zhang, J.; Pan, D.; Wang, L.; Fan, C. A Target-Responsive Electrochemical Aptamer Switch (TREAS) for Reagentless Detection of Nanomolar ATP. *J. Am. Chem. Soc.* **2007**, *129* (5), 1042–1043. https://doi.org/10.1021/ja067024b.

(107) Ferapontova, E. E.; Gothelf, K. V. Effect of Serum on an RNA Aptamer-Based Electrochemical Sensor for Theophylline. *Langmuir* **2009**, *25* (8), 4279–4283. https://doi.org/10.1021/la804309j.

(108) Kang, D.; Ricci, F.; White, R. J.; Plaxco, K. W. Survey of Redox-Active Moieties for Application in Multiplexed Electrochemical Biosensors. *Anal. Chem.* **2016**, *88* (21), 10452–10458. https://doi.org/10.1021/acs.analchem.6b02376.

(109) Ricci, F.; Lai, R. Y.; Heeger, A. J.; Plaxco, K. W.; Sumner, J. J. Effect of Molecular Crowding on the Response of an Electrochemical DNA Sensor. *Langmuir* **2007**, *23* (12), 6827–6834. https://doi.org/10.1021/la700328r.

(110) Kang, D.; Zuo, X.; Yang, R.; Xia, F.; Plaxco, K. W.; White, R. J. Comparing the Properties of Electrochemical-Based DNA Sensors Employing Different Redox Tags. *Anal. Chem.* **2009**, *81* (21), 9109–9113. https://doi.org/10.1021/ac901811n.

(111) Ferapontova, E. E.; Gothelf, K. V. Optimization of the Electrochemical RNA-Aptamer Based Biosensor for Theophylline by Using a Methylene Blue Redox Label. *Electroanalysis* **2009**, *21* (11), 1261–1266. https://doi.org/10.1002/elan.200804558.

(112) Patolsky, F.; Lichtenstein, A.; Willner, I. Detection of Single-Base DNA Mutations by Enzyme-Amplified Electronic Transduction. *Nat Biotechnol* **2001**, *19* (3), 253–257. https://doi.org/10.1038/85704.

(113) Castañeda, M. T.; Merkoçi, A.; Pumera, M.; Alegret, S. Electrochemical Genosensors for Biomedical Applications Based on Gold Nanoparticles. *Biosensors and Bioelectronics* **2007**, *22* (9), 1961–1967. https://doi.org/10.1016/j.bios.2006.08.031.

(114) Karadeniz, H.; Gulmez, B.; Sahinci, F.; Erdem, A.; Kaya, G. I.; Unver, N.; Kivcak, B.; Ozsoz, M. Disposable Electrochemical Biosensor for the Detection of the Interaction between DNA and Lycorine Based on Guanine and Adenine Signals. *Journal of Pharmaceutical and Biomedical Analysis* **2003**, *33* (2), 295–302. https://doi.org/10.1016/S0731-7085(03)00283-8.

(115) Souza, E.; Nascimento, G.; Santana, N.; Ferreira, D.; Lima, M.; Natividade, E.; Martins, D.; Lima-Filho, J. Label-Free Electrochemical Detection of the Specific Oligonucleotide Sequence of Dengue Virus Type 1 on Pencil Graphite Electrodes. *Sensors* **2011**, *11* (6), 5616–5629. https://doi.org/10.3390/s110605616.

(116) Galán, T.; Prieto-Simón, B.; Alvira, M.; Eritja, R.; Götz, G.; Bäuerle, P.; Samitier, J. Label-Free Electrochemical DNA Sensor Using “Click”-Functionalized PEDOT Electrodes. *Biosensors and Bioelectronics* **2015**, *74*, 751–756. https://doi.org/10.1016/j.bios.2015.07.037.

Chapter 3 - Analytical Techniques Used in this Research

This chapter includes all analytical techniques that were used for the characterization of PS-*b*-PMMA- and PS-*hv*-PEO-derived films. The thickness of a polymer film was measured by spectroscopic ellipsometry. The surface morphology of a polymer film was evaluated by atomic force microscopy (AFM). X-ray photoelectron spectroscopy (XPS) was used to analyze the elemental composition of a polymer film before and after silver electroless deposition. Cyclic voltammetry (CV) was used to assess electrochemical biosensor performance. Fluorescence spectroscopy was used to investigate the surface chemistry of nanoporous films.

3.1. Spectroscopic Ellipsometry

Spectroscopic Ellipsometry is a versatile, sensitive, fast, and convenient optical technique to acquire information about the thickness, roughness, and optical constants of a thin film.[1,2] This method is non-destructive and contactless because it involves only the irradiation of a weak incident beam with different wavelength ranges. The method is based on a change in beam polarization state when an incident beam reflects or transmits from thin film material.[3] Incident light with a linearly polarized state hits a sample with Θ_o. Then, light reflects from the sample, giving light with a different polarization state to give elliptically polarized light (Figure 3.1).[4]

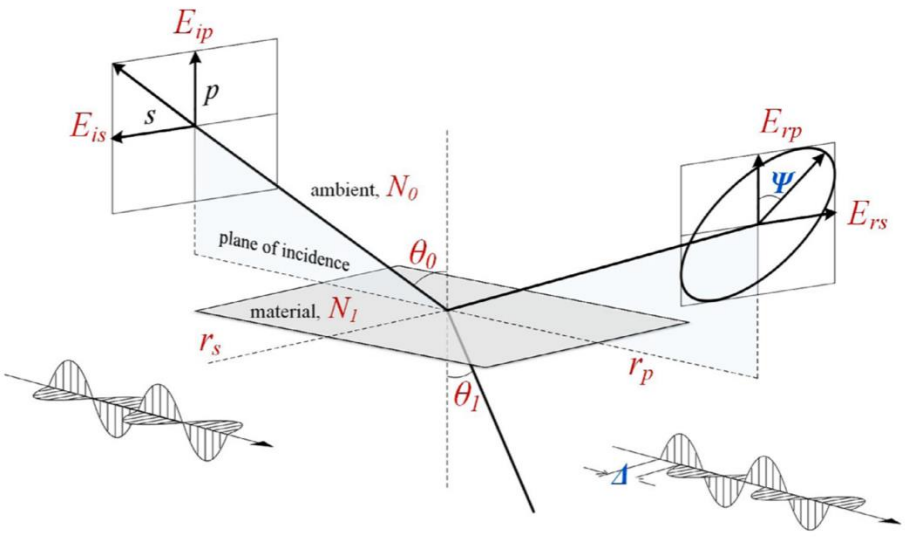

Figure 3.1: Optical reflection and transmission for incident polarization from thin-film layer. Adapted with permission from ref (4), © 2015 Elsevier Ltd.

The quantity of beam polarization change can be defined by phase difference (Δ, delta) and amplitude change upon reflection (Ψ, psi). The change depends on film thickness and refractive index. The principal equation for an ellipsometry measurement described as Equation 3.1[4]

$$\rho = r_p/r_s = \tan\Psi \exp(i\Delta) \qquad \text{(eq.3.1)}$$

As shown in Equation 3.1, the ratio of the amplitude reflection coefficients r_s (polarized parallel light) and r_p (perpendicular to the plane of incidence) are the results of an ellipsometry measurement.

Spectroscopic Ellipsometry is an indirect technique to measure film thickness. It means, first Δ and Ψ are collected for light with different wavelengths. Then Δ and Ψ are plotted as a function of wavelength. At the end, they are matched to Δ and Ψ values generated with an appropriate optical model. Some parameters should be considered to define an optical model for a sample. The parameters include a number of different reflective layers, extinction coefficient (k), and refractive index n of distinct layers.[5] For transparent thin film materials that do not have

absorbing dielectric property, *k* can be considered as zero, and Cauchy dispersion formula can be used (Equation 3.2).[5] Cauchy dispersion formula is a formula that shows the approximate relation between light wavelength (λ) and reflective index (n) of each medium.[6]

$$n(\lambda) = A + B/\lambda^2 + C/\lambda^4 \qquad \text{eq.3.2}$$

The basic configuration of an ellipsometer is shown in Figure 3.2,[7] including a beam source, polarizer, compensator, sample, analyzer, and detector. The beam is emitted by the beam source and passes through the polarizer to make linearly-polarized light, then goes into the compensator and then hits the sample with $\varphi > 0$ angles. The beam reflects off from the sample, and after passing through the analyzer, it goes to a detector. The source, polarizer, and compensator prepare a known polarization state of light incident on the sample. The sample changes the polarization and then the analyzer and detector detect this change.[8]

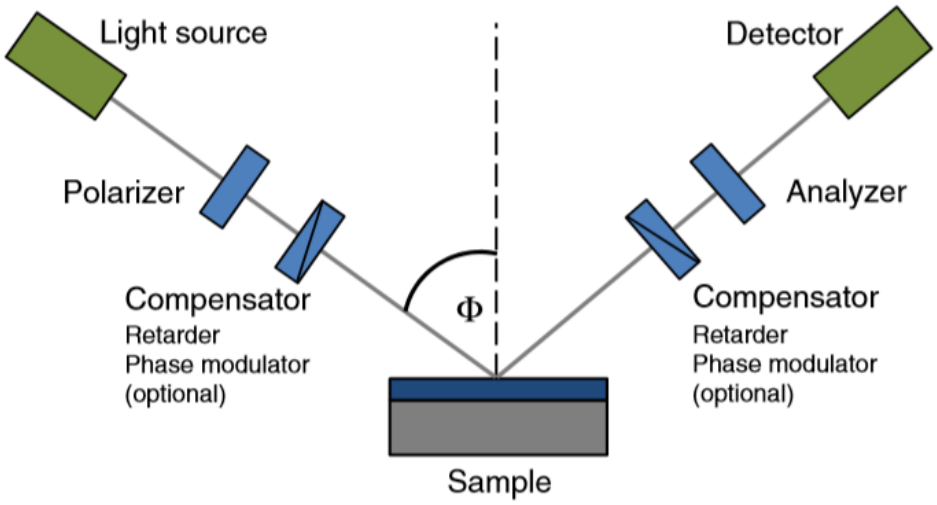

Figure 3.2: Configuration of an ellipsometer.[7]

3.2. Atomic Force Microscopy (AFM)

Atomic force microscopy was invented in 1985.[9] AFM can be used to gain information with nanometer resolution about surface morphology,[10] surface roughness,[11] stiffness,[12] adhesiveness,[13] viscosity,[14] hydrophobicity,[11] and conductivity.[15] A typical AFM system has three main parts shown in Figure 3.3[16], including a cantilever with an ultra-sharp tip, laser light, and photodetector.

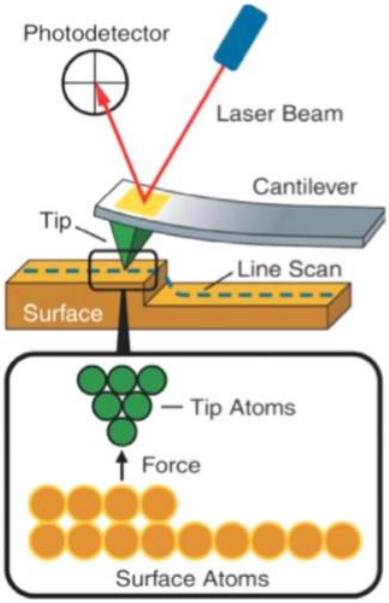

Figure 3.3: Schematic of the basic principle of AFM. Adapted with permission from ref (16), Copyright © 2008 Elsevier Ltd.

The AFM is based on the detection of forces acting between an AFM tip and the surface of the sample. The force cannot be measured directly. It can be measured from the deflection of the stiff cantilever, according to Hooke's law (Equation 3.3).

$$F = mx \qquad \text{(eq.3.3)}$$

where F is the force between the tip and surface, m is the spring constant of the cantilever, and x is the deflection of the cantilever.[17] The cantilever connected to the AFM tip moves backward and

forward across the sample surface due to the difference in the surface height. The laser beam is reflected at the top of the cantilever and collected by the photodetector that detects the cantilever deflection. The horizontal position of the tip is controlled by a piezo scanner. Therefore, the topographic information on the sample surface can be obtained.[18] AFM is normally used with three modes: contact mode (known as a repulsive mode), tapping mode, and non-contact mode (Figure 3.4). The tip drags on the sample to scan the surface in the contact mode. In this mode, van der Waals repulsion is the main interaction between the sample surface and the tip.

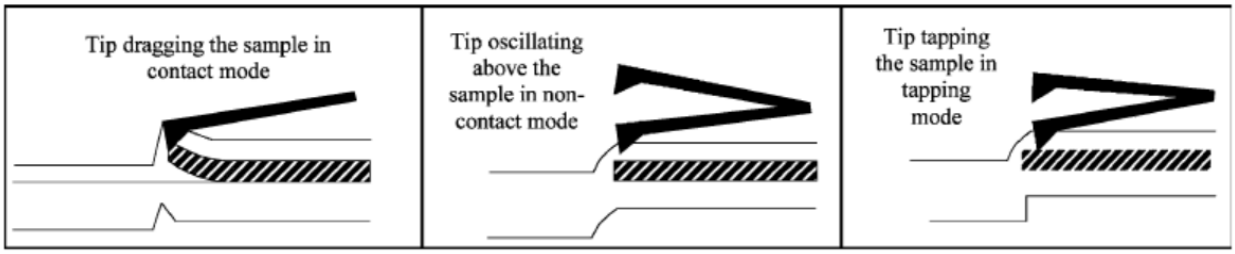

Figure 3.4: Three normal AFM modes, the left one is the contact mode, the middle one is the non-contact mode and the right one is the tapping mode.[19] Adapted with permission from ref (19), Copyright © 2004 Elsevier Ltd.

In the tapping mode, the cantilever oscillates up and down at or slightly below its resonance frequency so that the tip taps the surface of the sample.[20] When the tip touches the sample surface, the amplitude of oscillation decreases due to interactions (van der Waals forces, dipole-dipole interactions, electrostatic forces, etc.) between the tip and the sample surface. An image is obtained through measurements of the oscillation amplitude change. This mode is convenient to obtain the high-resolution image of a soft sample. In addition, when the tip faces a sample surface of different chemical compositions, a phase angle between the external driving force and the cantilever oscillation response shifts due to changes in interaction forces between the tip and sample.[15,21] The difference in the phase angle shift gives a phase image which helps to obtain information about

surface chemical compositions and viscoelasticity that are beyond surface topography.[22] Phase and height images can be recorded at the same time.

In the non-contact mode, a tip on a cantilever oscillated at a small amplitude moves above the sample surface at distance 50-150 Å. The tip detects a tip-surface force due to van der Waals attraction as changes in the frequency, amplitude, or phase of the cantilever oscillation.[19] In this thesis, tapping mode AFM was used to get the height and phase images of sample surfaces. Height images gave information about the topography of the polymer surface, while phase images gave information about surface chemical compositions.

3.3. Fluorescence Spectroscopy

Fluorescence spectroscopy (fluorometry) is a fast, simple, and sensitive type of electromagnetic spectroscopy that takes advantage of the process of fluorescence to learn about a fluorophore. Fluorescence spectroscopy measures the intensity and wavelength distribution of the emission spectrum of a fluorophore after photoexcitation in a particular wavelength range.[23] The most fluorophore molecules inhabit the lowest electronic ground state (a low energy state). When molecules are exposed to the light, they absorb photons and elevate to one of the higher vibrational sub-levels associated with an electronic excited state. Then excited molecules lose the extra gained vibration energy by collision and drop in the lowest vibrational level of the excited state. At this point, molecules emit their energy in the form of fluorescence and return to one of the vibrational levels of the electronic ground state. Therefore, a typical fluorescence lifetime is near 10 ns. Fluorescence process is depicted diagrammatically with the Jablonski energy diagram shown in Figure 3.5.[24]

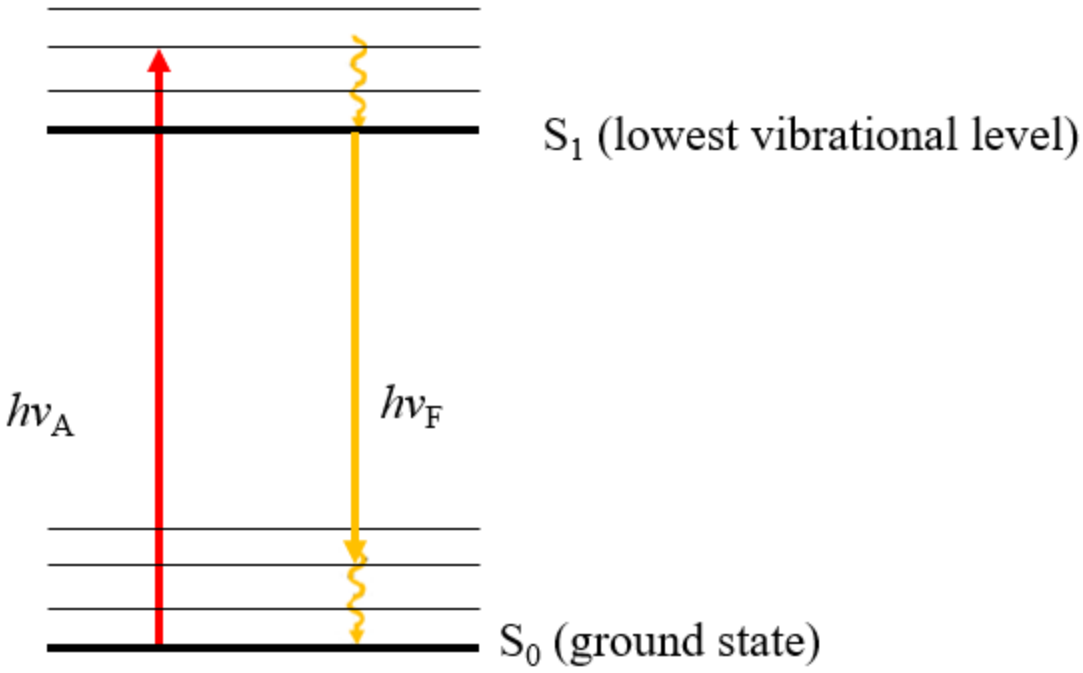

Figure 3.5: Jablonski energy diagram.

The design of a simple fluorometer is shown in Figure 3.6.[25] The light from a source passes through the excitation wavelength selector and then passes through the sample. The fluorophore molecules in a sample absorb some parts of the incident light then emit fluorescence in all directions. Some of this fluorescent light is captured by the emission wavelength selector and reaches a detector at 90° to the direction of the beam from the source. The detector is placed at 90° of the incident beam to minimize transmitted or reflected incident light reaching the detector.

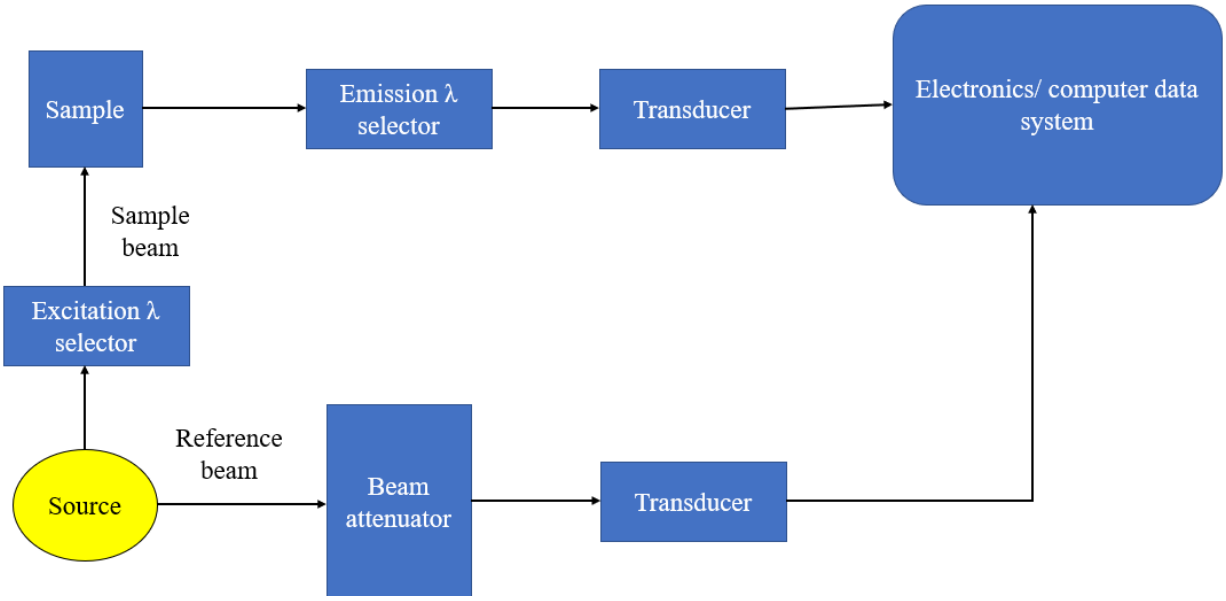

Figure 3.6: Component of a fluorometer.

Fluorimetry can be used for quantitative applications. Fluorescence power is directly proportional to fluorophore concentration and can be calculated using Equation.3.4 .[25]

$$F = KC = 2.303K'\varepsilon bCP_o = 2.303\phi_f K''\varepsilon bCP_o \qquad \text{(eq.3.4)}$$

In this equation, F and C are fluorescence intensity and concentration of fluorophore, respectively. K'', K', and K are constants. ϕ_f is the quantum efficiency of fluorescence for a given system. ε, b, and P_o are the molar absorption coefficient, the path length, and the power of the incident beam, respectively. A plot of fluorescence intensity as a function of fluorophore concentration is linear at relatively low fluorophore concentration, and the plot can be used to determine the fluorophore concentration of an unknown solution.[25] The linear relationship between concentration and fluorescence intensity is no longer valid at high fluorophore concentrations due to the inner filter effect, in which some of the emitted light is reabsorbed by other fluorophore molecules to decrease fluorescence intensity. The fluorescence spectra may change if environments around fluorophore molecules such as viscosity, pH, temperature, pressure and polarity change. The resulting changes

in fluorescence spectra include an increase or a decrease in fluorescence emission intensity, and a shift of emission wavelength.[26]

Solvatochromism phenomenon happens when a solute is dissolved in solvents with different polarities and leads to a change in position, intensity and shape of a fluorescence band. When solvent polarity increases, a red shift or blue shift can occur, which called positive and negative solvatochromism, respectively.[27] Positive solvatochromism happens when the permanent dipole moment of the excited state is larger than that of the ground state. The change in fluorescence spectra due to the solvatochromism phenomenon can be used to determine the polarity of an environment. There are several fluorophores which intensity and position of their fluorescence emissions depend on the polarity of their environment. These fluorophores called solvatochromic fluorophores. These fluorophores have an electron-donating and electron-withdrawing groups, connected through an aromatic π-linker moiety.[28] When these dyes absorb light, an intramolecular charge transfer (ICT) from the electron-donating group to the electron-withdrawing group occurs, which produces an excited state with high polarity. In other word, the polarity of the ground state and the excited state are different. The excited state relaxes due to interactions with dipoles of different solvents, which lead to a change in the energy gap between the ground and excited states (Figure 3.7).[29] The final consequence is a shift of emission wavelength toward longer wavelength (with more polar solvent) or shorter wavelength (with less polar solvent) (Figure 3.8).[30]

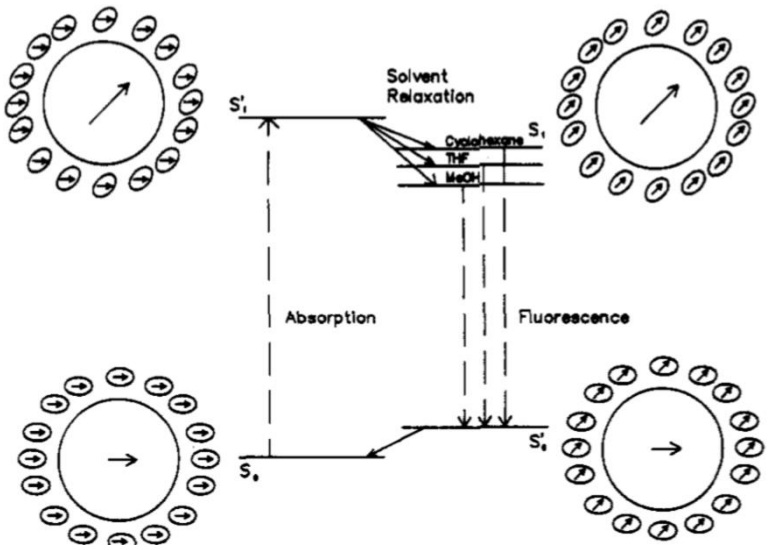

Figure 3.7: The effect of three different solvents with different polarities on the energy of the ground state and excited state. Adapted with permission from ref (29). Copyright © 1990, American Chemical Society

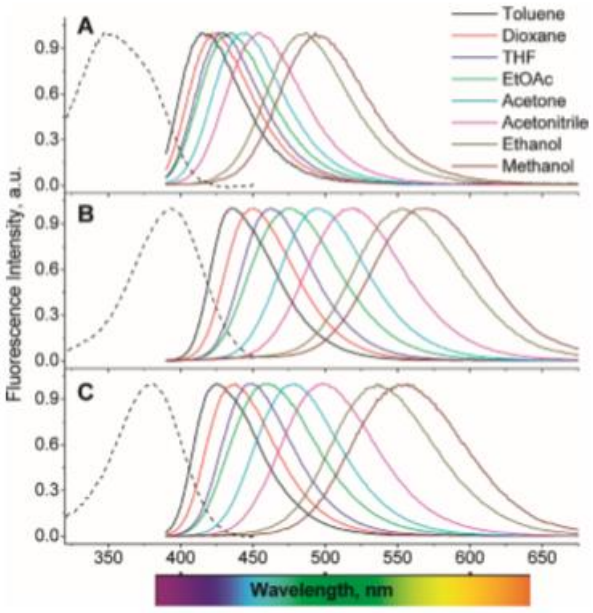

Figure 3.8: Dependency of emission wavelength to different solvent with different polarities is shown for (A) Prodan, (B) FR0 and (C) FR8. Fluorescence spectra is shown as a solid spectra and absorption as a dash spectra. Adapted with permission from ref (30). Copyright © 2010, American Chemical Society

The change in fluorescence spectra due to the solvatochromism phenomenon can be used to determine the polarity of an environment. Lippert−Mataga equation is used to assess the spectra shift due to the solvatochromism event (Equation.3.5).[31]

$$\Delta\nu = (2\Delta f/4\pi\varepsilon_o hca^3)(\mu_e - \mu_g)^2 + \text{constant} \qquad \text{eq.3.5}$$

Here, $\Delta\nu = \nu_{abs} - \nu_{em}$ is Stokes' shift between the of absorption (ν_{abs}) and fluorescence emission (ν_{em}). Δf is solvent orientation polarizability. ε_o is the permittivity of a vacuum. h is the Planck's constant. c is the speed of light in vacuum. a is Onsager cavity radius (the radius of the solvent cavity in which the fluorophore resides). μ_e and μ_g are the dipole moments of the fluorophore in the excited and ground states, respectively. Δf can be calculated using a solvent dielectric constant (ε) and refractive index (n) (Equation 3.6).[31]

$$\Delta f = [(\varepsilon - 1) / (2\varepsilon + 1)] - [(n^2 - 1) / (2n^2 + 1)] \qquad \text{eq.3.6}$$

There are two assumptions for Equation.3.5. First, the excited state for absorption and emission is the same. Second, the energy gap between the ground state and the excited state is proportional only to Δf. One of the solvatochromic fluorophores is 5'-carboxytetramethylrhodamine (TAMRA). The chemical structure of TAMRA is shown in Figure 3.9.[32] This solvatochromic fluorophore was tried to be used in Chapter 6 to assess the environmental polarity inside nanoporous films derived from PS-*hv*-PEO.

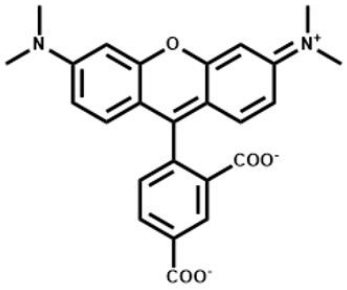

TAMRA

Figure 3.9: Chemical structure of TAMRA molecule.

In this research, a fluorometer was used to measure the density of free COOH groups in nanoporous films derived from PS-*hv*-PEO and to compare the COOH density after and before amidation with propargylamine to calculate the amidation reaction yield. In addition, it was used to evaluate the effect of the solvent on the fluorescence emission of TAMRA inside the nanopore structure of PS-*hv*-PEO.

3.4. Cyclic Voltammetry

Cyclic voltammetry is a versatile technique for acquiring information about processes that involve electron transfer. In cyclic voltammetry, the electrode potential ramps linearly versus time in cyclical phases at specific scan rate Figure 3.10.[33]

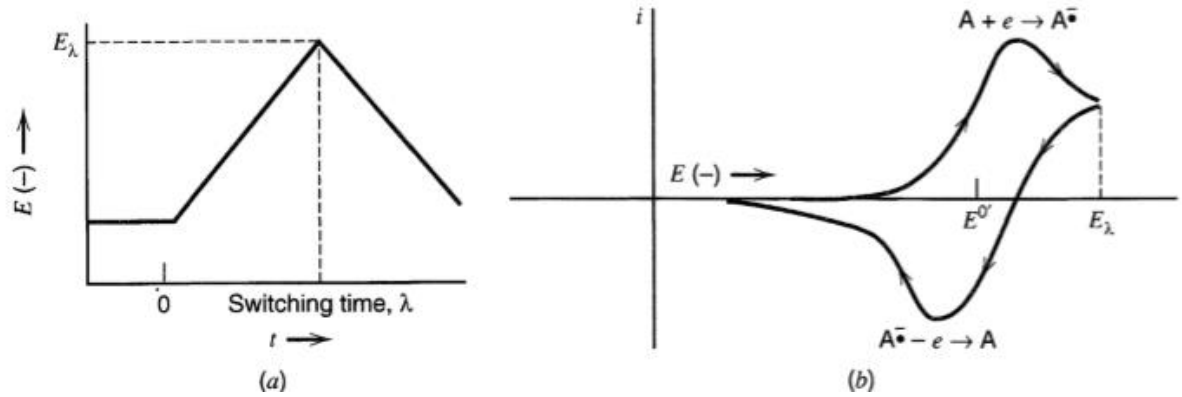

Figure 3.10: (a) Cyclic potential sweep, (b) resulting in cyclic voltammogram. Adapted with permission from ref (33). Copyright © 2000, John Wiley and Sons

In a CV experiment, a range of potential is applied between the working electrode and reference electrode. At the same time, the current is measured at the working electrode resulting in data that is plotted as current (i) vs. applied potential (E). The fundamental parameters of CV include cathodic peak potential ($E_{p,c}$), anodic peak potential ($E_{p,a}$), cathodic peak current (i_{pc}), anodic peak current (i_{pc}) (Figure 3.11).

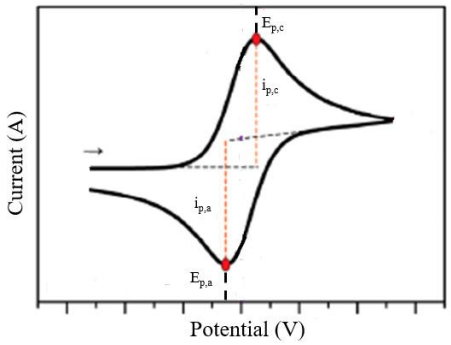

Figure 3.11: Typical voltammogram.

These parameters can be utilized to evaluate the reversibility or irreversibility of electrochemical reaction, electron transfer rate and the redox species concentration. Cyclic voltammograms at different scan rates (v) can be used to get information about diffusion-controlled or adsorption-controlled reactions. There is a linear relationship between i_p (A) vs. $v^{1/2}$ (V s^{-1}) based on Equation 3.7 for a reversible and diffusion-controlled reaction.[33]

$$i_p = (2.69 \times 10^5)\, n^{3/2} A D^{1/2} v^{1/2} C \qquad \text{(eq.3.7)}$$

In this equation, n is the number of electrons involved in the redox process, A (cm^2) is the area of the electrode, D ($cm^2\ s^{-1}$) is the diffusion coefficient of the redox species, and C ($mol.cm^{-3}$) is the concentration of the redox species. While for an adsorption-controlled process, there is a linear relation between I_p vs. v according to Equation 3.8.[34]

$$ip = (n^2F^2/4RT).\ A\ \Gamma^* v \qquad \text{(eq.3.8)}$$

where i_p (A) is peak current, F is Faraday's constant (96485 C/mol), Γ^* is the adsorbed species surface coverage in mol. cm^{-2}, R is the gas constant and T is temperature.

Here, cyclic voltammetry was used to assess the properties of electrochemical DNA sensors based on the stem-loop DNA probe, including probe DNA density on the electrode surface, electron transfer rate constant (k), current response magnitude (%SS), sensor reusability and limit of detection.

Laviron method can be used to calculate the electron transfer rate constant (k) and charge transfer coefficient of the reaction (α) through getting a series of cyclic voltammograms. At this method, CVs are obtained at different scan rates then the graph of peak potential (E_p) vs log$v$ is plotted. Figure 3.12 shows the graph of E_p vs log logarithm of scan rate (log$v$) for benzo(c)einnoline.[35]

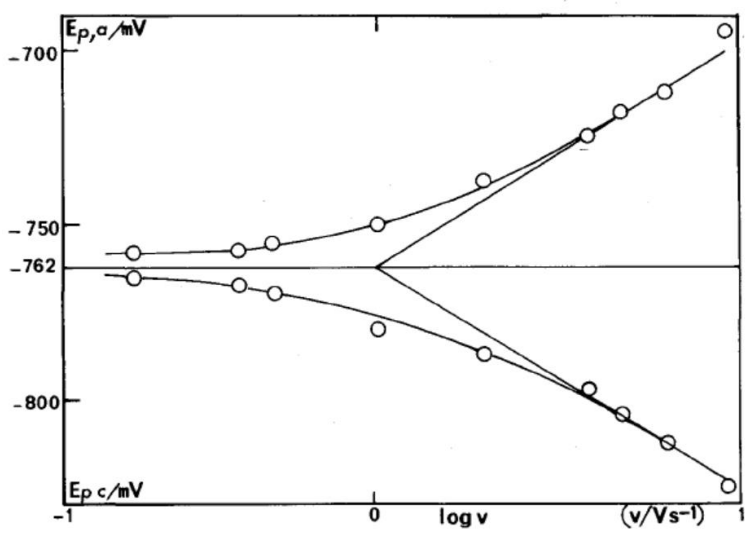

Figure 3.12: The graph of E_p vs log$v$ for benzo(c)einnoline. Adapted with permission from ref (35). Copyright © 1979 Published by Elsevier B.V.

The equation of the upper graph (for anodic peak) is shown in Equation 3.9

$$E_{pa} = a + \frac{2.303RT}{(1-\alpha)nF} logv \qquad \text{(eq.3.9)}$$

The equation of the lower graph (for cathodic peak) is shown in Equation 3.10

$$E_{pc} = b - \frac{2.303RT}{\alpha nF} logv \qquad \text{(eq.3.10)}$$

Here E_{pa} and E_{pc} are anodic and cathodic peak potentials, respectively. It is good to mention that calculated α using Equation 3.9 or Equation 3.10 results in exactly the same α value.

The charge transfer coefficient of the reaction (α) can be calculated from the slop of Equation 3.9 or Equation 3.10. Then α can be applied at Equation 3.11 to calculate the electron transfer rate constant. Equation 3.11 is valid only for $\Delta E_p > 200/n$ mV.

$$\log k_s = \alpha \log(1-\alpha) + (1-\alpha)\log\alpha - \log(\frac{RT}{nFv}) - \frac{\alpha(1-\alpha)nF\Delta E_p}{2.3\,RT} \qquad \text{(eq.3.11)}$$

When $\Delta E_p < 200/n$ mV, Equation 3.11 cannot be used to calculate k_s. Laviron method can be applied for electrochemical reactions with different reversibility degrees. However, the

electrochemical reaction should be diffusionless. In this case, the concentration of redox molecules is homogenized, in other words. This method can be applied only for the redox species that are strongly absorbed on the surface, and also absorption must obey Langmuir isotherm.

3.5. X-Ray Photoelectron Spectroscopy (XPS)

XPS is a surface-sensitive method in which X-rays in an ultrahigh vacuum chamber is used to excite photoelectrons from solids. XPS is applicable to get information about the atomic composition of a sample surface (at the parts per thousand range) except for hydrogen and helium, the structure and the oxidation state of the compound. In other word, XPS helps to get an empirical formula, chemical state, and electronic state of the elements existed in a sample. However, the sample should be stable in vacuum condition or get vacuum stability by cooling. Among all of the instrumental techniques for surface analysis, such as Auger electron spectroscopy (AES), secondary ion mass spectrometry (SIMS), XPS is the more quantitative method that can be interpreted easier. Also, it is more informative in point of chemical information.[36] Figure 3.13 shows the three basic parts of XPS instrument including a photon source, an analyzer, and an electron detector.[37]

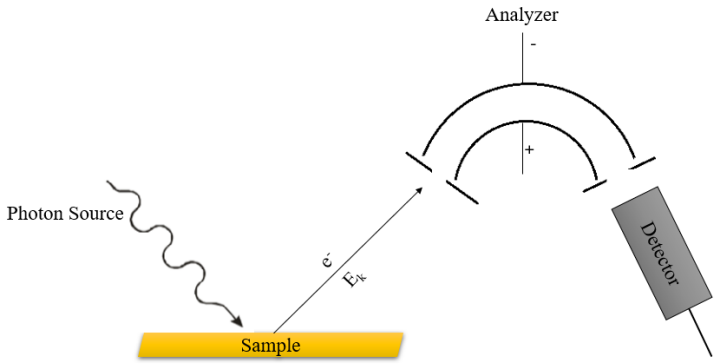

Figure 3.13: Three main parts of a XPS instrument.

XPS is based on the excitation of surface species by X-ray (often aluminum Kα or magnesium Kα). That causes the emission of photoelectrons from the sample surface due to the ejecting of core electron from the atoms that are on the surface.[38] The sample surface (A) is irradiated with a monochromatic X-ray beam. The electrons (e^-) emit from the excited sample (A^+) by the photoelectric effect. The reaction is shown below:

$$A + h\nu \longrightarrow A^{+*} + e^-$$

These emitted electrons have specific kinetic energy (E_k), which can be measured by an electron spectrometer, and shown by a photoelectron spectrum. The kinetic energy of the ejected electron has a direct relationship with a binding energy of the electron. Using the Einstein equation, the binding energy (E_b) of the Fermi level which the electron is emitted from can be obtained using Equation 3.12.[39]

$$E_b = h\nu - E_k - \phi \qquad \text{(eq.3.12)}$$

Here ϕ is work function, which depends on the sample. A chemical shift in E_b is different for each elemental state. It means E_b shifts depending on the chemical state (for example, oxidation state, molecular environment, and lattice parameters) of an emitting element. The shift gives chemical information about the material.[40] Additional peaks in a photoelectron spectrum are generated from Auger electrons: When one inner core electron is ejected, a hole is created in the inner core level. Then, an electron from higher energy level falls into the newly formed hole, leading to a release of energy. This energy is transferred to an electron in the second higher energy level, which leads to the ejection of another electron, which is called Auger electron (Figure 3.14).[41] The kinetic energy of this electron is independent of the energy of the source photon and gives more information about chemical speciation.

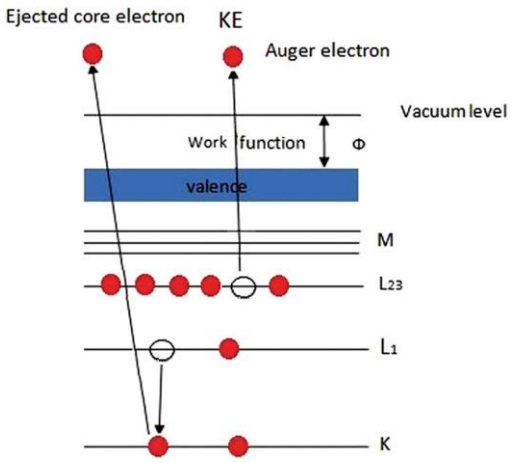

Figure 3.14: X-ray photon causes emission of an electron from the K level. Then, an electron in the L_1 level fills the vacancy in the K level and an Auger electron emitted from the L_{23} level. Adapted with permission from ref (41). Copyright © 2015 Royal Society of Chemistry.

Considering the fact that electron emission causes charge formation on the sample, charge stabilizing is necessary to prevent charge builds up, which can affect the spectrum. The newest spectrometers use charge compensation tools to solve this drawback.

3.6. Reference

(1) Tompkins, H. G. *A User's Guide to Ellipsometry*; Academic Press, New York, 1993.

(2) Azzam, R. M. A.; Bashara, N. M. *Ellipsometry and Polarized Light*; North-Holland: Amsterdam, 1977.

(3) Battie, Y.; Stchakovsky, M.; En Naciri, A.; Akil, S.; Chaoui, N.; Broch, L. Ellipsometry of Colloidal Solutions: New Experimental Setup and Application to Metallic Colloids. *Langmuir* **2017**, *33* (30), 7425–7434. https://doi.org/10.1021/acs.langmuir.7b00490.

(4) Dorywalski, K.; Maciejewski, I.; Krzyżyński, T. Spectroscopic Ellipsometry Technique as a Materials Characterization Tool for Mechatronic Systems—The Case of Composition and Doping Concentration Monitoring in SBN Crystals. *Mechatronics* **2016**, *37*, 33–41. https://doi.org/10.1016/j.mechatronics.2015.11.005.

(5) Ogieglo, W.; Wormeester, H.; Wessling, M.; Benes, N. E. Spectroscopic Ellipsometry Analysis of a Thin Film Composite Membrane Consisting of Polysulfone on a Porous α-Alumina Support. *ACS Appl. Mater. Interfaces* **2012**, *4* (2), 935–943. https://doi.org/10.1021/am2015958.

(6) Cauchy's Dispersion Formula. In *Encyclopedic Dictionary of Polymers*; Gooch, J. W., Ed.; Springer: New York, NY, 2007; pp 167–167. https://doi.org/10.1007/978-0-387-30160-0_2019.

(7) Losurdo, M.; Bergmair, M.; Bruno, G.; Cattelan, D.; Cobet, C.; de Martino, A.; Fleischer, K.; Dohcevic-Mitrovic, Z.; Esser, N.; Galliet, M.; et al. Spectroscopic Ellipsometry and Polarimetry for Materials and Systems Analysis at the Nanometer Scale: State-of-the-Art, Potential, and Perspectives. *J Nanopart Res* **2009**, *11* (7), 1521–1554. https://doi.org/10.1007/s11051-009-9662-6.

(8) *Handbook of Ellipsometry*; Tompkins, H. G., Irene, E. A., Eds.; William Andrew Pub. ; Springer: Norwich, NY : Heidelberg, Germany, 2005.

(9) Binnig, G.; Quate, C. F.; Gerber, C. Atomic Force Microscope. *Phys. Rev. Lett.* **1986**, *56* (9), 930–933. https://doi.org/10.1103/PhysRevLett.56.930.

(10) Franz, C. M.; Puech, P.-H. Atomic Force Microscopy: A Versatile Tool for Studying Cell Morphology, Adhesion and Mechanics. *Cel. Mol. Bioeng.* **2008**, *1* (4), 289–300. https://doi.org/10.1007/s12195-008-0037-3.

(11) Boussu, K.; Van der Bruggen, B.; Volodin, A.; Snauwaert, J.; Van Haesendonck, C.; Vandecasteele, C. Roughness and Hydrophobicity Studies of Nanofiltration Membranes Using Different Modes of AFM. *Journal of Colloid and Interface Science* **2005**, *286* (2), 632–638. https://doi.org/10.1016/j.jcis.2005.01.095.

(12) Hayashi, K.; Iwata, M. Stiffness of Cancer Cells Measured with an AFM Indentation Method. *Journal of the Mechanical Behavior of Biomedical Materials* **2015**, *49*, 105–111. https://doi.org/10.1016/j.jmbbm.2015.04.030.

(13) Zhang, W.; Stack, A. G.; Chen, Y. Interaction Force Measurement between E. Coli Cells and Nanoparticles Immobilized Surfaces by Using AFM. *Colloids and Surfaces B: Biointerfaces* **2011**, *82* (2), 316–324. https://doi.org/10.1016/j.colsurfb.2010.09.003.

(14) Ahmed, N.; Nino, D. F.; Moy, V. T. Measurement of Solution Viscosity by Atomic Force Microscopy. *Review of Scientific Instruments* **2001**, *72* (6), 2731–2734. https://doi.org/10.1063/1.1368856.

(15) Trotsenko, O.; Koestner, R.; Roiter, Y.; Tokarev, A.; Minko, S. Probing Rough Composite Surfaces with Atomic Force Microscopy: Nafion Ionomer in Fuel Cell Electrodes. *Polymer* **2016**, *102*, 396–403. https://doi.org/10.1016/j.polymer.2015.11.021.

(16) Kada, G.; Kienberger, F.; Hinterdorfer, P. Atomic Force Microscopy in Bionanotechnology. *Nano Today* **2008**, *3* (1), 12–19. https://doi.org/10.1016/S1748-0132(08)70011-2.

(17) Chin, C.-J.; Yiacoumi, S.; Tsouris, C. Influence of Metal Ion Sorption on Colloidal Surface Forces Measured by Atomic Force Microscopy. *Environ. Sci. Technol.* **2002**, *36* (3), 343–348. https://doi.org/10.1021/es010905s.

(18) García, R.; Pérez, R. Dynamic Atomic Force Microscopy Methods. *Surface Science Reports* **2002**, *47* (6), 197–301. https://doi.org/10.1016/S0167-5729(02)00077-8.

(19) Jalili, N.; Laxminarayana, K. A Review of Atomic Force Microscopy Imaging Systems: Application to Molecular Metrology and Biological Sciences. *Mechatronics* **2004**, *14* (8), 907–945. https://doi.org/10.1016/j.mechatronics.2004.04.005.

(20) Vahabi, S.; Nazemi Salman, B.; Javanmard, A. Atomic Force Microscopy Application in Biological Research: A Review Study. *Iran J Med Sci* **2013**, *38* (2), 76–83.

(21) Nagao, E.; Dvorak, J. A. Phase Imaging by Atomic Force Microscopy: Analysis of Living Homoiothermic Vertebrate Cells. *Biophys J* **1999**, *76* (6), 3289–3297.

(22) Bar, G.; Thomann, Y.; Whangbo, M.-H. Characterization of the Morphologies and Nanostructures of Blends of Poly(Styrene)-Block-Poly(Ethene-Co-but-1-Ene)-Block-Poly(Styrene) with Isotactic and Atactic Polypropylenes by Tapping-Mode Atomic Force Microscopy. *Langmuir* **1998**, *14* (5), 1219–1226. https://doi.org/10.1021/la9711544.

(23) Xu, Z.; Rollins, A.; Alcala, R.; Marchant, R. E. A Novel Fiber-Optic PH Sensor Incorporating Carboxy SNAFL-2 and Fluorescent Wavelength-Ratiometric Detection. *Journal of Biomedical Materials Research* **1998**, *39* (1), 9–15. https://doi.org/10.1002/(SICI)1097-4636(199801)39:1<9::AID-JBM2>3.0.CO;2-U.

(24) Lindon, J. C.; Tranter, G. E.; Koppenaal, D. *Encyclopedia of Spectroscopy and Spectrometry*, 3rd ed.; Academic Press, 2016.

(25) Skoog, D. A.; Holler, F. J.; Crouch, S. R. *Principles of Instrumental Analysis*, 7th, illustrated ed.; Cengage Learning, 2017.

(26) Lakowicz, J. R. *Principles of Fluorescence Spectroscopy*, 2nd, illustrated ed.; Springer Science & Business Media, New York, 2013.

(27) Buncel, E.; Rajagopal, S. Solvatochromism and Solvent Polarity Scales. *Acc. Chem. Res.* **1990**, *23* (7), 226–231. https://doi.org/10.1021/ar00175a004.

(28) Kovács, S. L.; Nagy, M.; Fehér, P. P.; Zsuga, M.; Kéki, S. Effect of the Substitution Position on the Electronic and Solvatochromic Properties of Isocyanoaminonaphthalene (ICAN) Fluorophores. *Molecules* **2019**, *24* (13). https://doi.org/10.3390/molecules24132434.

(29) Cecil, T. L.; Rutan, S. C. Correction for Fluorescence Response Shifts in Polyaromatic Hydrocarbon Mixtures with an Innovations-Based Kalman Filter Method. *Anal. Chem.* **1990**, *62* (18), 1998–2004. https://doi.org/10.1021/ac00217a019.

(30) Kucherak, O. A.; Didier, P.; Mély, Y.; Klymchenko, A. S. Fluorene Analogues of Prodan with Superior Fluorescence Brightness and Solvatochromism. *J. Phys. Chem. Lett.* **2010**, *1* (3), 616–620. https://doi.org/10.1021/jz9003685.

(31) Lippert, E. Spektroskopische Bestimmung des Dipolmomentes aromatischer Verbindungen im ersten angeregten Singulettzustand. *Zeitschrift für Elektrochemie, Berichte der Bunsengesellschaft für physikalische Chemie* **1957**, *61* (8), 962–975. https://doi.org/10.1002/bbpc.19570610819.

(32) Unruh, J. R.; Gokulrangan, G.; Wilson, G. S.; Johnson, C. K. Fluorescence Properties of Fluorescein, Tetramethylrhodamine and Texas Red Linked to a DNA Aptamer¶. *Photochemistry and Photobiology* **2005**, *81* (3), 682–690. https://doi.org/10.1111/j.1751-1097.2005.tb00244.x.

(33) Bard, A. J.; Faulkner, L. R. *Electrochemical Methods: Fundamentals and Applications*, 2. ed.; Wiley: Hoboken, NJ, 2001.

(34) Elgrishi, N.; Rountree, K. J.; McCarthy, B. D.; Rountree, E. S.; Eisenhart, T. T.; Dempsey, J. L. A Practical Beginner's Guide to Cyclic Voltammetry. *J. Chem. Educ.* **2018**, *95* (2), 197–206. https://doi.org/10.1021/acs.jchemed.7b00361.

(35) Laviron, E. General Expression of the Linear Potential Sweep Voltammogram in the Case of Diffusionless Electrochemical Systems. *Journal of Electroanalytical Chemistry and Interfacial Electrochemistry* **1979**, *101* (1), 19–28. https://doi.org/10.1016/S0022-0728(79)80075-3.

(36) Andrade, J. D. X-Ray Photoelectron Spectroscopy (XPS). In *Surface and Interfacial Aspects of Biomedical Polymers: Volume 1 Surface Chemistry and Physics*; Andrade, J. D., Ed.; Springer US: Boston, MA, 1985; pp 105–195. https://doi.org/10.1007/978-1-4684-8610-0_5.

(37) Hüfner, S. *Photoelectron Spectroscopy: Principles and Applications*; Springer Science & Business Media, 2013.

(38) Sykes, D. Surface Chemical Analysis. In *Springer Handbook of Electronic and Photonic Materials*; Kasap, S., Capper, P., Eds.; Springer Handbooks; Springer International Publishing: Cham, 2017; pp 1–1. https://doi.org/10.1007/978-3-319-48933-9_18.

(39) Lambert, J. B.; McLaughlin, C. D.; Shawl, C. E.; Xue, L. Peer Reviewed: X-Ray Photoelectron Spectroscopy and Archaeology. *Anal. Chem.* **1999**, *71* (17), 614A-620A. https://doi.org/10.1021/ac990608u.

(40) Swartz, W. E. X-Ray Photoelectron Spectroscopy. *Anal. Chem.* **1973**, *45* (9), 788A – 800a. https://doi.org/10.1021/ac60331a001.

(41) Mazzotta, E.; Rella, S.; Turco, A.; Malitesta, C. XPS in Development of Chemical Sensors. *RSC Adv.* **2015**, *5* (101), 83164–83186. https://doi.org/10.1039/C5RA14139G.

Chapter 4 - Sensitization with Stannous Acetate in Dimethyl Sulfoxide for Silver Electroless Deposition

Published as an open-access article: Zeinab Harandizadeh, Jingyi Xie, Mikaela M. Moore, Keith L. Hohn and Takashi Ito, *J. Electrochem. Soc.* **2018**, *165*, D488-D493.

https://iopscience.iop.org/article/10.1149/2.1391810jes

4.1. Contribution of Authors

TI directed the overall project. ZH prepared all the polymer samples deposited by Ag nanoparticles, and measured their ellipsometry and AFM data. JX and KLH measured/analyzed the XPS data of Ag-deposited polymer samples. ZH, MMM and TI individually prepared Ag-deposited SAM samples, and measured their AFM images. TI prepared Ag-deposited μCP SAM samples and measured their AFM images.

4.2. Introduction

This chapter reports electroless deposition on silver nanoparticles on patterned PS-*b*-PMMA using $Sn(OAc)_2$ in DMSO as a new sensitizer in an organic solvent. The thickness of spin coated PS-*b*-PMMA on the surface was exam by spectroscopic ellipsometer. Deposited silver nanoparticles on PS-*b*-PMMA were characterized using atomic force microscopy (AFM) and X-ray photoelectron spectroscopy (XPS). Electroless deposition (ELD) has been widely employed for surface coating with thin layers/nanoparticles of metals such as gold, silver, copper and nickel.[1–3] This wet deposition method is based on the preferential reduction of metal ions by

reducing agents on a catalytic surface. ELD is applicable to the surfaces of non-conductors as well as conductors, because it does not require external electrical current for the reduction of metal ions in contrast to galvanic electrodeposition.[2,3] ELD can be used to fabricate uniform metal layers on surfaces of various geometries, including the inner walls of nanopores[4–7] and colloid particle surfaces.[7,8]

The solution-based method does not require sophisticated instruments, in contrast to dry deposition methods such as physical/chemical vapor deposition and sputtering.[9] In ELD, active catalytic sites are often immobilized on a surface of interest to preferentially reduce precursor metal ions on the surface rather than in the solution. The catalyst immobilization prior to ELD is often carried out by a so-called two-step process based on sensitization and activation, which are known to afford thinner ELD layers than a one-step process.[1–3,10] The sensitization step involves the adsorption of Sn(II) from its solution onto a sample surface. In the subsequent activation step, the Sn(II)-decorated surface is treated by a solution containing Pd^{2+} or Ag^{+} to immobilize metallic catalytic sites on the surface. Here, the adsorbed Sn(II) serves as a reducing agent for these precious metal ions. For example, the reaction with Ag^{+} is described by:[10]

$$Sn(II) + 2Ag^{+} \rightarrow Sn(IV) + 2Ag^{0} \qquad \text{(eq.4.1)}$$

The activated surface is then immersed in a plating solution containing metal ions of interest and appropriate reducing agents for ELD. The reduction of target metal ions is enhanced on the catalytic sites, resulting in the preferential formation of a metal layer on the surface. The sensitization conventionally uses an aqueous stannous chloride ($SnCl_2$) solution containing HCl.[10] The addition of HCl at a relatively high concentration ($\geq$ 0.02 M)[11] is required to reduce the precipitation of the hydroxides of Sn(II) in an aqueous solution.[12] On the other hand,

it has been shown that Sn(II) in an aqueous sensitization solution is partly oxidized by oxygen in air to yield Sn(IV)[13,14] which can form a hydroxide-based adsorption layer incorporating Sn(II).[15] As a result of the hydroxide formation and Sn (II) oxidation, a $SnCl_2$ solution of a relatively high concentration ($\geq$ 0.05 M) is usually used in the sensitization step.[10] In this study, we examined a dimethyl sulfoxide (DMSO) solution of stannous acetate ($Sn(OAc)_2$/DMSO) for sensitization in silver ELD, and compared it with other Sn(II)-based sensitization solutions.

We hypothesized that the use of DMSO as a solvent would enable efficient sensitization in ELD due to the suppressed hydroxide formation, and $Sn(OAc)_2$ would be immobilized on the polymer surface efficiently due to its hydrophobicity. Silver ELD was examined on a nanostructured polymer surface derived from cylinder-forming polystyrene-block-poly(methylmethacrylate) (PS-*b*-PMMA)[16] and on micropatterned thiolate self-assembled monolayers (SAMs).[17,18] We measured the early stage of ELD, which leads to the deposition of silver nanoparticles (Ag-NPs) rather than that of a continuous silver film.[8,19] Ag-NPs are important materials, as they have been used as antibacterial materials,[20] catalysts in organic reactions,[19,21] and substrates for surface enhanced Raman spectroscopy.[22] More importantly, the early-stage experiments will help us realize surface regions where silver ELD preferentially occurs.

4.3. Experimental Section

4.3.1. Chemicals and Materials

PS-*b*-PMMA (PS-*b*-PMMA: M_n = 57,000 g/mol for PS and 25,000 g/mol for PMMA, M_w/M_n 1.07) was purchased from Polymer Source and used without further purification. Stannous chloride ($SnCl_2$; 98%, Acros), stannous acetate ($Sn(OAc)_2$; 95%, Alfa Aesar), potassium sodium tartrate tetrahydrate ($C_4H_4O_6KNa$; Fisher Chemical), silver nitrate ($AgNO_3$; Allied Chemical),

toluene (Fisher Chemical), dimethyl sulfoxide (DMSO; Fisher Chemical), ammonium hydroxide (NH_4OH; Fisher Chemical), hydrochloric acid (HCl; Fisher Chemical), 1,1,1,3,3,3-hexamethyldisilazane (Acros), 11-mercaptoundecanoic acid (MUA; Aldrich), 1-dodecanethiol (DT; Aldrich) and ethanol (Decon Laboratories) were used as received. All aqueous solutions were prepared with water having a resistivity of 18 MΩ (Barnstead Nanopure Systems). Planar Si (100) wafers (p-type) were purchased from University Wafer (South Boston, MA). Premium microscope slides were purchased from Fisher. Gold-coated silicon wafers, which were prepared by sputtering 10 nm of Ti followed by 200 nm of Au onto Si (100) wafers, were purchased from LGA Thin Films (Foster City, CA).

4.3.2. Preparation of UV/AcOH-Treated PS-*b*-PMMA Films

A silicon or glass substrate (ca. 1 × 1 cm^2) was cleaned in an ultrasonic cleaner for 10 min consecutively in aqueous soap solution, deionized water and ethanol, followed by air plasma treatment (PDC-32 G, Harrick Plasma) for 5 min. The cleaned substrates were exposed to the vapor of 1,1,1,3,3,3-hexamethyldisilazane for 20 minutes at room temperature, and then heated in an oven at 120°C for 1 hour. The surface modification with 1,1,1,3,3,3-hexamethyldisilazane increased the hydrophobicity of the substrate surface, resulting in the improved adhesion of a PS-*b*-PMMA thin film. Subsequently, a UV/AcOH-treated PS-*b*-PMMA film was fabricated on the silanized surface according to procedures reported previously.[23,24] Briefly, a PS-*b*-PMMA solution in toluene (0.85 wt%) was spin-cast at a speed of 2000 rpm onto the silanized substrate. The polymer-coated substrate was annealed at 190°C for 60 h under vacuum to induce the microphase separation of the block copolymer. The thickness of the film measured using alpha-

SE spectroscopic ellipsometer (J. A. Woollam) was 30–40 nm. The resulting film-coated substrate was irradiated by UV for 10 min under Ar atmosphere using Novascan PSD-UVTUV-ozone system, and then immersed in glacial acetic acid. Immediately after rinsed with ultrapure water, the resulting substrate coated with a UV/AcOH-treated PS-*b*-PMMA film was used for silver ELD.

4.3.3. Preparation of SAMs.

Gold-coated Si substrates (ca. 1 $\times$ 1 cm^2) were cleaned in an ultrasonic cleaner for 10 min consecutively in aqueous soap solution, deionized water and ethanol, followed by a Novascan PSD-UVT UV-ozone system for 30 min. The cleaned substrates were then immersed in a 1 mM ethanolic solution of MUA or DT overnight to obtain COOH- or CH_3-terminated SAMs, respectively.[17] A micropatterned, COOH-terminated SAM was prepared using microcontact printing (μCP).[18] A PDMS stamp was fabricated using an optical grating as a master. The PDMS stamp was coated with a 5mM ethanolic solution of MUA, dried in a stream of N_2, and then brought into contact with a cleaned gold substrate for 40 sec. After separated from the PDMS stamp, the gold substrate was washed with ethanol, dried in a N_2 stream, and then used for silver ELD.

4.3.4. Silver ELD.

All the solutions employed were prepared immediately before use and were used in a dark room at room temperature (ca. 25 ℃). The first step of silver ELD was sensitization in which a substrate was immersed in a sensitization solution, which was either 0.5 mM $Sn(OAc)_2$ in DMSO, 0.5 mM $SnCl_2$ in DMSO, 0.5, 5 or 50 mM $SnCl_2$ in 0.5 M HCl/H_2O, for 10 min. DMSO was selected as an organic solvent due to its higher solubility to $Sn(OAc)_2$ than alcohols. A substrate

immersed in a DMSO sensitization solution was washed with DMSO followed by ultra-pure water, whereas one sensitized by an aqueous sensitization solution was washed thoroughly with ultra-pure water. The second step was activation in which the sensitized substrate was immersed in an aqueous solution containing 2 mM $AgNO_3$ and 20 mM NH_4OH for 10 min. Subsequently, the substrate was washed thoroughly with ultra-pure water. The last step was silver ELD. For this step, an aqueous silver plating solution was prepared using 1mM $AgNO_3$, 10 mM NH_4 OH and 10 mM $C_4H_4O_6KNa$ (reducing agent).[3] Of note, the presence of the excess NH_3 reduced the rate of ELD. An activated substrate was immersed in the silver plating solution for 10 – 90 min, washed thoroughly with ultrapure water, and then dried under Ar.

4.3.5. Atomic Force Microscopy (AFM) and X-Ray Photoelectron Spectroscopy (XPS) Measurements.

AFM images were obtained by the tapping/phase mode in air, using a Digital Instruments Multimode AFM with Nanoscope IIIa electronics. Tapping mode AFM probes were purchased from Aspire. XPS spectra were collected using a Perkin-Elmer PHI 5400 with an achromatic Al K X-ray source (1486.6 eV) radiation operating at 300 W (15 kV and 20 mA).[25] The base pressure of the chamber was in the order of 10^{-9} Torr. Before testing the samples, the spectrometer was calibrated by setting the binding energies of $Au4f_{7/2}$ and $Cu2p_{3/2}$ to 84.0 and 932.7 eV, respectively. For XPS survey spectra measurements, the analyzer pass energy was set to 44.75 eV and the dwell time was 100 msec. For high-resolution measurement of O1s, $Ag3d_{5/2}$, $Ag3d_{3/2}$, $Sn3d_{5/2}$, $Sn3d_{3/2}$ and C1s spectra, the analyzer pass energy was set to 17.9 eV and the dwell time was 25 msec.

4.4. Results and Discussion

In this study, silver ELD was explored on nanostructured surfaces derived from PS-*b*-PMMA.[16] PS-*b*-PMMA used in this study has a PMMA volume fraction of ~0.3[26] and thus forms cylindrical PMMA microdomains upon microphase separation.[27–30] The cylindrical microdomains in a thin film (30-40 nm thick) were horizontally oriented due to the higher affinity of the hydrophobic PS fragment to the 1,1,1,3,3,3-hexamethyldisilazane-modified surface. The selective removal of the PMMA microdomains via UV/AcOH treatment[16] led to the formation of nanoscale trenches, as shown in a topographic AFM image (Figure 4.1.a). The nanoscale trenches had the width, depth and periodicity of ca. 20 nm, 4–5 nm and 50 nm, respectively. The presence of carboxyl (-COOH) groups was previously reported on UV/AcOH-treated PS-*b*-PMMA surfaces[31–33] at a slightly higher -COOH density on the nanotrenches than the nanoridges.[24] The nanoscale heterogeneity led to their uses as unique platforms for spatially controlled deposition of nanoparticles and proteins.[24,34–37]

4.4.1. Silver ELD on Nanostructured Polymer Surfaces Sensitized with 0.5 mM $Sn(OAc)_2$/DMSO

Upon the sensitization with 0.5 mM $Sn(OAc)_2$/DMSO, a number of nanoscale features were observed on the nanoridges (Figure 4.1b).

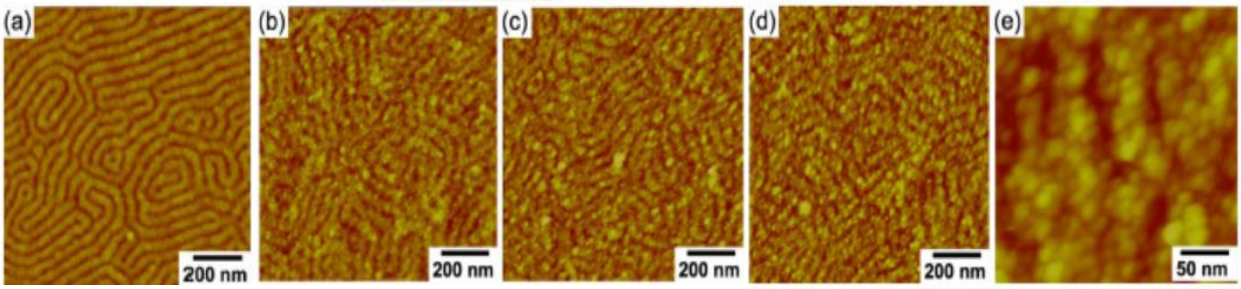

Figure 4.1: Tapping-mode AFM images (1 × 1 μm^2; Δz = 60 nm) of the surfaces of UV/AcOH-treated PS-*b*-PMMA films on glass substrates (a) after the UV/AcOH treatment, (b) after sensitization with 0.5 mM $Sn(OAc)_2$/DMSO, (c) after activation with 2 mM aqueous $[Ag(NH_3)_2]^+$, and (d) after silver ELD for 10 min. (e) A zoomed AFM image (250 × 250 nm^2) from (d).

These features were attributed to a morphological change induced by the solvent-induced polymer swelling deswelling, as indicated by the observation of a similar surface morphology upon immersion in DMSO. However, the morphological change was relatively minor, as indicated by a slight increase in RMS roughness upon the sensitization, from 2.3 nm (Figure 4.1a) to 2.5 nm (Figure 4.1b). The subsequent activation with 2 mM aqueous $[Ag(NH_3)_2]^+$ did not significantly alter the surface morphology (Figure 4.1c), as shown by a small increase in RMS roughness (2.7 nm). Although the AFM image did not clearly show the deposition of catalytic Ag^0 sites, XPS data suggested the stoichiometric reduction of Ag^+ to Ag^0 by Sn(II). Figures 4.2a and 4a shows XPS spectra obtained at a UV/AcOH-treated PS-*b*-PMMA film upon activation.

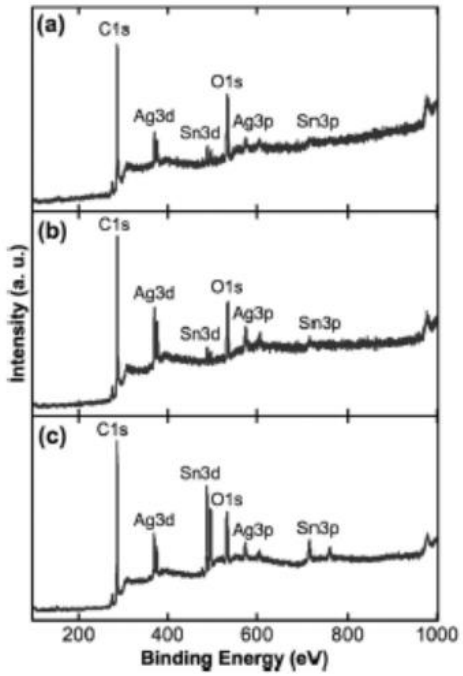

Figure 4.2: XPS survey spectra of Si-supported UV/AcOH-treated PS-*b*-PMMA films on Si substrates. (a) A polymer film sensitized with 0.5 mM $Sn(OAc)_2$/DMSO and then activated with 2 mM aqueous $[Ag(NH3)_2]^+$; (b) A polymer film sensitized with 0.5 mM $Sn(OAc)_2$/DMSO, activated with 2 mM aqueous $[Ag(NH3)_2]^+$, and then immersed in 1 mM $[Ag(NH_3)_2]^+$ and 2 mM $C_4H_4O_6KNa$ for 10 min; (c) A polymer film sensitized with aqueous 50 mM $SnCl_2$ in 0.5 M HCl and then activated with 2 mM aqueous $[Ag(NH3)_2]^+$. The XPS spectra were measured by Dr. Jingyi Xie.

The survey spectrum (Figure 4.2a) indicates the presence of Ag and Sn, in addition to C and O from the polymer and acetate ions (OAc^-). The entire substrate surface was covered with a polymer layer as indicated by the absence of Si peaks in the spectrum. The binding energies for Ag and Sn were similar to those in literature for Ag^0 (369.0 eV),[38] Sn(II) (486.6 eV)[39] and Sn(IV) (487.4 eV).[39] The elemental composition of the activated surface is summarized in Table 4-1.

Table 4-1: Binding Energies (eV) for $Ag3d_{5/2}$, $Ag3d_{3/2}$, $Sn3d_{5/2}$, $Sn3d_{3/2}$ and O1s and Surface Elemental Composition (atom%)[a] of UV/AcOH-Treated PS-*b*-PMMA Films on Si Substrates upon Activation and Silver ELD.

Sensitizer Used before Activation	ELD	$Ag3d_{5/2}$	$Ag3d_{3/2}$	$Sn3d_{5/2}$	$Sn3d_{3/2}$	O1s	Ag/Sn(IV)[b]
(a) 0.5 mM $Sn(OAc)_2$/DMSO	-[c]	368.7 (1.7)	374.7	486.6 (0.2), 487.4 (0.6)[d]	495.6	532.5 (15.2)	2.9
(b) 0.5 mM $Sn(OAc)_2$/DMSO	10 min	369.0 (2.8)	374.9	487.4 (0.6)[d]	495.6	532.6 (12.7)	4.7
(c) 50 mM $SnCl_2/H_2O$	-[c]	368.3 (2.2)	374.1	486.6 (2.1), 487.4 (1.1)[d]	495.4	531.9 (11.3)	2.1

[a] Binding energy for C1s was used as the standard (284.6 eV). Surface elemental composition shown in parentheses was calculated from the relative peak areas for $Ag3d_{5/2}$, $Sn3d_{5/2}$(II, IV), C1s and O1s. Note that the peaks for C1s and O1s were not discussed in details because of significant signals from the underlying polymer. [b] Ratio of the surface elemental compositions of Ag and Sn(IV). [c] No electroless deposition. [d] Surface compositions for Sn(II) and Sn(IV) were shown as the left and right values, respectively, in the parentheses. These values were obtained from the areas of deconvoluted peaks at 486.6 eV and 487.4 eV, as shown in Figure 3.3.

The elemental ratio between Ag^0 and Sn(IV) upon $Sn(OAc)_2$/DMSO sensitization and subsequent activation was close to the theoretical stoichiometric ratio (=2), supporting the formation of Ag^0 by the reduction with Sn(II) immobilized on the polymer surface. It should be noted that the observation of a Sn(II) signal (Figure 4-3a) suggests the presence of unreacted Sn(II) in the activation step. However, the ratio of such unreacted Sn(II) on the $Sn(OAc)_2$/DMSO-sensitized surface was much lower than that on a $SnCl_2/H_2O$-sensitized surface (*vide infra*), suggesting that $Sn(OAc)_2$/DMSO-based sensitization afforded a thinner Sn(II)-based layer on the polymer surface.

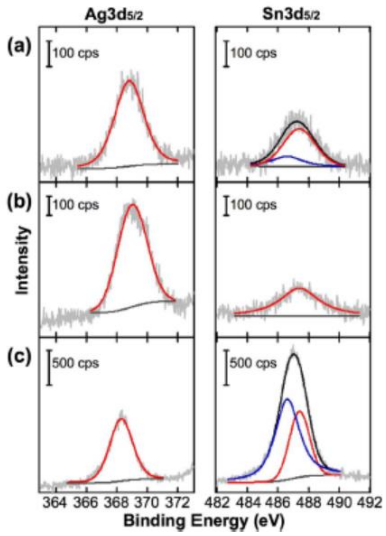

Figure 4.3: $Ag3d_{5/2}$ and $Sn3d_{5/2}$ XPS spectra of Si-supported UV/AcOH treated PS-*b*-PMMA films on Si substrates. (a) A polymer film sensitized with 0.5 mM $Sn(OAc)_2$/DMSO and then activated with 2 mM aqueous $[Ag(NH_3)_2]^+$; (b) A polymer film sensitized with 0.5 mM $Sn(OAc)_2$/DMSO, activated with 2 mM aqueous $[Ag(NH_3)_2]^+$, and then immersed in 1 mM $[Ag(NH_3)_2]^+$ and 2 mM $C_4H_4O_6KNa$ for 10 min; (c) A polymer film sensitized with aqueous 50 mM $SnCl_2$ in 0.5 M HCl and then activated with 2 mM aqueous $[Ag(NH_3)_2]^+$. The $Ag3d_{5/2}$ spectra originate only from Ag^0 as shown in red curves, and the $Sn3d_{5/2}$ spectra could be deconvoluted for Sn(II) and Sn(IV) as shown in blue and red curves, respectively. Note that the intensity scale of $Ag3d_{5/2}$ and $Sn3d_{5/2}$ XPS spectra was the same for each sample. The XPS spectra were measured by Dr. Jingyi Xie.

The Sn(II)-based surface layer contained $Sn(OAc)_2$, as indicated by the O1s peak around 532.5 eV that could be assigned to OAc^- as well as carbonyl groups from the polymer film.[40] Subsequently, an activated film was immersed for silver ELD in an aqueous plating solution containing 1 mM $[Ag(NH_3)_2]^+$ and 2 mM potassium sodium tartrate for 10 min. It was observed that the longer immersion (≥ 2 hours) led to the coverage of the entire surface with a silver layer as well as the formation of Ag colloids in the plating solution. The relatively short ELD time (10 min) was chosen to assess the silver deposition at the early stage. AFM images (Figures 4.1d–1e) show the preferential deposition of highly-dense Ag-NPs (10–20 nm in diameter) onto the nanoscale ridges upon the ELD. The RMS roughness was increased to 3.1 nm in Figure 4.1d. The

surface was not completely covered by Ag, as supported by the observation of Sn signals in its XPS data (Figures 4.2b and 4.3b). However, these XPS spectra clearly showed an increase in surface Ag composition resulting from the silver ELD, as shown by the higher Ag/Sn in Table 4-1. The preferential Ag-NP deposition on the nanoridges suggested that the silver ELD was mainly controlled by the diffusion of Ag^+ toward catalytic Ag^0 sites immobilized on surface. The surface –COOH groups on the polymer surfaces did not control the Sn (II) immobilization, because the Ag-NP deposition was more efficient on the nanoridges with a lower surface –COOH density rather than the nanotrenches.[24]

4.4.2. Silver ELD on Nanostructured Polymer Surfaces Sensitized with 0.5 mM $SnCl_2$/DMSO

The role of OAc^- in the Sn(II)-based sensitization of the polymer surface was investigated using 0.5 mM $SnCl_2$/DMSO. Cl^- is more hydrophilic and a much weaker Lewis base than OAc^-.[41] Sensitization with 0.5 mM $SnCl_2$/DMSO led to the formation of nanoscale surface features (Figure 4.4a) due to the DMSO-induced swelling-deswelling of the polymer film (*vide infra*).

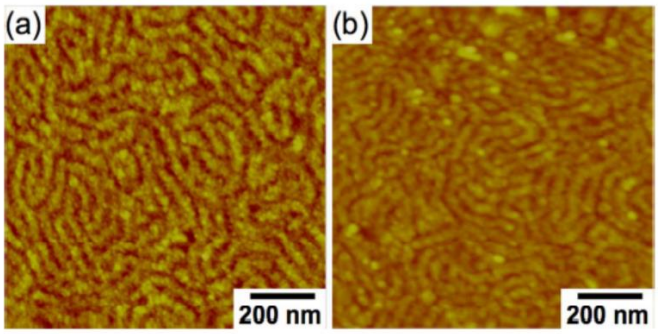

Figure 4.4: Tapping-mode AFM images (1×1 μm^2;Δz = 60 nm) of the surfaces of UV/AcOH-treated PS-*b*-PMMA films on glass substrates (a) after sensitization with 0.5 mM $SnCl_2$/DMSO and (b) after activation and subsequent silver ELD for 10 min.

Subsequently, the $SnCl_2$/DMSO-sensitized surface was activated, and then immersed in an aqueous plating solution for 10 min. In contrast to the $Sn(OAc)_2$/DMSO-sensitized surface (Figures 4.1d–1e), the $SnCl_2$/DMSO-sensitized surface exhibited no significant change in surface morphology except for the deposition of a few particles (Figure 4.4b). The negligible particle deposition was supported by similar RMS roughness (2.7 vs. 2.8 nm) obtained from Figures 4.4a and 4.4b, respectively. These results suggest much lower efficiency in sensitization with $SnCl_2$/DMSO than $Sn(OAc)_2$/DMSO.

4.4.3. Silver ELD on Nanostructured Polymer Surfaces Sensitized with Aqueous $SnCl_2$

We examined the sensitization of the polymer surface with conventional aqueous $SnCl_2$ to investigate the roles of the organic solvent in sensitization with $Sn(OAc)_2$/DMSO. Aqueous $SnCl_2$ solutions were prepared in 0.5 M HCl to reduce the formation for Sn(II/IV) hydroxide in the solution.[10] Of note, $Sn(OAc)_2$ could not be dissolved in aqueous Figure 4.4. Tapping-mode AFM images (1×1 μm^2; Δz = 60 nm) of the surfaces of UV/AcOH-treated PS-*b*-PMMA films on glass substrates (a) after sensitization with 0.5 mM $SnCl_2$/DMSO and (b) after activation and subsequent silver ELD for 10 min. solutions. Figures 4.5a, 4.5b and 4.5c show AFM images of UV/AcOH treated PS-*b*-PMMA films upon sensitization with 0.5 mM, 5 mM and 50 mM $SnCl_2$, respectively.

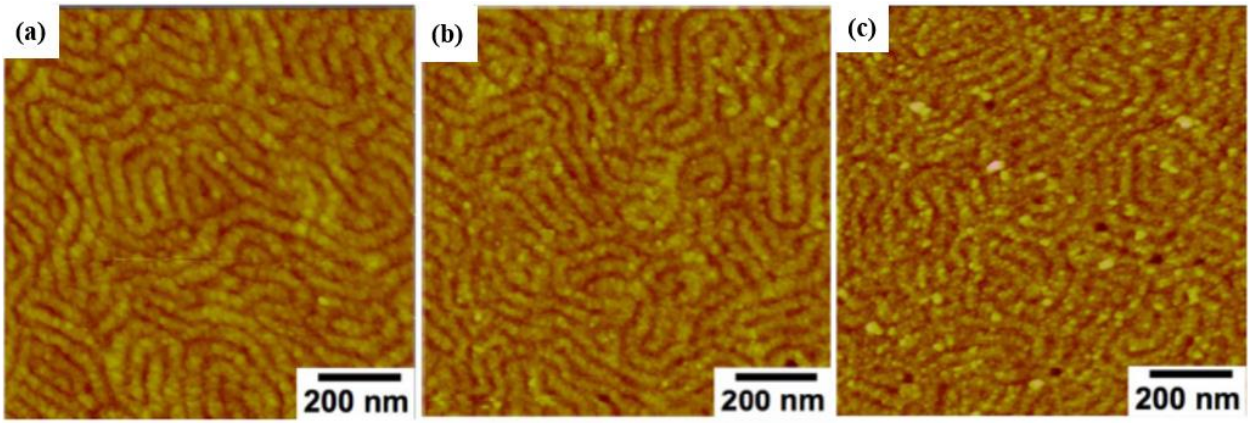

Figure 4.5: Tapping-mode AFM images (1 × 1 μm^2;Δz = 60 nm) of the surfaces of UV/AcOH-treated PS-*b*-PMMA films on glass substrates (a) after sensitization with 0.5 mM $SnCl_2/H_2O$ and (b) after sensitization with 5mM $SnCl_2/H_2O$ (c) after sensitization with 50 mM $SnCl_2/H_2O$

Nanoscale features were not clearly observed on the surface sensitized with 0.5 mM $SnCl_2/H_2O$ (Figure 4.5a), indicating the polymer film was negligibly swollen by the aqueous solution. In contrast, sensitization with 5 mM and 50 mM $SnCl_2/H_2O$ lead to the formation of nanoscale features based on Sn(II/IV)-based hydroxides (Figures 4.5b and 4.5c).[13,14] The observation of the underlying nanotrenches/nanoridges indicates that the hydroxide layers were fairly thin. Subsequent activation with 2 mM $[Ag(NH_3)_2]^+$ did not significantly change the morphology of a surface sensitized with 50 mM $SnCl_2/H_2O$ (Figure 4.7b), but led to the formation of Ag^0 as shown by the observation of a Ag^0 peak in XPS spectra (Figures 4.2c and 4.3c). The Ag/Sn(IV) ratio of this sample was close to 2 (Table 4-1), indicating the formation of Ag^0 based on Reaction 4.1. However, a larger portion of Sn(II) was unreacted with Ag^+ as compared to a $Sn(OAc)_2$/DMSO-sensitized surface, reflecting the incorporation of Sn(II) inside a thicker hydroxide-based layer. The formation of the hydroxide layer was supported by the observation of an O1s peak at 531.9 eV[42] instead of 532.5 eV on $Sn(OAc)_2$/DMSO-sensitized surfaces (Table4-1), the latter of which was associated with the carbonyl groups of OAc^- and the polymer film (vide supra). Importantly, the higher Sn(II) concentration was necessary for efficient sensitization of the

polymer surface with $SnCl_2/H_2O$ as compared to $Sn(OAc)_2$/DMSO. Ag-NPs were negligibly deposited on a polymer surface sensitized with 0.5 mM $SnCl_2/H_2O$ (Figure 4. 5b) in spite of the use of the same nominal Sn(II) concentration as $Sn(OAc)_2$/DMSO. In contrast, polymer surfaces sensitized with 5 and 50 mM $SnCl_2/H_2O$ showed the deposition of Ag-NPs having diameters of *ca*. 40 nm (Figures 4.6b–6c and 4.7c–7d). The RMS roughness obtained from Figures 4.6b and 3.7c was significantly larger (6.1 and 5.1 nm, respectively) than those from sensitized/activated surfaces (<3 nm). Sensitization with 50 mM $SnCl_2$ /H_2O led to deposition of the higher density of Ag-NPs (Figure 3.7d) than that with 5 mM $SnCl_2/H_2O$ (Figure 4.6c). However, it was unclear whether these Ag-NPs were deposited onto the nanotrenches or nanoridges, because the particle sizes were larger than the nanotrench/nanoridge widths. The observation of larger Ag-NPs via sensitization with 5 mM and 50 mM $SnCl_2/H_2O$ as compared with $Sn(OAc)_2$/DMSO may reflect the formation of larger catalytic Ag^0 sites upon activation due to the higher areal density of Sn(II) in the thicker hydroxide layer.

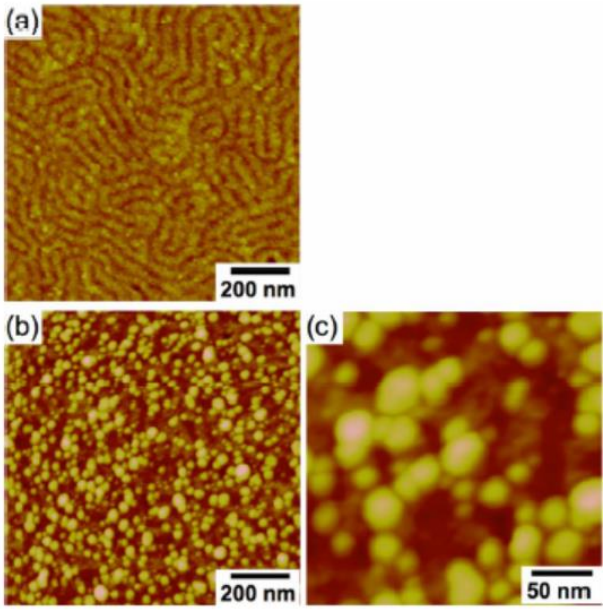

Figure 4.6: Tapping-mode AFM images (1 × 1 μm^2; Δz = 60 nm) of the surfaces of UV/AcOH-treated PS-*b*-PMMA films on glass substrates (a) after sensitization with 5 mM$SnCl_2/H_2O$and (b) after activation with 2 mM aqueous $[Ag(NH_3)_2]^+$ and subsequent silver ELD for 10 min. (c)A zoomed AFM image (250 × 250 nm^2) from (b).

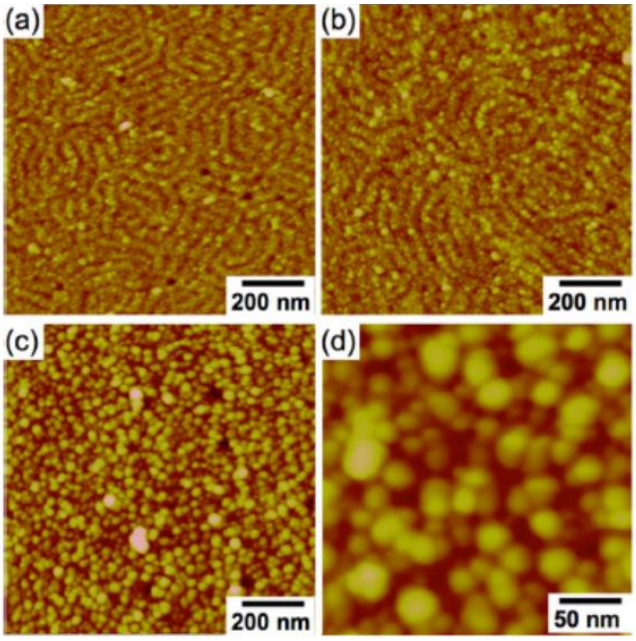

Figure 4.7: Tapping-mode AFM images (1 × 1 μm^2;Δz = 60 nm) of the surfaces of UV/AcOH-treated PS-*b*-PMMA films on glass substrates (a) after sensitization with 50 mM $SnCl_2/H_2O$, (b) after activation with 2 mM aqueous $[Ag(NH_3)_2]^+$, and (c) after silver ELD for 10 min. (d) A zoomed AFM image (250 × 250 nm^2) from (c).

4.4.4. Silver ELD on SAM Surfaces Sensitized with 0.5 mM $Sn(OAc)_2$/DMSO

In addition to nanostructured polymer surfaces derived from UV/AcOH-treated PS-*b*-PMMA, silver ELD was examined on thiolate SAMs to investigate the roles of surface –COOH groups in $Sn(OAc)_2$/DMSO-based sensitization. ELD on thiolate SAMs were previously investigated to examine metal deposition controlled by surface functional groups.[43–45] In this study, COOH and CH_3-terminated SAMs from MUA and DT were used to clarify reasons behind the more efficient sensitization of the COOH terminated polymer surface[24,31–33] with $Sn(OAc)_2$/DMSO (Figure 4.1) than $SnCl_2$/DMSO (Figure 4.4). OAc^- is known to behave as a Lewis base in organic solution as indicated by the enhanced deprotonation of acidic groups,[33,41,46]

and $Sn(OAc)_2$ would be hydrophobic as shown by its poor solubility in water and alcohols (*vide supra*). It was found that $Sn(OAc)_2$/DMSO-based sensitization led to negligible deposition of Ag-NPs on these SAMs upon 10-min ELD (data not shown). The crystalline-like surfaces of the SAMs,[17] in contrast to the solvent-swellable polymer film,[26] could be the reason behind the inefficient sensitization with $Sn(OAc)_2$/DMSO. In addition, micropatterned MUA SAMs fabricated via μCP on Au surfaces were used to investigate the roles of surface functional groups in silver ELD. AFM images of such SAMs (Figures 4.8a–8b) showed equally spaced lines formed from COOH-terminated monolayers on a gold substrate, which corresponded to the average pitch of the optical gratings. Upon silver ELD for 90 min, nanoscale particles corresponding to Ag-NPs were observed (Figures 4.8c–8d). Deposition of Ag-NPs were similarly observed on COOH-terminated SAM and on unmodified gold surfaces (Figures 4.8b and 4-8d), indicating that sensitization with $Sn(OAc)_2$/DMSO was not preferential to the COOH-terminated surface. These results indicated that the efficient $Sn(OAc)_2$/DMSO-based sensitization of the UV/AcOH-treated PS-*b*-PMMA surface was not primarily due to the Lewis basicity of OAc^-. It was postulated that the more efficient sensitization was attributable to the partitioning of $Sn(OAc)_2$ into the solvent-swollen surface region of the polymer film that comprised intrinsically flexible polymer chains.[47] Sensitization with $SnCl_2$/DMSO was not efficient on the polymer surface because of the stronger solvation of Sn(II) and Cl^- by DMSO, which prevented the partitioning into the surface region.

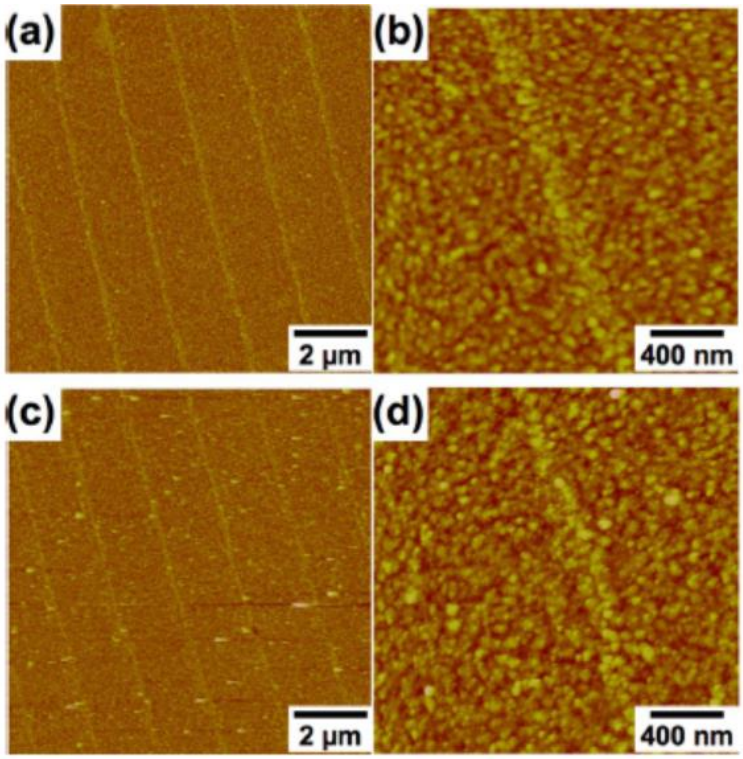

Figure 4.8: (a, b) Tapping-mode AFM images of periodic microscale lines with COOH-terminated SAMs formed on a Au substrate using μCP. (c, d) Tapping mode AFM images of the micropatterned surfaces after $Sn(OAc)_2$/DMSO based sensitization, activation and silver ELD for 90 min. Scale: 10 × 10 μm^2, Δz = 50 nm for (a) and (c); 2 × 2 μm^2, Δz = 30 nm for (b) and (d). The data were obtained by Dr. Takashi Ito.

4.6. Conclusions

In this work, we showed that $Sn(OAc)_2$/DMSO was applicable for the efficient sensitization of nanostructured polymer surfaces for silver ELD. The sensitization of a PS-*b*-PMMA-derived surface with $Sn(OAc)_2$/DMSO was efficient at a low Sn(II) concentration (0.5 mM) as compared to conventional $SnCl_2/H_2O$. The high efficiency could originate from reduced hydroxide formation for Sn(II) in aprotic DMSO and also from the partitioning of $Sn(OAc)_2$ into a solvent swollen polymer surface, as suggested from the negligible sensitization with $SnCl_2$/DMSO and also from the inefficient sensitization of SAM surfaces. Sensitization with $Sn(OAc)_2$/DMSO may be applicable for ELD of various metals such as Pd and Au.[1–3]

4.7. References

(1) Mallory, G. O.; Hajdu, J. B.; American Electroplaters and Surface Finishers Society. *Electroless Plating: Fundamentals and Applications*, Repr. ed.; AESF ; Orlando, Fla., 1990.

(2) Paunovic, M.; Schlesinger, M. *Fundamentals of Electrochemical Deposition, 2ndEdition*, 2nd edition.; John Wiley & Sons: Hoboken, NJ, 2006.

(3) Schlesinger, M.; Paunovic, M. *Modern Electroplating*, Fifth Edition.; JohnWiley & Sons: Hoboken, NJ, 2010.

(4) Menon, V. P.; Martin, C. R. Fabrication and Evaluation of Nanoelectrode Ensembles. *Anal. Chem.* **1995**, *67* (13), 1920–1928. https://doi.org/10.1021/ac00109a003.

(5) Martin, C. R. Membrane-Based Synthesis of Nanomaterials. *Chem. Mater.* **1996**, *8* (8), 1739–1746. https://doi.org/10.1021/cm960166s.

(6) Baker, L. A.; Jin, P.; Martin, C. R. Biomaterials and Biotechnologies Based on Nanotube Membranes. *Crit. Rev. Solid State Mater. Sci.* **2005**, *30* (4), 183–205. https://doi.org/10.1080/10408430500198169.

(7) Pérez-Page, M.; Yu, E.; Li, J.; Rahman, M.; Dryden, D. M.; Vidu, R.; Stroeve, P. Template-Based Syntheses for Shape Controlled Nanostructures. *Adv. Colloid Interface Sci.* **2016**, *234*, 51–79. https://doi.org/10.1016/j.cis.2016.04.001.

(8) Kobayashi, Y.; Salgueiriño-Maceira, V.; Liz-Marzán, L. M. Deposition of Silver Nanoparticles on Silica Spheres by Pretreatment Steps in Electroless Plating. *Chem. Mater.* **2001**, *13* (5), 1630–1633. https://doi.org/10.1021/cm001240g.

(9) Lakhtakia, A.; Martín-Palma, R. J. *Engineered Biomimicry*; Elsevier, 2013. https://doi.org/10.1016/C2011-0-06814-X.

(10) Wei, X.; Roper, D. K. Tin Sensitization for Electroless Plating Review. *J. Electrochem. Soc.* **2014**, *161* (5), D235–D242. https://doi.org/10.1149/2.047405jes.

(11) Chang, S.; Combs, Z. A.; Gupta, M. K.; Davis, R.; Tsukruk, V. V. In Situ Growth of Silver Nanoparticles in Porous Membranes for Surface-Enhanced Raman Scattering. *ACS Appl. Mater. Interfaces* **2010**, *2* (11), 3333–3339. https://doi.org/10.1021/am100758k.

(12) Cohen, R. L.; West, K. W. Solution Chemistry and Colloid Formation in the Tin Chloride Sensitizing Process. *J. Electrochem. Soc.* **1972**, *119* (4), 433–438. https://doi.org/10.1149/1.2404224.

(13) Cohen, R. L.; D'Amico, J. F.; West, K. W. Mössbauer Study of Tin(II) Sensitizer Deposits on Kapton. *J. Electrochem. Soc.* **1971**, *118* (12), 2042–2046. https://doi.org/10.1149/1.2407909.

(14) Przyłuski, J.; Kasprzak, M.; Bieliński, J. Investigations of SnCl2-Sensitizing Solutions for Electroless Plating. *Surf. Coat. Technol.* **1987**, *31* (3), 203–211. https://doi.org/10.1016/0257-8972(87)90073-9.

(15) Feldstein, N.; Weiner, J. A. Contact Angle Measurements of Tin Sensitizing Solutions. *J. Electrochem. Soc.* **1972**, *119* (6), 668–671. https://doi.org/10.1149/1.2404289.

(16) Thurn-Albrecht, T.; Steiner, R.; DeRouchey, J.; Stafford, C. M.; Huang, E.; Bal, M.; Tuominen, M.; Hawker, C. J.; Russell, T. P. Nanoscopic Templates from Oriented Block Copolymer Films. *Adv. Mater.* **2000**, *12* (11), 787–791. https://doi.org/10.1002/(SICI)1521-4095(200006)12:11<787::AID-ADMA787>3.0.CO;2-1.

(17) Love, J. C.; Estroff, L. A.; Kriebel, J. K.; Nuzzo, R. G.; Whitesides, G. M. Self-Assembled Monolayers of Thiolates on Metals as a Form of Nanotechnology. *Chem. Rev.* **2005**, *105* (4), 1103–1170. https://doi.org/10.1021/cr0300789.

(18) Qin, D.; Xia, Y.; Whitesides, G. M. Soft Lithography for Micro- and Nanoscale Patterning. *Nat. Protoc.* **2010**, *5* (3), 491–502. https://doi.org/10.1038/nprot.2009.234.

(19) Çelen, B.; Ekiz, D.; Pişkin, E.; Demirel, G. Green Catalysts Based on Bio-Inspired Polymer Coatings and Electroless Plating of Silver Nanoparticles. *J. Mol. Catal. Chem.* **2011**, *350* (1), 97–102. https://doi.org/10.1016/j.molcata.2011.09.017.

(20) Rizzello, L.; Pompa, P. P. Nanosilver-Based Antibacterial Drugs and Devices: Mechanisms, Methodological Drawbacks, and Guidelines. *Chem. Soc. Rev.* **2014**, *43* (5), 1501–1518. https://doi.org/10.1039/C3CS60218D.

(21) Dong, X.-Y.; Gao, Z.-W.; Yang, K.-F.; Zhang, W.-Q.; Xu, L.-W. Nanosilver as a New Generation of Silver Catalysts in Organic Transformations for Efficient Synthesis of Fine

Chemicals. *Catal. Sci. Technol.* **2015**, *5* (5), 2554–2574. https://doi.org/10.1039/C5CY00285K.

(22) Bell, S. E. J.; Sirimuthu, N. M. S. Quantitative Surface-Enhanced Raman Spectroscopy. *Chem. Soc. Rev.* **2008**, *37* (5), 1012–1024. https://doi.org/10.1039/B705965P.

(23) Maire, H. C.; Ibrahim, S.; Li, Y.; Ito, T. Effects of Substrate Roughness on the Orientation of Cylindrical Domains in Thin Films of a Polystyrene–poly(Methylmethacrylate) Diblock Copolymer Studied Using Atomic Force Microscopy and Cyclic Voltammetry. *Polymer* **2009**, *50* (10), 2273–2280. https://doi.org/10.1016/j.polymer.2009.03.002.

(24) Ibrahim, S.; Ito, T. Surface Chemical Properties of Nanoscale Domains on UV-Treated Polystyrene−Poly(Methyl Methacrylate) Diblock Copolymer Films Studied Using Scanning Force Microscopy. *Langmuir* **2010**, *26* (3), 2119–2123. https://doi.org/10.1021/la902677e.

(25) Ito, T.; Forman, S. M.; Cao, C.; Li, F.; Eddy, C. R.; Mastro, M. A.; Holm, R. T.; Henry, R. L.; Hohn, K. L.; Edgar, J. H. Self-Assembled Monolayers of Alkylphosphonic Acid on GaN Substrates. *Langmuir* **2008**, *24* (13), 6630–6635. https://doi.org/10.1021/la800716r.

(26) Perera, D. M. N. T.; Pandey, B.; Ito, T. Electrochemical Impedance Spectroscopy Studies of Organic-Solvent-Induced Permeability Changes in Nanoporous Films Derived from a Cylinder-Forming Diblock Copolymer. *Langmuir* **2011**, *27* (17), 11111–11117. https://doi.org/10.1021/la202005n.

(27) Bates, F. S.; Fredrickson, G. H. Block Copolymers—Designer Soft Materials. *Phys. Today* **2008**, *52* (2), 32. https://doi.org/10.1063/1.882522.

(28) Park, C.; Yoon, J.; Thomas, E. L. Enabling Nanotechnology with Self Assembled Block Copolymer Patterns. *Polymer* **2003**, *44* (22), 6725–6760. https://doi.org/10.1016/j.polymer.2003.08.011.

(29) Meuler, A. J.; Hillmyer, M. A.; Bates, F. S. Ordered Network Mesostructures in Block Polymer Materials. *Macromolecules* **2009**, *42* (19), 7221–7250. https://doi.org/10.1021/ma9009593.

(30) Ito, T. Block Copolymer-Derived Monolithic Polymer Films and Membranes Comprising Self-Organized Cylindrical Nanopores for Chemical Sensing and Separations. *Chem. – Asian J.* **2014**, *9* (10), 2708–2718. https://doi.org/10.1002/asia.201402136.

(31) Li, Y.; Maire, H. C.; Ito, T. Electrochemical Characterization of Nanoporous Films Fabricated from a Polystyrene−Poly(Methylmethacrylate) Diblock Copolymer: Monitoring the Removal of the PMMA Domains and Exploring the Functional Groups on the Nanopore Surface. *Langmuir* **2007**, *23* (25), 12771–12776. https://doi.org/10.1021/la702756s.

(32) Li, Y.; Ito, T. Surface Chemical Functionalization of Cylindrical Nanopores Derived from a Polystyrene−Poly(Methylmethacrylate) Diblock Copolymer via Amidation. *Langmuir* **2008**, *24* (16), 8959–8963. https://doi.org/10.1021/la800992f.

(33) Li, F.; Diaz, R.; Ito, T. Quantitative Investigation of Surface Functionalization of Cylindrical Nanopores Derived from Polystyrene-Poly(Methylmethacrylate) Diblock Copolymers. *RSC Adv.* **2011**, *1* (9), 1732–1736. https://doi.org/10.1039/C1RA00471A.

(34) Darling, S. B. Directing the Self-Assembly of Block Copolymers. *Prog. Polym. Sci.* **2007**, *32* (10), 1152–1204. https://doi.org/10.1016/j.progpolymsci.2007.05.004.

(35) Olson, D. A.; Chen, L.; Hillmyer, M. A. Templating Nanoporous Polymers with Ordered Block Copolymers. *Chem. Mater.* **2008**, *20* (3), 869–890. https://doi.org/10.1021/cm702239k.

(36) Bang, J.; Jeong, U.; Ryu, D. Y.; Russell, T. P.; Hawker, C. J. Block Copolymer Nanolithography: Translation of Molecular Level Control to Nanoscale Patterns. *Adv. Mater.* **2009**, *21* (47), 4769–4792. https://doi.org/10.1002/adma.200803302.

(37) Hahm, J.-I. Polymeric Surface-Mediated, High-Density Nano-Assembly of Functional Protein Arrays https://www.ingentaconnect.com/content/asp/jbn/2011/00000007/00000006/art00001%3bjsessionid=1vih8385a56ol.x-ic-live-01 (accessed Aug 17, 2019). https://doi.org/info:doi/10.1166/jbn.2011.1341.

(38) Uzunlar, E.; Wilson, Z.; Kohl, P. A. Electroless Copper Deposition Using Sn/Ag Catalyst on Epoxy Laminates. *J. Electrochem. Soc.* **2013**, *160* (12), D3237–D3246. https://doi.org/10.1149/2.039312jes.

(39) Katić, J.; Metikoš-Huković, M.; Šarić, I.; Petravić, M. Semiconducting Properties of the Oxide Films Formed on Tin: Capacitive and XPS Studies. *J. Electrochem. Soc.* **2016**, *163* (5), C221–C227. https://doi.org/10.1149/2.0961605jes.

(40) Briggs, D.; Beamson, G. XPS Studies of the Oxygen 1s and 2s Levels in a Wide Range of Functional Polymers. *Anal. Chem.* **1993**, *65* (11), 1517–1523. https://doi.org/10.1021/ac00059a006.

(41) Odashima, K.; Ito, T.; Tohda, K.; Umezawa, Y. A Systematic Study on the Complexation of Quaternary Ammonium Salts and Neutral Phenols. *Chem. Pharm. Bull. (Tokyo)* **1998**, *46* (8), 1248–1253. https://doi.org/10.1248/cpb.46.1248.

(42) Šeruga, M.; Metikoš-Huković, M.; Valla, T.; Milun, M.; Hoffschultz, H.; Wandelt, K. Electrochemical and X-Ray Photoelectron Spectroscopy Studies of Passive Film on Tin in Citrate Buffer Solution. *J. Electroanal. Chem.* **1996**, *407* (1), 83–89. https://doi.org/10.1016/0022-0728(95)04502-3.

(43) Kumar, A.; Biebuyck, H. A.; Whitesides, G. M. Patterning Self-Assembled Monolayers: Applications in Materials Science. *Langmuir* **1994**, *10* (5), 1498–1511. https://doi.org/10.1021/la00017a030.

(44) Garno, J. C.; Zangmeister, C. D.; Batteas, J. D. Directed Electroless Growth of Metal Nanostructures on Patterned Self-Assembled Monolayers. *Langmuir* **2007**, *23* (14), 7874–7879. https://doi.org/10.1021/la070015b.

(45) Lu, P.; Walker, A. V. Investigation of the Mechanism of Electroless Deposition of Copper on Functionalized Alkanethiolate Self-Assembled Monolayers Adsorbed on Gold. *Langmuir* **2007**, *23* (25), 12577–12582. https://doi.org/10.1021/la702268a.

(46) Papra, A.; Hicke, H.-G.; Paul, D. Synthesis of Peptides onto the Surface of Poly(Ethylene Terephthalate) Particle Track Membranes. *J. Appl. Polym. Sci.* **1999**, *74* (7), 1669–1674.

https://doi.org/10.1002/(SICI)1097-4628(19991114)74:7<1669::AID-APP9>3.0.CO;2-W.

(47) Ediger, M. D.; Forrest, J. A. Dynamics near Free Surfaces and the Glass Transition in Thin Polymer Films: A View to the Future. *Macromolecules* **2014**, *47* (2), 471–478. https://doi.org/10.1021/ma4017696.

Chapter 5 - Block Copolymer-Derived Recessed Nanodisk-Array Electrodes as Platforms for Folding-Based Electrochemical DNA Sensors

Modified with permission from Wiley.

Published as an article: Z. Harandizadeh, T. Ito "Block Copolymer-Derived Recessed Nanodisk-Array Electrodes as Platforms for Folding-Based Electrochemical DNA Sensors",

ChemElectroChem, **2019**, *6*, 5627-5632.

https://onlinelibrary.wiley.com/doi/10.1002/celc.201901562

5.1. Contribution of Authors

TI directed the overall project. ZH prepared all the samples and conducted all the CV measurement. TI and ZH analyzed the data.

5.2. Introduction

Since the first reports in 2003,[1,2] folding-based electrochemical DNA (E-DNA) sensors have attracted considerable interest due to their potential capability of *in vivo* selective detection of target oligonucleotides without the use of exogenous reagents.[3-5] An E-DNA sensor can be fabricated by chemical modification of a gold electrode with a self-assembled monolayer consisting of a thiolated, redox-tagged DNA probe and a hydroxy-terminated alkanethiol.[6,7] The resulting sensor gives a faradaic current signal associated with the accessibility of the redox-active tag to the underlying electrode that is controlled by the hybridization-induced conformational

changes of the DNA probe.[3] An E-DNA sensor can selectively detect a target oligonucleotide at the nM level, which takes advantage of the high selectivity and affinity of the DNA probe to the target oligonucleotide over other interfering species. The reusability of an E-DNA sensor is attributed to the reversibility of the hybridization/dehybridization-induced folding–unfolding behavior of the DNA probe.

However, further improvement of detection sensitivity and selectivity is required to apply E-DNA sensors for the point-of-care diagnosis of trace oligonucleotides such as microRNA in real samples like whole blood.[5] Previously, nanostructured electrodes were used for electrochemical DNA sensors that measured hybridization-based signals using exogenous redox-active reagents.[8] These DNA sensors showed better detection sensitivity and selectivity because of larger faradaic signals originating from the high electrode surface[9,10] and also higher hybridization efficiency[10-12] and mitigated biofouling[13] due to the nanoscale electrode morphology. Nanostructured gold electrodes were also explored as the platforms of folding-based electrochemical sensors including E-DNA[14] and related aptamer-based sensors.[15,16] The resulting aptamer-based sensors gave larger reversible current signals[15] with higher signal-to-noise ratio[16] owing to the larger electrode area. The E-DNA sensors based on nanostructured gold electrodes exhibited the higher electron transfer efficiency of the redox-active tag, but were not reusable possibly due to the obstruction of the refolding of the DNA probe by the nanostructures.[14] Understanding the folding-unfolding behavior of DNA probes in nanospaces is crucial to utilize nanostructured electrodes to improve the performance of E-DNA sensors, and also to design nanopores suitable for DNA separations and detection.[17-19]

On the other hand, electrode coating with a porous polymer membrane could be used to mitigate the biofouling of an electrochemical biosensor for measurements in whole blood.[20-22]

Recessed nanodisk-array electrodes (RNEs), electrodes coated with insulating layers comprising vertically-oriented cylindrical nanopores with uniform diameters, were explored to design unique electrochemical sensors.[23,24] The isoporous layers of RNEs were based on nanoporous anodic alumina or track-etched membranes,[25-27] or were fabricated from cylinder-forming block copolymer thin films upon the selective removal of the cylindrical microdomains.[28,29] RNEs were shown to give high sensitivity in faradaic current measurements owing to the overlapping of analyte diffusion layers developed from individual pores and also a small charging current that reflected the small active electrode area.[30] The isoporous layers of RNEs exhibited size-based[31,32] and charge-based[33,34] permeability for redox-active biomolecules and small ions, respectively. In addition, their nanoporous layers were used as the unique scaffolds of chemical recognition[35-37] and electrochemical signal transduction moieties[38,39] in electrochemical sensing.

In this study, the electrochemical characteristics of RNE-based E-DNA sensors (Figure 5.1) were investigated and compared with those of film-free counterparts.

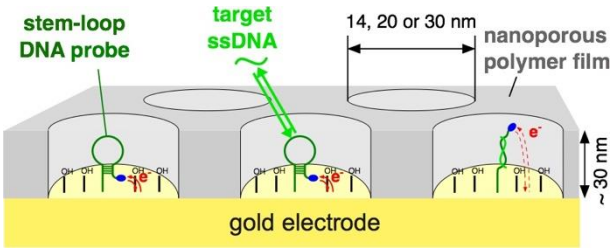

Figure 5.1: RNE-Based E-DNA Sensor

RNEs were fabricated from planar gold substrates coated with nanoporous thin films derived from cylinder-forming diblock copolymers, polystyrene-*block*-poly(methylmethacrylate) (PS-*b*-PMMA).[28,29] The nanoporous films were obtained by the selective removal of cylindrical PMMA microdomains[40] orienting perpendicular to the underlying gold electrodes.[41] The gold surface of

such a RNE was modified with a thiolated stem-loop DNA probe (SLP) having a methylene blue (MB) tag.[42,43] PS-*b*-PMMA-derived nanoporous thin films are suitable to investigate the effects of nanoconfinement on the characteristics of E-DNA sensors for the following reasons.[29] First, the uniform and controllable (10-50 nm) pore diameter permits the systematic investigation of the influences of nanopore diameter on sensor performance. Second, the high pore density (570–1220 pores/μm^2) allows the observation of a large faradaic current from a large number of SLPs. Third, the shallow (*ca*. 30 nm) solution-filled pores facilitate the migration of counter ions, and thus reversible faradaic processes at the bottom electrode surface. The electrochemical characteristics of RNE-based and film-free E-DNA sensors were investigated in solutions containing different concentrations of complementary target single-stranded DNA at different scan rates (v) using cyclic voltammetry (CV). In addition, the size-exclusion property of the nanoporous layer of a RNE was examined by CV measurements in undiluted whole cow blood. Of note, this study focused on the comparison of the characteristics of RNE-based and film-free E-DNA sensors using CV, and did not pursue the improvement of detection sensitivity using square wave voltammetry or AC voltammetry.[43,44]

5.3. Experimental Section

5.3.1. Chemicals and Materials.

Three types of cylinder-forming PS-*b*-PMMA (82K PS-*b*-PMMA: M_n= 57 000 g/mol for PS and M_n = 25 000 g/mol for PMMA, M_w/M_n = 1.07; 57K PS-*b*-PMMA: M_n = 39 800 g/mol for PS and M_n = 17 000 g/mol for PMMA, M_w/M_n = 1.06; 43K PS-*b*-PMMA: M_n = 31 400 g/mol for PS and M_n = 11 500 g/mol for PMMA, M_w/M_n = 1.06) were purchased from Polymer Source and used without further purification. Toluene (Fisher), glacial acetic acid (Fisher), sodium hydroxide

(NaOH, Fisher), sulfuric acid (H_2SO_4, Fisher), 6-mercapto-1-hexanol (C6-OH, Aldrich), tris-(2-carboxyethyl)phosphine hydrochloride (TCEP, Aldrich), tris(hydroxymethyl)aminomethane (Tris, Sigma), hydrochloric acid (Fisher), agar (Sigma), sodium chloride (Fisher), calcium chloride **(**Fisher**),** potassium chloride (Fisher) and magnesium chloride (Fisher) were used as received. A thiolated, MB-tagged SLP and complementary target single-stranded DNA (Biosearch Technologies)[42,43] were used as received. The sequences of them are as follows:

SLP: 5´-HO-$(CH_2)_6$-S-S-$(CH_2)_6$-CCG TTA CGC CAC CAG CTC CAA ACG G-C_7-NH-MB-3´

Target DNA: 5´-TTG GAG CTG GTG GCG TA-3´

Gold-coated silicon wafers, which were prepared by sputtering 10 nm of Ti followed by 200 nm of Au onto Si (100) wafers, were purchased from LGA Thin Films (Foster City, CA). All aqueous solutions were prepared with water having a resistivity of 18 MΩ (Barnstead Nanopure systems). A whole cow blood sample (Martin Purefoods; ingredients: beef blood and sodium citrate) was purchased at a local grocery store.

5.3.2. E-DNA Sensor Preparation.

RNEs based on PS-*b*-PMMA-derived nanoporous films were prepared according to a procedure reported previously.[32,33] Briefly, thin PS-*b*-PMMA films were prepared by spin-coating (2000 rpm, 30 sec) from its toluene solution (0.6 wt%) on gold-coated silicon wafers cleaned by a Novascan PSD-UVT UV-ozone system for 60 min. The film-coated substrates were annealed under vacuum at 170 °C for 60 hours to obtain cylindrical microdomains oriented perpendicular to the underlying substrates.[41] Nanoporous thin films were obtained by the selective removal of the cylindrical PMMA microdomains by UV irradiation for 10 min under Ar atmosphere and subsequent immersion in glacial acetic acid.[40] The surface morphologies of the resulting

nanoporous films were measured by tapping mode in air, using a Digital Instruments Multimode AFM with Nanoscape IIIa electronics. Tapping mode AFM probes were purchased from Aspire. The nanopore diameters and densities of these films were very similar to those reported previously (Table 5-1).[45]

Table 5-1: Pore Diameter, Surface Probe Density (Γ^*), Apparent Electron Transfer Rate Constants before (k_s) and after Hybridization (k_s') at 1 µM Target DNA, Signal Suppression (SS) at 1 µM Target DNA, the Limit of Detection (LOD) of the E-DNA Sensors, and Dissociation Constant (K_D) between SLP and Target DNA for the E-DNA Sensors

E-DNA sensors	Pore diameter (nm)[a]	Γ^* (molecules/cm^{-2})[b,c,d]	k_s (s^{-1})[b,e,f]	k_s' (s^{-1})[b,e,g]	SS (%)[b,e,h]	LOD (nM)[b,i]	K_D (nM)[b,i,j]
Film-free	-	(2.6 ± 0.2) x 10^{12}	143 ± 10	112 ± 11	73 ± 2	4.2 ± 1.6	84 ± 79
82K-RNE	30 ± 3	(2.6 ± 0.9) x 10^{12}	175 ± 26	121 ± 17	71 ± 3	0.4 ± 0.1	56 ± 17
57K-RNE	20 ± 3	(2.0 ± 0.5) x 10^{12}	190 ± 16	135 ± 11	74 ± 3	0.9 ± 0.4	77 ± 50
43K-RNE	14 ± 1	(4.2 ± 1.2) x 10^{12}	201 ± 9	145 ± 19	68 ± 3	1.2 ± 1.1	60 ± 24

[a] Taken from Ref. 45. [b] Prepared from a mixture of 200 µM SLP (1 µL) and 10 mM TCEP (1 µL). [c] Average ± standard error (80% confidence interval) obtained at nine film-free, seven 82K-RNE-based, ten 57K-RNE-based and nine 43K-RNE-based E-DNA sensors. [d] Determined from the amount of charge associated with MB reduction at 0.02 V/s and gold surface area estimated from the film porosity. [e] Average ± standard error (80% confidence interval) obtained at five film-free, three 82K-RNE-based, six 57K-RNE-based and four 43K-RNE-based E-DNA sensors. [f] Obtained in the absence of target DNA using Eq (2). [g] Obtained in the presence of 1 µM target DNA using Eq (2). [h] Determined from cyclic voltammograms at 10 V/s measured in the absence and presence of 1 µM target DNA using Eq (3). [i] Average ± standard error (80% confidence interval) obtained at four film-free, four 82K-RNE-based, four 57K-RNE-based and five 43K-RNE-based E-DNA sensors. [j] Determined from the amount of charge associated with MB reduction at 10 V/s using Eqs (4.5) and (4.6).

The resulting RNE or film-free gold electrode was immobilized at the bottom of an electrochemical cell as reported previously.[33] Subsequently, the electrodes were electrochemically cleaned by sweeping the electrode potential in 0.5 M NaOH between -0.35 and -1.35 V (vs. Ag/AgCl), in 0.5 M H_2SO_4 between 0 and +1.5 V (vs. Ag/AgCl), and then in 0.05 M H_2SO_4 between 0 and +1.5 V (vs. Ag/AgCl).[46] In general, E-DNA sensors were prepared according to the following procedure.[42,43] First, a mixture of 200 µM SLP (1 µL) and 10 mM TCEP (1 µL) was

incubated for 1 h, and then was diluted by 100 µL of a physiological buffer solution containing 20 mM Tris-HCl (pH 7.4), 140 mM NaCl, 5 mM KCl, 1 mM $MgCl_2$ and 1 mM $CaCl_2$ (Phys2).[42] The SLP concentration of the resulting SLP-TCEP-Phys2 solution was 1 µM. Film-free sensors were also fabricated in SLP-TCEP-Phys2 solutions containing 0.17, 0.33 or 0.5 µM SLP to investigate the effects of surface SLP density on sensor response. A cleaned RNE-based or film-free electrode was incubated in the SLP solution for 1 h, washed with ultrapure water, and then incubated in 2 mM aqueous C6-OH solution (1 mL) overnight to obtain an E-DNA sensor.

5.3.3. Electrochemical Measurements.

CV measurements were carried out at room temperature (*ca*. 25 °C) in a three-electrode system containing a Ag/AgCl reference electrode (with 3 M KCl) and a Pt counter electrode using a CH Instruments model 618B or 720C electrochemical analyzer. A Ag/AgCl reference electrode (with 1 M KCl) was prepared using a plastic micropipette with a salt bridge based on 2 wt% agar containing 1 M KCl[48] for CV measurements in whole cow blood. An E-DNA sensor was stabilized by recording cyclic voltammograms in Phys2 buffer (2.00 mL) every 5 min until very similar cyclic voltammograms were obtained in three consecutive measurements. After the stabilization, CV measurements were carried out at different target DNA concentrations adjusted by stepwise addition of stock solutions. For regeneration, the sensor was rinsed with ultrapure water for 30 sec. CV measurements in whole cow blood were carried out after stabilization in Phys2 buffer. The response time of these film-free and RNE-based E-DNA sensors was similarly slow (≥ 15 min) as with E-DNA sensors based on the same SLP,[42] possibly due to the slow hybridization kinetics of the SLP.

Surface SLP density (Γ^* in Table 1) was calculated from the amount of charge (Q) associated with MB reduction in cyclic voltammograms at 0.02 V/s using the following equation:[42]

$$\Gamma^* = \frac{Q}{nFA} \qquad \text{(eq.5.1)}$$

where n is the number of electrons (n = 2 for MB), F is Faraday's constant (96 485 C/mol), and A is the area of the gold surface of the electrode. The gold surface area was estimated from the sensor geometric area defined by the O-ring of a cell (0.65 mm in diameter, 0.33 cm^2)[33] and the porosity of a nanoporous film calculated from pore diameter and density (Table 5-1 and Figure 5.2, respectively).

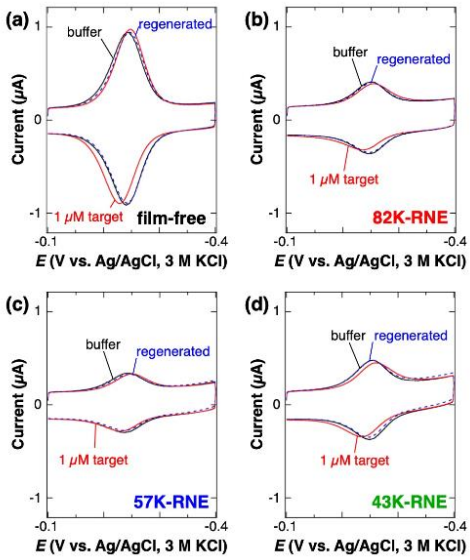

Figure 5.2: Cyclic voltammograms(scan rate: 0.1 V/s) measured at the same E-DNA sensors as those reported in Figure 4.1before hybridization (black solid line),after hybridization at1 μM target DNA(red solid line), and after regeneration (blue dashed line): (a) Film-free, (b) 82K-RNE-based, (c) 57K-RNE-based, and (d) 43K-RNE-based E-DNA sensors. These voltammograms were recorded in Phys2 buffer (pH 7.4) at room temperature (ca. 25 °C).

Meanwhile, we also measured a gold surface area from the amount of charge associated with the reduction of the gold surface oxide obtained in 0.05 M H_2SO_4 using a literature reported value (400 μC/cm^2),[42,47] and calculated surface SLP density (Γ^*_{oxide} in Table 5-2).

Table 5-2: Pore Density, Surface Probe Density Calculated from the Anodic Charge of Surface Gold Oxide (Γ^*oxide), Alpha Values Measured before (a) and after (a') Hybridization at 1 μM Target DNA

E-DNA sensors	Pore density (pores/μm^2)[a]	Γ^*_{oxide} (molecules/cm^{-2})[b,c,d]	α[b,e,f]	α'[b,e,g]
Film-free		$(3.6 \pm 0.3) \times 10^{12}$	0.27 ± 0.01	0.36 ± 0.04
82K-RNE	570 ± 50	$(1.5 \pm 0.5) \times 10^{12}$	0.26 ± 0.03	0.32 ± 0.04
57K-RNE	890 ± 70	$(2.0 \pm 0.5) \times 10^{12}$	0.33 ± 0.02	0.35 ± 0.04
43K-RNE	1220 ± 70	$(1.1 \pm 0.3) \times 10^{12}$	0.31 ± 0.02	0.39 ± 0.03

[a] Taken from Ref [45]. [b] Prepared from a mixture of 200 μM SLP (1 μL) and 10 mM TCEP (1 μL). [c] Average ± standard error (80% confidence interval) obtained at nine film-free, seven 82K-RNE-based, ten 57K-RNE-based and nine 43K-RNE-based E-DNA sensors. [d] Calculated from active electrode area measured from the amount of charge associated with the reduction of surface gold oxide layer in 0.05 M H_2SO_4using Equation (5.1). [e] Average ± standard error (80% confidence interval) obtained at five film-free, three 82K-RNE-based, six 57K-RNE-based and four 43K-RNE-based E-DNA sensors. [f] Obtained in the absence of target DNA using Equation (5.2). [g] Obtained in the presence of 1 μM target DNA using Equation (5.2).

However, Γ^*_{oxide} was not used for discussion, because the cathodic charge of gold surface oxide often offered a very large gold surface area possibly due to solution penetration to the film–electrode interface during the measurement.

Apparent electron transfer rate constant (s^{-1}) before and after hybridization (k_s and k_s', respectively) at 1 μM target DNA was calculated from redox peak separations ($\Delta E_p = E_{p,a} - E_{p,c}$) at potential scan rates (*e.g.*, v = 10 ~ 70 V/s) where $\Delta E_p > 200/n$ (mV) using the following equation:[42,49]

$$\log k_s = \alpha \log(1-\alpha) + (1-\alpha)\log\alpha - \log(\frac{RT}{nFv}) - \frac{\alpha(1-\alpha)nF\Delta E_p}{2.3\,RT} \qquad \text{(eq.5.2)}$$

where α is the electron-transfer coefficient (α and α′ before and after hybridization, respectively; Table 5-2). It should be mentioned that the uncompensated resistance of the film-free and RNE-based sensors was ≤ 40 Ω, and thus the contribution of the Ohmic drop was relatively minor (≤ 10%) for the estimation of k_s and k_s'.

Signal suppression (SS (%)) and signal remaining (SR (%)) are defined by the following equations:[6,50]

$$SS = 100 \times \frac{I_0 - I_s}{I_0} \quad \text{(eq.5.3)}$$

$$SR = 100 \times \frac{I_i}{I_0} \quad \text{(eq.5.4)}$$

where I_0 is the peak current of the MB tag in the physiological buffer prior to the addition of target DNA, I_s is the peak current in a solution containing target DNA, and I_i is the peak current recorded in the *i*th measurement. The limit of detection (LOD) was defined as a target DNA concentration at which a current change (= $I_0 - I_s$) at 10 V/s was equal to 3σ, where σ was the standard deviation of three I_0 values obtained from CV data during the stabilization in Phys2 buffer.

Dissociation constant (K_D) for the target and probe DNA was estimated from Q measured from cyclic voltammograms (v = 10 V/s) at different target DNA concentrations (5 – 1000 nM) using the following two equations under the assumptions that (1) the binding of targets to SLPs follows the Langmuir isotherm,[4,51] (2) the redox processes of the MB tags of hybridized SLPs are negligible,[4] and (3) the concentration of target DNA is not affected by its binding to SLPs:[4]

$$\Gamma = \frac{Q_0 - Q}{nFA} \quad \text{(eq.5.5)}$$

$$\frac{1}{\Gamma} = \frac{K_D}{\Gamma_{max}} \frac{1}{C} + \frac{1}{\Gamma_{max}} \quad \text{(eq.5.6)}$$

where Q_0 is the amount of charge from MB measured prior to the addition of target DNA. Of note, the Langmuir isotherm suggests that, if $\frac{Q_0 - Q}{Q_0}$ can be approximated to SS, the calibration curve of

an E-DNA sensor is linear only at the concentration significantly smaller K_D. Indeed, the linear dynamic range of the calibration was limited to ≤ 25 nM (*vide infra*).

5.4. Results and Discussion

5.4.1. Electrochemical Behavior of RNE-Based E-DNA Sensors in the Absence of Target DNA.

Figure 5.3 depicts cyclic voltammograms obtained at film-free and RNE-based sensors in Phys2 buffer (pH 7.4). These voltammograms show faradaic cathodic and anodic peaks at -0.2 ~ -0.3 V (vs. Ag/AgCl), which can be assigned to the reduction and re-oxidation of the MB tag of the SLP, respectively.[42,43] The redox peak potentials measured at RNE-based sensors (Figure 5.3.b-d) were very close to that at a film-free sensor (Figure 5.3a). These results indicate the successful immobilization of MB-tagged SLPs on PS-*b*-PMMA-derived RNEs. The SLP, which was estimated to have a diameter of *ca*. 3 nm by assuming the formation of a circular 17-base loop,[17] was small enough to penetrate through the nanopores (14, 20 or 30 nm in diameter) and to reach the underlying gold surface.[32]

However, the RNE-based sensors exhibited smaller faradaic currents than the film-free sensors. The smaller currents were mainly attributed to the smaller area of a gold surface exposed at the bottom of the nanopores. Table 5-1 summarizes the Γ^* values of these sensors calculated from porosity-based geometric gold surface area (A) and the amount of MB reduction charge (Q) using equation (5.1). The Γ^* values of 57K- and 82K-RNE-based sensors were similar to that of film-free sensors, indicating that the nanopores did not give significant influence on the diffusion of SLP during the sensor fabrication. On the other hand, the Γ^* value of the 43K-RNE-based sensor

was larger than the other sensors, implying the underestimation of gold surface area that might be caused by the non-ideal morphology of the nanopores.

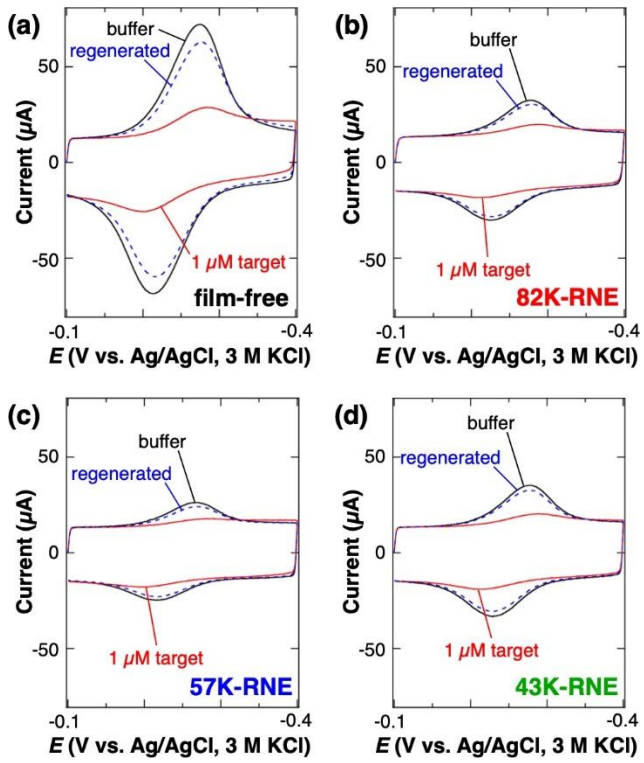

Figure 5.3: Typical cyclic voltammograms (scan rate: 10 V/s) measured at (a) a film-free E-DNA sensor, (b) an 82K-RNE-based E-DNA sensor (30 nm in pore diameter), (c) a 57K-RNE-based E-DNA sensor (20 nm in pore diameter), and (d) a 43K-RNE-based E-DNA sensor (14 nm in pore diameter) before hybridization (black solid line), after hybridization at 1 μM target DNA (red solid line), and after regeneration (blue dashed line). These voltammograms were recorded in Phys2 buffer (pH 7.4) at room temperature (*ca*. 25 °C).

In addition, cyclic voltammograms obtained at RNE-based sensors (Figure 5.3 b-d) exhibited slightly smaller redox peak separation (ΔE_p) than those at film-free sensors (Figure 5.3a), suggesting the more facile electron transfer of the MB tags within the nanopores. Indeed, the RNE-based sensors afforded larger apparent electron transfer rate constants (k_s) than the film-free sensors (Table 5-1). The larger k_s at the smaller nanopores possibly reflected the sterically and/or electrostatically restricted dynamic flexibility[17,25] of anionic SLPs within the negatively-charged

nanopores having surface -COO^- groups[33,52] that held the MB moieties in proximity to the electrode.

5.4.2. Electrochemical Behavior of RNE-Based E-DNA Sensors in the Presence of 1 µM Target DNA.

These RNE-based sensors exhibited a decrease in the faradaic current of the MB tag in the presence of 1 µM target DNA, as with the film-free sensor (Figure 5.3). Signal suppression (SS (%)) in MB reduction current, which is obtained using equation (5.3) and is commonly used to assess the electrochemical response of an E-DNA sensor,[6,42,43] at 1 µM target DNA was similar for the RNE-based and film-free sensors (Table 5-1). The decrease in MB faradaic current was ascribed to an increase in MB–electrode distance that resulted from the hybridization-induced unfolding of the SLP (Figure 5.1, left and right pores).[3] The longer MB–electrode distance led to the reduction of the electron transfer efficiency of the MB tag at the electrode, resulting in the observation of smaller faradaic currents. Indeed, apparent electron transfer rate constant obtained at 1 µM target DNA (k_s', Table 5-1) was smaller than k_s for both the RNE-based and film-free sensors. Interestingly, RNE-based sensors afforded the slightly larger hybridization-induced reduction of apparent electron transfer rate constant, suggesting the restriction of probe orientation and dynamic properties within nanopores (*vide supra*). On the other hand, hybridization-induced current reduction was very small at 0.1 V/s (Figure 5.2), consistent to the facile electron transfer processes of the folded and unfolded SLPs as supported by the large k_s and k_s' values.

The nanoporous films of the RNEs negligibly affected the reversibility of the folding-unfolding property of the SLP (Figure 5.3, blue dashed lines). Figure 5.4 ab shows typical cyclic voltammograms recorded at film-free and 82K-RNE-based sensors upon repeated hybridization at

1 µM target DNA and regeneration with ultrapure water. A slight decrease in MB faradaic currents was observed at both types of sensors. Figure 5.4 c shows signal remaining (SR (%)), which is defined by equation (5.4), after multiple hybridization-regeneration cycles for film-free and RNE-based sensors. The SR data of RNE-based sensors were comparable to those of film-free sensors. The high reusability of RNE-based sensors was in sharp contrast to E-DNA sensors fabricated on nanostructured gold electrodes,[14] and could result from the negligible adsorption of unfolded SLPs onto the negatively-charged nanopore surfaces.

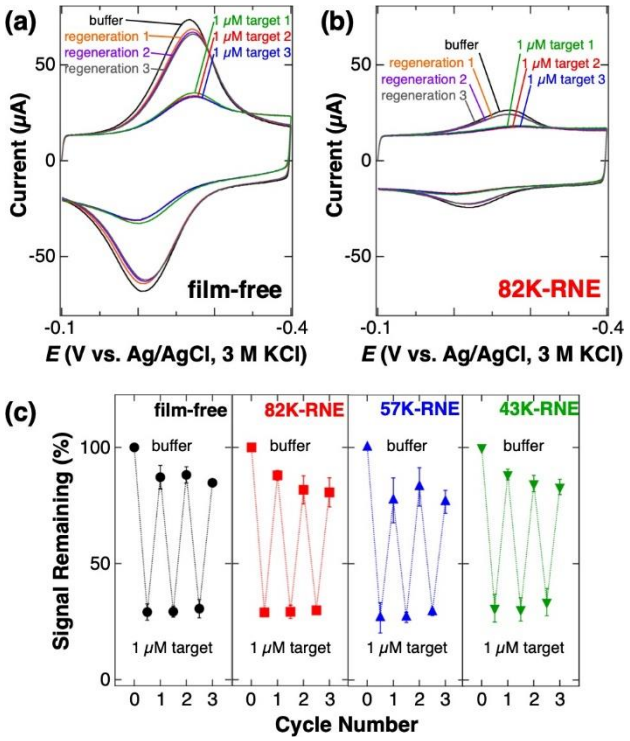

Figure 5.4: Typical cyclic voltammograms (scan rate: 10 V/s) measured at (a) a film-free E-DNA sensor and (b) an 82K-RNE-based E-DNA sensor (30 nm in pore diameter) before hybridization (black) and after repeated hybridization at 1 µM target DNA and regeneration with ultrapure water. These voltammograms were recorded in Phys2 buffer (pH 7.4) at room temperature (*ca*. 25 °C). (c) Signal remaining (%) obtained at three film-free, four 82K-RNE-based, three 57K-RNE-based and four 43K-RNE-based E-DNA sensors upon repeated hybridization and regeneration processes. The error bars represent the 80% confidence intervals.

5.4 .4. Electrochemical Responses of RNE-Based E-DNA Sensors at Different Target DNA Concentrations.

Subsequently, the effects of target DNA concentration on SS (%) were investigated at RNE-based and film-free E-DNA sensors. Figure 5.5 a-d shows cyclic voltammograms measured at film-free and RNE-based sensors at different target DNA concentrations (0 ~ 1000 nM). The RNE-based sensors clearly showed a decrease in faradaic current at a much lower concentration (1 ~ 10 nM; Figure 5.5b-d) than the film-free sensor (10 ~ 25 nM; Figure 5.5a). The higher detection sensitivity of the RNE-based sensors was supported by the relationships between SS (%) and the logarithm of target DNA concentration (Figure 5.5e) and also by the lower LOD (80% confidence interval) of RNE-based sensors than that of film-free sensors (Table 5-1). The improvement of the detection sensitivity was attributable to the steric and/or electrostatic restriction of the dynamic flexibility and orientation of the SLPs[17,25] within the nanopores having surface -COO^- groups[33,52] (*vide supra*). In addition, the enhancement of hybridization efficiency[10-12] within the RNE nanopores made some contribution to the sensitivity improvement, as shown by the slightly smaller K_D values for the RNE-bases sensors as compared with the film-free sensors (Table 5-1). The effects of I^* on K_D and LOD were however unclear at the I^* range examined due to the large variation of the data of different sensors (Figure 5.6), in contrast to a previous report that showed higher K_D and lower LOD at E-DNA sensors with lower I^*.[53] Unfortunately, the effects of pore diameter on sensor performance were not clearly shown in Figure 5.5e and Table 5-1 due to the large variation of the electrochemical responses of different sensors. It should be mentioned that the corresponding calibration curves (Figure 5.7) exhibited linear dynamic ranges at the target DNA concentrations of < 25 nM, as anticipated from the adsorption-based mechanism that could be assessed by the Langmuir isotherm (*vide supra*).[4] These results indicate that RNEs can be used

to improve the detection sensitivity of folding-based electrochemical sensors. We infer that the confined environment in the nanopores not only enhances the hybridization, but also reduces faradaic currents from the MB tags of hybridized DNA probes due to the steric/electrostatic effects,[17,25] leading to the lower LOD.

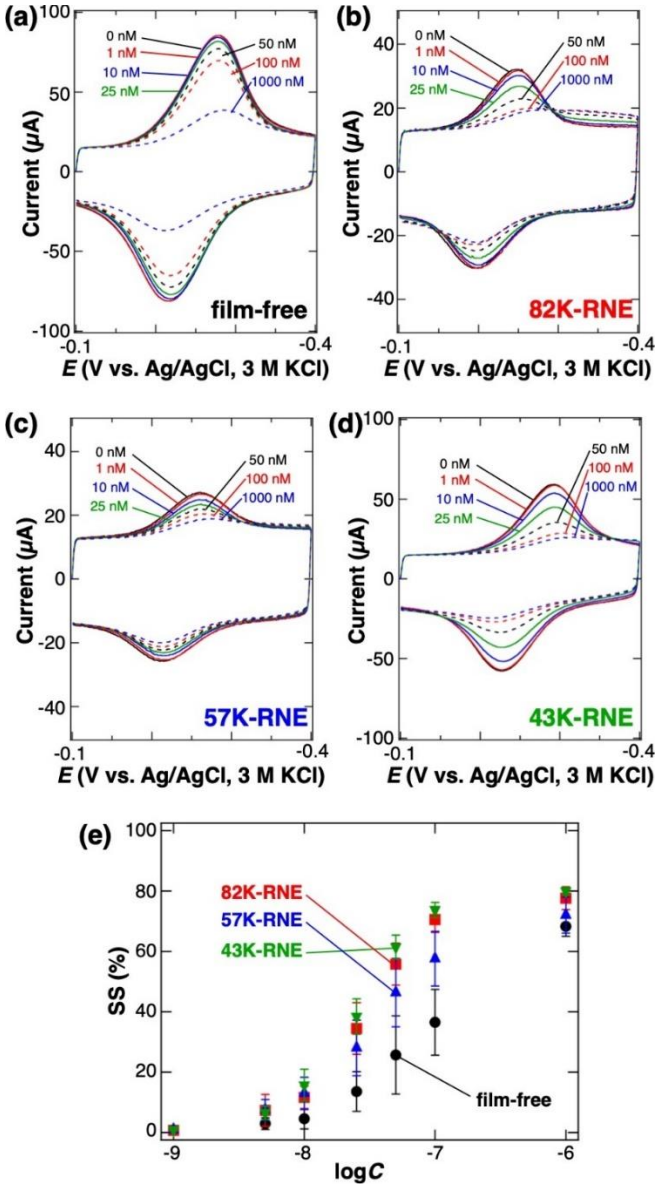

Figure 5.5: Typical cyclic voltammograms (scan rate: 10 V/s) measured at (a) a film-free E-DNA sensor, (b) an 82K-RNE-based E-DNA sensor (30 nm in pore diameter), (c) a 57K-RNE-based E-DNA sensor (20 nm in pore diameter), and (d) a 43K-RNE-based E-DNA sensor (14 nm

in pore diameter) at different target DNA concentrations (0 ~ 1000 nM). These voltammograms were recorded in Phys2 buffer (pH 7.4) at room temperature (*ca*. 25 °C). (e) Signal suppression (%) as a function of the logarithm of target DNA concentration (in mol/L) obtained from four film-free (black circles), four 82K-RNE-based (red squares), four 57K-RNE-based (blue triangles) and five 43K-RNE-based (green inverted triangles) E-DNA sensors. The error bars represent the 80% confidence intervals.

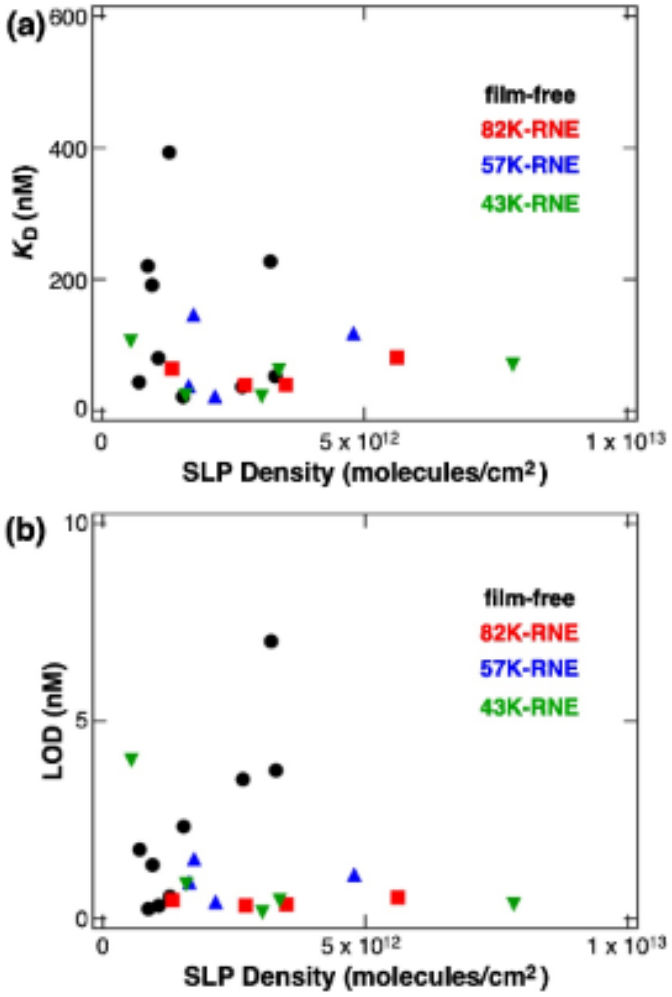

Figure 5.6: Relationships (a) between K_D and SLP density (Γ^*) and (b) between LOD and Γ^* for individual E-DNA sensors. K_D was obtained from Q in cyclic voltammograms at 10 V/s. Of note, five of the nine film-free E-DNA sensors were prepared from SLP solutions of lower concentrations, giving the lower Γ^* and LOD. However, the K_D values of these five sensors were similar to those of the other four sensors with the higher Γ^*, possibly reflecting the limited accuracy of the K_D determination

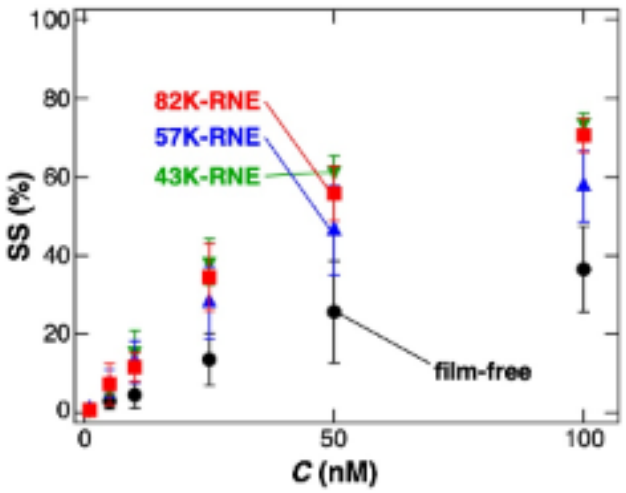

Figure 5.7: Signal suppression (%) as a function of target DNA concentration (in nmol/L) obtained from four film-free (black circles), four 82K-RNE-based (red squares), four 57K-RNE-based (blue triangles) and five 43K-RNE-based (green inverted triangles) E-DNA sensors. The error bars represent the 80% confidence intervals. These calibration curves were recorded in Phys2 buffer (pH 7.4) at room temperature (ca. 25 °C).

5.4.5. Electrochemical Behavior of RNE-Based E-DNA Sensors in Whole Cow Blood. Furthermore, the electrochemical behavior of a RNE-based sensor in undiluted whole cow blood was compared with that of a film-free sensor. The PS-*b*-PMMA-derived nanoporous film of a RNE served as a size-exclusion layer for ferritin.[31] Thus, it was anticipated that interference from relatively large redox-active species in whole blood would be reduced at a RNE-based sensor.

Figure 5.8a shows typical cyclic voltammograms obtained at a film-free sensor in whole cow blood before and after the addition of 1 µM target DNA. An electrocatalytic cathodic current was observed at E < -0.3 V due to redox-active interferents in the blood. In contrast, an 82K-RNE-based sensor with 30-nm nanopores afforded a much smaller electrocatalytic current in the same blood sample (Figure 5.8b). The electrocatalytic process was not facile, as indicated by the observation of similar voltammograms for film-free and RNE-based sensors at 10 V/s (Figure 5.9). These results can be explained by the steric prevention of the entry of redox-active interferents into the nanopores. It is unclear what species gave the electrocatalytic cathodic current, but very

similar voltammograms were observed at gold electrodes modified with MB-tagged DNA in the presence of hemoglobin.[54] Considering the smaller electrocatalytic current at the RNE-based sensor, the interferents could be red blood cells that contain hemoglobin or hemoglobin-incorporating aggregates. Of note, bovine hemoglobin can probably penetrate through the 30-nm nanopores because it is small (*ca*. 7 nm) and almost uncharged (pI ~ 6.9)[54] at pH 7.4.

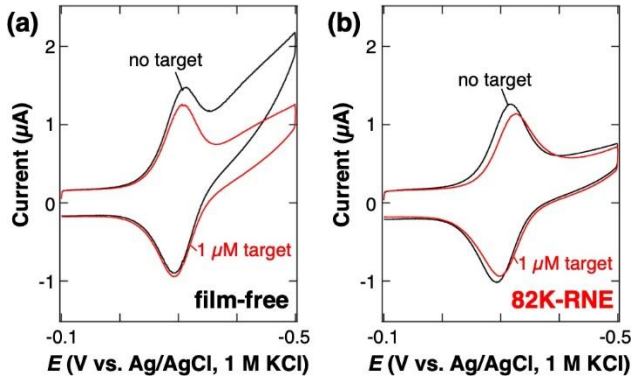

Figure 5.8: Typical cyclic voltammograms (scan rate: 0.1 V/s) measured at (a) a film-free E-DNA sensor and (b) an 82K-RNE-based E-DNA sensor (30 nm in pore diameter) in the absence (black) and presence (red) of 1 µM target DNA. These voltammograms were recorded in whole cow blood at room temperature (*ca*. 25 °C).

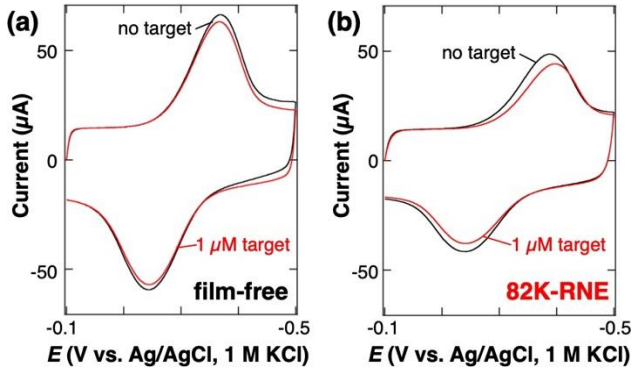

Figure 5.9: Typical cyclic voltammograms (scan rate: 10 V/s) measured at the same E-DNA sensors as those reported in Figure 5.8 in the absence (black) and presence (red) of 1 µM target DNA: (a) Film-free and (b) 82K-RNE-based E-DNA sensors. These voltammograms were recorded in undiluted whole cow blood at room temperature (*ca*. 25 °C).

The electrochemical responses of these sensors to 1 μM target DNA in the blood sample at 10 V/s (Figure 5.9) were much smaller than those in Phys2 buffer (Figure 5.3), possibly because the target DNA was adsorbed onto some components in the blood. The sensors could not be regenerated (data not shown), probably due to nonspecific adsorption of relatively small interferents onto the electrode and/or significant blocking of the nanopores during the regeneration process. In the future, nonspecific adsorption need be reduced by functionalizing the nanopore surface with oligo(ethylene oxide) chains.[31,32] Meanwhile, the film-free sensor gave a larger hybridization-induced change in current response to 1 μM target DNA as compared with the RNE-based sensor (Figure 5.9) due to the electrocatalytic signal amplification.[55] However, the magnitudes of the signal amplification largely varied for different film-free sensors, and thus the electrocatalytic current would be difficult to utilize for DNA quantification.

5.5. Conclusion

This study showed the influences of electrode-attached nanoporous films on the preparation and electrochemical characteristics of folding-based E-DNA sensors. RNEs with different nanopore diameters (14, 20 and 30 nm) were fabricated by coating gold electrodes with PS-*b*-PMMA-derived nanoporous films and were then successfully modified with a self-assembled monolayer comprising a MB-tagged SLP. The resulting RNE-based sensors reversibly exhibited electrochemical responses to 1 μM target DNA in the physiological buffer solution, as with film-free sensors. Interestingly, SLPs within nanopores exhibited larger k_s and k_s' as compared with those of film-free sensors. More importantly, RNE-based E-DNA sensors exhibited lower LOD than film-free sensors. These results were attributable to steric and/or electrostatic interactions with the negatively-charged nanopores that controlled the dynamic flexibility and

orientation of SLPs, in addition to enhanced hybridization within the nanopores. Furthermore, the nanoporous films mitigated the influences of redox-active interferents on electrochemical measurements in whole blood on the basis of size-exclusion mechanism. In conclusion, this study revealed a possibility to improve the performance of folding-based electrochemical sensors using RNEs. However, a number of issues still need to be addressed for the applications of these sensors to point-of-care diagnosis, including the more quantitative understanding of the nanoconfinement effects on sensor performance, the improvement of the reproducibility of sensor fabrication, and the further improvement of detection sensitivity and selectivity.

5.6. References

(1) Fan, C.; Plaxco, K. W.; Heeger, A. J. Electrochemical Interrogation of Conformational Changes as a Reagentless Method for the Sequence-Specific Detection of DNA. *Proc. Natl. Acad. Sci. USA* **2003**, *100*, 9134-9137.

(2) Anne, A.; Bouchardon, A.; Moiroux, J. 3'-Ferrocene-Labeled Oligonucleotide Chains End-Tethered to Gold Electrode Surfaces: Novel Model Systems for Exploring Flexibility of Short DNA Using Cyclic Voltammetry. *J. Am. Chem. Soc.* **2003**, *125*, 1112-1113.

(3) Lubin, A. A.; Plaxco, K. W. Folding-Based Electrochemical Biosensors: The Case for Responsive Nucleic Acid Architectures. *Acc. Chem. Res.* **2010**, *43*, 496-505.

(4) Schoukroun-Barnes, L. R.; Macazo, F. C.; Gutierrez, B.; Lottermoser, J.; Liu, J.; White, R. J. Reagentless, Structure-Switching, Electrchemical Aptamer-Based Sensors. *Annu. Rev. Anal. Chem.* **2016**, *9*, 163-181.

(5) Ferapontova, E. E. DNA Electrochemistry and Electrochemical Sensors for Nucleic Acids. *Annu. Rev. Anal. Chem.* **2018**, *11*, 197-218.

(6) Lai, R. Y.; Seferos, D. S.; Heeger, A. J.; Bazan, G. C.; Plaxco, K. W. Comparison of the Signalling and Stability of Electrochemical DNA Sensors Fabricated from 6- or 11-Carbon Self-Assembled Monolayers. *Langmuir* **2006**, *22*, 10796-10800.

(7) Ricci, F.; Lai, R. Y.; Heeger, A. J.; Plaxco, K. W.; Sumner, J. J. Effect of Molecular Crowding on the Response of an Electrochemical DNA Sensor. *Langmuir* **2007**, *23*, 6827-6834.

(8) Labib, M.; Sargent, E. H.; Kelley, S. O. Electrochemical Methods for the Analysis of Clinically Relevant Biomolecules. *Chem. Rev.* **2016**, *116*, 9001-9090.

(9) Hu, K.; Lan, D.; Li, X.; Zhang, S. Electrochemical DNA Biosensor Based on Nanoporous Gold Electrode and Multifunctional Encoded DNA–Au Bio Bar Codes. *Anal. Chem.* **2008**, *80*, 9124-9130.

(10) Daggumati, P.; Matharu, Z.; Seker, E. Effect of Nanoporous Gold Thin Film Morphology on Electrochemical DNA Sensing. *Anal. Chem.* **2015**, *87*, 8149-8156.

(11) Bin, X.; Sargent, E. H.; Kelley, S. O. Nanostructuring of Sensors Determines the Efficiency of Biomolecular Capture. *Anal. Chem.* **2010**, *82*, 5928-5931.

(12) Su, S.; Wu, Y.; Zhu, D.; Chao, J.; Liu, X.; Wan, Y.; Su, Y.; Zuo, X.; Fan, C.; Wang, L. On-Electrode Synthesis of Shape-Controlled Hierarchical Flower-Like Gold Nanostructures for Efficient Interfacial DNA Assembly and Sensitive Electrochemical Sensing of MicroRNA. *Small* **2016**, *12*, 3794-3801.

(13) Daggumati, P.; Matharu, Z.; Wang, L.; Seker, E. Biofouling-Resilient Nanoporous Gold Electrodes for DNA Sensing. *Anal. Chem.* **2015**, *87*, 8618-8622.

(14) Salamifar, S. E.; Lai, R. Y. Fabrication of Electrochemical DNA Sensors on Gold-Modified Recessed Platinum Nanoelectrodes. *Anal. Chem.* **2014**, *86*, 2849-2852.

(15) Liu, J.; Wagan, S.; Davila Morris, M.; Taylor, J.; White, R. J. Achieving Reproducible Performance of Electrochemical, Folding Aptamer-Based Sensors on Microelectrodes: Challenges and Prospects. *Anal. Chem.* **2014**, *86*, 11417-11424.

(16) Arroyo-Curras, N.; Scida, K.; Ploense, K. L.; Kippin, T. E.; Plaxco, K. W. High Surface Area Electrodes Generated via Electrochemical Roughening Improve the Signaling of Electrochemical Aptamer-Based Biosensors. *Anal. Chem.* **2017**, *89*, 12185-12191.

(17) Kohli, P.; Harrell, C. C.; Cao, Z.; Gasparac, R.; Tan, W.; Martin, C. R. DNA-Functionalized Nanotube Membranes with Single-Base Mismatch Selectivity. *Science* **2004**, *305*, 984-986.

(18) Iqbal, S. M.; Akin, D.; Bashir, R. Solid-State Nanopore Channels with DNA Selectivity. *Nat. Nanotechnol.* **2007**, *2*, 243-248.

(19) Yang, S. Y.; Son, S.; Jang, S.; Kim, H.; Jeon, G.; Kim, W. J.; Kim, J. K. DNA-Functionalized Nanochannels for SNP Detection. *Nano Letters* **2011**, *11*, 1032-1035.

(20) Nguyen, V. K.; Wolff, C.-M.; Seris, J. L.; Schwing, J.-P. Immobilized Enzyme Electrode for Creatinine Determination in Serum. *Anal. Chem.* **1991**, *63*, 611-614.

(21) Higson, S. P. J.; Desal, M. A.; Ghosh, S.; Christie, I.; Vadgama, P. Amperometric Enzyme Electrode Biofouling and Passivation in Blood: Characterisation of Working Electrode Polarisation and Inner Membrane Effects. *J. Chem. Soc., Faraday Trans.* **1993**, *89*, 2847-2851.

(22) Pfeiffer, D.; Scheller, F. W.; Setz, K.; Schubert, F. Amperometric Enzyme Electrodes for Lactate and Glucose Determinations in Highly Diluted and Undiluted Media. *Anal. Chm. Acta* **1993**, *281*, 489-502.

(23) Arrigan, D. W. M. Nanoelectrodes, Nanoelectrode Arrays and their Applications. *Analyst* **2004**, *129*, 1157-1165.

(24) Zoski, C. G.; Wijesinghe, M. Electrochemistry at Ultramicroelectrode Arrays and Nanoelectrode Ensembles of Macro- and Ultramicroelectrode Dimensions. *Isr. J. Chem.* **2010**, *50*, 347-359.

(25) Baker, L. A.; Jin, P.; Martin, C. R. Biomaterials and Biotechnologies Based on Nanotube Membranes. *Crit. Rev. Solid State Mater. Sci.* **2005**, *30*, 183-205.

(26) Ito, T.; Audi, A. A.; Dible, G. P. Electrochemical Characterization of Recessed Nanodisk-Array Electrodes Prepared from Track-Etched Membranes. *Anal. Chem.* **2006**, *78*, 7048-7053.

(27) Perera, D. M. N. T.; Ito, T. Cyclic Voltammetry on Recessed Nanodisk-Array Electrodes Prepared from Track-Etched Polycarbonate Membranes with 10-nm Diameter Pores. *Analyst* **2010**, *135*, 172-176.

(28) Ito, T. Block Copolymer-Derived Monolithic Polymer Films and Membranes Comprising Self-Organized Cylindrical Nanopores for Chemical Sensing and Separations. *Chem.–Asian J.* **2014**, *9*, 2708-2718.

(29) Ito, T.; Ghimire, G. Electrochemical Applications of Microphase-Separated Block Copolymer Thin Films. *ChemElectroChem* **2018**, *5*, 2937-2953.

(30) Menon, V. P.; Martin, C. R. Fabrication and Evaluation of Nanoelectrode Ensembles. *Anal. Chem.* **1995**, *67*, 1920-1928.

(31) Li, Y.; Ito, T. Size-Exclusion Properties of Nanoporous Films Derived from Polystyrene-Poly(methylmethacrylate) Diblock Copolymers Assessed Using Direct Electrochemistry of Ferritin. *Anal. Chem.* **2009**, *81*, 851-855.

(32) Pandey, B.; Tran Ba, K. H.; Li, Y.; Diaz, R.; Ito, T. Electrochemical Study of the Diffusion of Cytochrome c within Nanoscale Pores Derived from Cylinder-Forming Polystyrene-Poly(methylmethacrylate) Diblock Copolymers. *Electrochim. Acta* **2011**, *56*, 10185-10190.

(33) Li, Y.; Maire, H. C.; Ito, T. Electrochemical Characterization of Nanoporous Films Fabricated from a Polystyrene–Poly(methylmethacrylate) Diblock Copolymer: Monitoring the Removal of the PMMA Domains and Exploring the Functional Groups on the Nanopore Surface. *Langmuir* **2007**, *23*, 12771-12776.

(34) Li, Y.; Ito, T. Surface Chemical Functionalization of Cylindrical Nanopores Derived from a Polystyrene–Poly(methylmethacrylate) Diblock Copolymer via Amidation. *Langmuir* **2008**, *24*, 8959-8963.

(35) Vlassiouk, I.; Takmakov, P.; Smirnov, S. Sensing DNA Hybridization via Ionic Conductance through a Nanoporous Electrode. *Langmuir* **2005**, *21*, 4776-4778.

(36) Cheng, M. S.; Toh, C.-S. Novel Biosensing Methodologies for Ultrasensitive Detection of Viruses. *Analyst* **2013**, *138*, 6219-6229.

(37) Fayad, S. J.; Minatti, E.; Soldi, V.; Fort, S.; Labbe, P.; Borsali, R. A Versatile Nanoarray Electrode Produced from Block Copolymer Thin Films for Specific Detection of Proteins. *Polymer* **2017**, *123*, 128-136.

(38) Li, F.; Pandey, B.; Ito, T. Linker-Based Control of Electron Propagation through Ferrocene Moieties Covalently Anchored onto Insulator-Based Nanopores Derived from a Polystyrene-Poly(methylmethacrylate) Diblock Copolymer. *Langmuir* **2012**, *28*, 16496-16500.

(39) Li, F.; Ito, T. Complexation-Induced Control of Electron Propagation Based on Bounded Diffusion through Nanopore-Tethered Ferrocenes. *J. Am. Chem. Soc.* **2013**, *135*, 16260-16263.

(40) Thurn-Albrecht, T.; Steiner, R.; DeRouchey, J.; Stafford, C. M.; Huang, E.; Bal, M.; Tuominen, M.; Hawker, C. J.; Russell, T. P. Nanoscopic Templates from Oriented Block Copolymer Films. *Adv. Mater.* **2000**, *12*, 787-791.

(41) Maire, H. C.; Ibrahim, S.; Li, Y.; Ito, T. Effects of Substrate Roughness on the Orientation of Cylindrical Domains in Thin Films of a Polystyrene-Poly(methylmethacrylate) Diblock Copolymer Studied Using Atomic Force Microscopy and Cyclic Voltammetry. *Polymer* **2009**, *50*, 2273-2280.

(42) Yang, W.; Lai, R. Y. Comparison of the Stem-Loop and Linear Probe-Based Electrochemical DNA Sensors by Alternating Current Voltammetry and Cyclic Voltammetry. *Langmuir* **2011**, *27*, 14669-14677.

(43) Lai, R. Y.; Walker, B.; Stormberg, K.; Zaitouna, A. J.; Yang, W. Electrochemical Techniques for Characterization of Stem-Loop Probe and Linear Probe-Based DNA Sensors. *Methods* **2013**, *64*, 267-275.

(44) White, R. J.; Plaxco, K. W. Exploiting Binding-Induced Changes in Probe Flexibility for the Optimization of Electrochemical Biosensors. *Anal. Chem.* **2010**, *82*, 73-76.

(45) Li, F.; Diaz, R.; Ito, T. Quantitative Investigation of Surface Functionalization of Cylindrical Nanopores Derived from Polystyrene-Poly(methylmethacrylate) Diblock Copolymers. *RSC Adv.* **2011**, *1*, 1732-1736.

(46) Ito, T. Ion-Channel-Mimetic Sensor for Trivalent Cations Based on Self-Assembled Monolayers of Thiol-Derivatized 4-Acyl-5-Pyrazolones on Gold. *J. Electroanal. Chem.* **2001**, *495*, 87-97.

(47) Trasatti, S.; Petrii, O. A. Real Surface Area Measurements in Electrochemistry. *Pure Appl. Chem.* **1991**, *63*, 711-734.

(48) Sato, H.; Wakabayashi, M.; Ito, T.; Sugawara, M.; Umezawa, Y. Potentiometric Responses of Ionophore-Incorporated Bilayer Lipid Membranes with and without Added Anionic Sites. *Anal. Sci.* **1997**, *13*, 437-446.

(49) Laviron, E. General Expression of the Linear Potential Sweep Voltammogram in the Case of Diffusionless Electrochemical Systems. *J. Electroanal. Chem.* **1979**, *101*, 19-28.

(50) Kang, D.; Zuo, X.; Yang, R.; Xia, F.; Plaxco, K. W.; White, R. J. Comparing the Properties of Electrochemical-Based DNA Sensors Employing Different Redox Tags. *Anal. Chem.* **2009**, *81*, 9109-9113.

(51) Levine, I. N. *Physical Chemistry* 4th Ed., McGraw-Hill, New York, 1995.

(52) Ibrahim, S.; Ito, T. Surface Chemical Properties of Nanoscale Domains on UV-Treated Polystyrene–Poly(methyl methacrylate) Diblock Copolymer Films Studied Using Scanning Force Microscopy. *Langmuir* **2010**, *26*, 2119-2123.

(53) Fernandez de Avila, B. E.; Watkins, H. M.; Pingarron, J. M.; Plaxco, K. W.; Palleschi, G.; Ricci, F. Determinants of the Detection Limit and Specificity of Surface-Based Biosensors. *Anal. Chem.* **2013**, *85*, 6593-6597.

(54) Pheeney, C. G.; Guerra, L. F.; Barton, J. K. DNA Sensing by Electrocatalysis with Hemoglobin. *Proc. Natl. Acad. Sci. USA* **2012**, *109*, 11528-11533.

(55) Khan, S.; Gupta, A.; Verma, N. C.; Nandi, C. K. Kinetics of Protein Adsorption on Gold Nanoparticles with Variable Protein Structure and Nanoparticle Size. *J. Chem. Phys.* **2015**, *143*, 164709.Add content here.

Chapter 6 - Characterization of Nanoporous Thin Films from Photocleavable Polystyrene-*b*-Poly(ethylene oxide)

6.1. Contribution of Authors

Dr. Takashi Ito directed the overall project. Dr. Yi Yi (Dept. Chem., Indiana Univ. Bloomington) provided photocleavable PS-*b*-PEO, PS-*hv*-PEO. Dr. Herman Coceancigh established the experimental setup for solvent vapor annealing (SVA). Zeinab Harandizadeh prepared all the samples and obtained all the data shown in this chapter, including ellipsometric thickness, AFM images and fluorescence spectroscopic data.

6.2. Introduction

Diblock copolymers (DBCs) have enticed significant attentiveness due to their spatial structure and valuable technological applications. DBCs consist of two incompatible blocks grafted together through covalently bond. DBCs have a tendency to undergo microphase separation (self-assembly) as a function of composition and form microphase-separated structures with domains in the range of few nanometers to several hundred nanometers, depending on the molecular weight of the polymer and segmental interactions strength between different segments.[1] In another word, the microphase separation process is a thermodynamic process which forms periodic nanostructure. Different morphology including spherical, gyroid, cylindrical or lamellar can be obtained by microphase separation.[2]

One of the DBCs is asymmetric polystyrene-*b*-poly(ethylene oxide) (PS-*b*-PEO). The polymer can be used to prepare a template for the preparation of nanoparticle arrays,[3] a framework for nanoparticle growth,[4] and an insulation layer for the preparation of nanoelectrode ensembles[5]

after undergoing microphase separation. The application of PS-*b*-PEO can be expanded as a nanolithographic mask if PEO blocks are removed through etching.[6] A successful etching process involves the removal of the minor segment selectively. PS-*b*-PEO undergoes self-assembly after spreading on a surface. PS blocks are hydrophobic, while PEO blocks are hydrophilic. When a PS-*b*-PEO solution is spin-coated on a hydrophilic surface at the air/water interface, PS blocks stay in the air and PEO attached to the surface; therefore, the nanostructure of PS-*b*-PEO thin film is formed.[7]

Solvent vapor annealing (SVA) is one of the annealing methods to obtain well-order vertical alignment of microdomains for thin block copolymer films. In this method, a surface coated with a thin block copolymer film is exposed to vapor of one or more solvents in a closed container.[8] In 1998, Albalak et al. reported the application of SVA to improve microdomain alignment in BCP films. In this work, a thin film of poly(styrene)-*b*-poly(butadiene)-*b*-poly(styrene) was exposed to toluene vapor. They showed that a well-ordered nanostructure obtained through SVA was similar to one obtained through thermal annealing; however, they obtained the nanostructure in a significantly shorter time compared with thermal annealing.[9] In the same year, Kim et al. also reported the control of microdomain orientation in thin films of a polystyrene-polybutadiene-polystyrene (SBS) triblock copolymer (30 wt % PS) by controlling solvent evaporation rate during SVA. When the solvent evaporation rate was fast (200 nL/s), the obtained microphase-separated microstructure was highly disordered. The microstructure with fully in-plane PS cylinder was gained when the solvent evaporation rate was very slow (0.2 nL/s).[10] In general, the SVA process can be divided into two steps. In the first step, a BCP thin film on a substrate is exposed to solvent vapor for an extended time. This step leads to the swelling of the

thin film. In the second step, the sample is removed from the solvent vapor atmosphere. This step causes the deswelling of the DBC film due to the evaporation of the solvent from the polymer film.

Kim *et al.*[11] reported the use of SVA to obtain highly-ordered arrays of cylindrical PEO microdomains in a PS-*b*-PEO thin film. They spin-coated PS-*b*-PEO films from its solution on different surfaces. After the spin-coating, nonequilibrium morphology that includes cylindrical PEO domains was obtained on the film surface. However, the cylindrical domains did not reach to the bottom of the film. They exposed the thin films to benzene vapor at room temperature. This step led to the rapid swelling of the thin film. The vertically-oriented cylindrical PEO microdomains with a high degree of lateral order were obtained after removing the sample from the SVA chamber and evaporation of benzene from the film. The cylindrical microdomain morphology obtained at this step is equilibrium morphology. In another word, SVA helps to turn nonequilibrium morphology to equilibrium morphology with a high degree of lateral order.[12] The SVA chamber humidity is another parameter to be considered to get desirable morphology for PEO-base BCPs. For example, poly(ethylene oxide)-*b*-poly(methyl methacrylate)-*b*-polystyrene (PEO-*b*-PMMA-*b*-PS) triblock copolymers (M_{ps} = 32.4 kDa and f_{ps} = 0.77, M_{PMMA} = 6.0 kDa and f_{PMMA} = 0.13, M_{PEO} = 5.0 kDa and f_{PEO} = 0.11) gave cylindrical morphologies parallel to the substrate at humidity less than 70%. Perpendicular PEO cylinders to the substrate surface were obtained when the humidity of the SVA chamber was higher than 70%.[13]

In this chapter, I will summarize my results on the preparation and characterization of photocleavable PS-*b*-PEO (PS-*hv*-PEO) thin films. Specifically, I tried to prepare perpendicular cylindrical PEO domains in thin PS-*hv*-PEO films on gold substrates. SVA was used to improve the order of the domains. The optimization of the solvent was done for SVA to get more uniform domain morphology. After removing the cylindrical PEO domains by a photocleavage reaction, I

functionalized the resulting pore surface having -COOH groups by amidation with an alkyne-terminated amine. I tried different conditions to maximize the reaction yield. I tried to further functionalize the pore surface by click reaction with an azide-tagged fluorescent probe.

6.3. Experimental Section

6.3.1. Chemicals and Materials

Photocleavable PS-*b*-PEO (PS_{226}-*hv*-PEO_{113}: M_n = 23 500 g/mol for PS and 5,200 g/mol for PEO, PEO volume fraction: 0.16) was synthesized by Dr. Yi (Department of Chemistry, Indiana University, Bloomington) and used as received. Toluene (Fisher), hydrochloric acid (HCl; Fisher), 1,1,1,3,3,3-hexamethyldisilazane (Acros), tetrahydrofuran (≥ 99.0%, Aldrich), ethanol (Decon Laboratories) were used as received. Hydroxybenzotriazole (HOBT, TCI), *N*-hydroxysuccinimide (NHS, Acros), 1-ethyl-3-(3-dimethylaminopropyl) carbodiimide hydrochloride (EDC; Chemimpex international), propargylamine (Aldrich), rhodamine 6G (R6G, Aldrich), thionine acetate (Acros), Azide-fluor 545 (λ_{ex} = 546 nm, λ_{em} = 565 nm; Aldrich), L-ascorbic acid (Acros), cupric sulfate pentahydrate ($CuSO_4 \cdot 5H_2O$; Fisher), tris[(1-benzyl-1H1,2,3-triazol-4-yl)methyl]amine (TBTA; Aldrich), 4-(2-hydroxyethyl)-1-piperazineethanesulfonic acid (HEPES, Sigma) and 2-(*N*-morpholino)ethanesulfonic acid (MES, Sigma) were used as received. All aqueous solutions were prepared with water having a resistivity of 18 MΩ (Barnstead Nanopure Systems). Planar Si (100) wafers (p-type) were purchased from University Wafer (South Boston, MA). Premium microscope slides were purchased from Fisher. Gold-coated silicon wafers, which were prepared by sputtering 10 nm of Ti followed by 200 nm of Au onto Si (100) wafers, were purchased from LGA Thin Films (Foster City, CA).

6.3.2. PS-*hv*-PEO Thin Film Preparation

PS-*hv*-PEO-derived nanoporous films (ellipsometric thickness 55-60 nm) were prepared according to a procedure reported previously.[14] Briefly, thin PS-*hv*-PEO films were prepared by spin-coating (2000 rpm, 30 sec) of a dilute toluene solution of the PS-*hv*-PEO (1.5 wt%) on cleaned gold-coated silicon wafer, silicon wafer or glass substrate. Prior to the spin-coating, the substrates were sonicated for 10 min with soap, water, and ethanol, respectively, and then cleaned by a PDC-32G Plasma cleaner system for 10 min. The film-coated substrates underwent SVA using different solvents and different SVA times to improve orientation and order of nanopores. The humidity of the solvent chamber was 70%-80%. After SVA, PEO domains aligned vertically on the film surface. Then, the thin film sample was exposed to a UV lamp. A UV lamp 360 nm was used to optimize irradiation time. The UV irradiation led to the photocleaving reaction of the ONB ester of PS-*hv*-PEO.[15] After removing PEO domains by immersing the sample in methanol/H_2O (8:1) for 3 h,[16] the sample was dried in air. Spectroscopic ellipsometry and AFM were used to evaluate the thickness and surface morphology of the thin film after each step. Figure 6.1 shows the molecular structure of PS-*hv*-PEO before and after exposure to UV light.

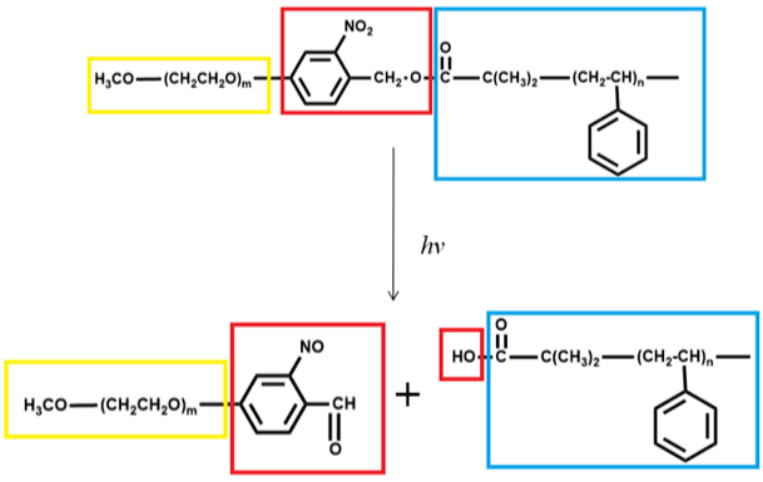

Figure 6.1: Molecular structure of PS-*hv*-PEO before and after exposure to UV light.

6.3.3. Surface Functionalization of PS-*hv*-PEO-Derived Nanopores by Aqueous-Phase Amidation

Amidation of a PS-*hv*-PEO-derived nanoporous film on a substrate was performed under different conditions to attain high reaction yield with short reaction time. All the reaction conditions are explained below.

Method 1:[18] A gold, Si wafer or glass substrate coated with a PS-*hv*-PEO-derived nanoporous film was immersed in an aqueous solution containing EDC (0.2 g/mL) and NHS (0.03 g/mL) in HEPES buffer (0.1 M, pH 7) or phosphate buffer (0.1 M, pH 6) for 7 h while the reaction vial was shaking on a laboratory rocker. The films were then rinsed with HEPES buffer and dipped in an aqueous HEPES buffer (pH 7) containing propargylamine (10 mM) for 24 h with gentle shaking. The samples were rinsed with HEPES buffer and then with water.

Method 2:[19] A gold substrate coated with a PS-*hv*-PEO-derived nanoporous film was incubated in a solution containing propargylamine (25 mM) and HOBT (25 mM) in 0.1 M MES buffer (pH 7.0, 5 mL). Every 12 h, EDC (5 mg) was added into the solution 4 times to reach a total amount of 20 mg EDC. The reaction vial was under the stirring condition for all the reaction time. In the end, the sample was rinsed by ultrapure water for 2 h and dry under vacuum condition.

Method 3:[20] A substrate coated with a PS-*hv*-PEO-derived film was immersed in a solution prepared by mixing 5 mL of ultrapure water, 1.0 ml of MES buffer (500 mM, pH = 6.1) and 2.3 ml of an aqueous NHS solution (50 mg/mL). Under fast shaking, 1.2 mL fresh aqueous EDC solution (10 mg/mL) was added quickly, and the mixture was continually shaken at room temperature for 30 min. The sample was removed from the solution and rinsed thoroughly with 50 mM MES buffer (pH 6.1) to remove excess EDC, NHS, and byproduct. Then the sample was

immersed in 9.0 mL of 50 mM MES buffer (pH 6.1). Aqueous propargylamine solution (10 mg/mL, 1.0 mL) in MES buffer (pH 6.1) was added to the previous solution. After shaking the vial containing the substrate and solution at room temperature for 24 h, the sample was removed and washed with 50 mM MES buffer (pH 6.1) three times to remove unbound propargylamine.

6.3.4. Click Reaction

The amidated sample was used for a click reaction. The sample was dipped in a solution (1 mL) containing 0.01 mM Azide-fluor 545, 0.25 mM TBTA, 0.25 mM $CuSO_4$ and 0.25 ml L-ascorbic acid for 2.5 h. Next, the sample was rinsed with ultrapure water and dried with air. Fluoromax was used to measure the fluorescence intensity of dye molecules attached to the nanoporous thin film. For this purpose, the film-coated substrate was inserted in a plastic or quartz cuvette. One side of a cuvette was covered by a black paper with a hole to fix an illumination area for the excitation light. The intensity of Azide-fluor 545 was measured using 546 nm as an excitation wavelength and 565 nm as an emission wavelength.

6.3.5. Determination of Free Surface –COOH Density *via* Cation Exchange

A nanoporous film before or after amidation was immobilized at the bottom of a cell used in our previous study.[18] An O–ring (0.80 cm in diameter) was put between the top of the surface and upper part of the cell to determine the area of a film exposed to the dye solution. The cell was filled with an aqueous solution of R6G (1 mM) or ethanol solution of thionine acetate (10 mM) overnight. Then, the cell was washed with ultrapure water when R6G was used as a probe or ethanol when thionine acetate was used as a probe. The substrate was separated from the cell and washed with ultrapure water or ethanol three times for R6G and thionine acetate, respectively. The

washed substrate was dipped in 0.01 M HCl solution (2.00 mL) or 0.01 M HCl (1:1 mixture of water and ethanol, 2 mL)[21] for 2 h for R6G and thionine acetate, respectively. Spectrofluorometry was used to get emission spectra of these probes in the HCl solution. Before running spectrofluorometry measurement, standard solutions of R6G or thionine were prepare for getting a calibration curve. The ultrapure water was used to prepare standard solution for R6G (1 mM, 5 mM, 10 mM, 15 mM, 25 mM, 75 mM), while a 1: 1 mixture of ethanol and water including 0.01 M HCl was used to prepare thionine acetate standard solution (1 mM, 5 mM, 10 mM, 15 mM, 2 5mM, 75 mM). For R6G, the excitation wavelength was set at 525 nm and the fluorescence intensity at 550 nm was measured to determine the concentration of R6G in standard solutions and cations released to the HCl solution. For thionine acetate, the excitation wavelength was set at 594 nm as an excitation wavelength and fluorescence intensity at 620 nm (thionine) was used for measuring the concentration of thionine acetate in standard solution and thionine acetate cations released to the HCl solution.[18]

6.4. Result and Discussion

6.4.1. Solvent Vapor Annealing (SVA) with Different Solvent Conditions.

PS-*hv*-PEO thin films on substrates underwent SVA with different solvents for different SVA times to get vertically-oriented uniform cylindrical domains. Different solvents with different ratios including toluene, THF, THF:H_2O (10:1), THF:H_2O (5:1), benzene/H_2O were used for SVA. H_2O was selected as a solvent because it is selective for PEO. PS chain starts to aggregate to minimize the interaction between PS and H_2O while PEO concentration gets maximize on the surface to increase interaction between PEO and H_2O. Toluene is good solvent for PS and PEO; however, it is slightly selective for PS. Toluene leads to swelling of the PS chain.[6] Benzene and

THF are good solvents for PS and PEO but has PS-preferential affinity.[22] THF It is good to mention that the Hildebrand solubility parameter is 24.3 $MPa^{0.5}$, 18.61 $MPa^{0.5}$, 18.3 $MPa^{0.5}$, 18.8 $MPa^{0.5}$, 18.5 $MPa^{0.5}$ and 48 $MPa^{0.5}$ for PEO, PS, toluene, benzene, THF and H_2Orespectively.[23]

Also, for each solvent, optimization of SVA time was carried out. AFM was used to evaluate the surface morphology of each thin film after SVA. Figure 6.2 shows AFM images for a thin PS-*hv*-PEO film before SVA (Figure 6.2a) and after SVA with toluene as a SVA solvent at different SVA times, followed by the removal of PEO domains. Figure 6.2.a shows nonequilibrium phase separation due to the evaporation of the solvent during the spin coating step (Figure 6.2a). The use of toluene as a solvent for SVA did not give any vertically-oriented cylindrical pores after SVA for 30 min (Figure 6.2b), 60 min (Figure 6.2c), and even 150 min (Figure 6.2d).

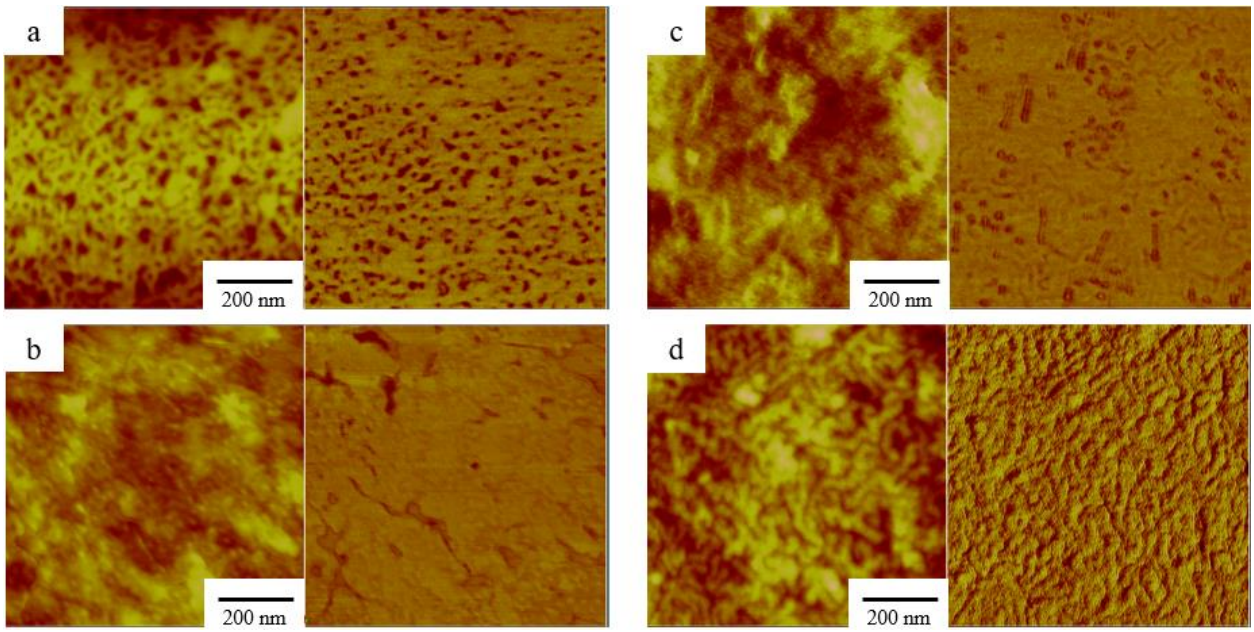

Figure 6.2: Tapping-mode AFM height (left) and phase (right) images (1 × 1 μm^2; Δz = 10 nm) of the surfaces of PS-*hv*-PEO films on silicon substrates (a) after the spin coating, and after SVA with toluene for (b) 30 min, (c) 60 min, and (d) 150 min, followed by UV/methanol treatment (UV wavelength 360 nm).

Figure 6.3 shows AFM images for PS-*hv*-PEO after SVA with THF as a solvent. It is clear that THF is not suitable as a SVA solvent for PS-*hv*-PEO because vertically-oriented pores were not obtained after SVA for 1h (Figure 6.3a), and 4h (Figure 6.2c). For 2.5 h (Figure 6.3b), the size of vertically-oriented pores was not uniform after SVA. Also, it seems some of the pores connected to each other and made channels.

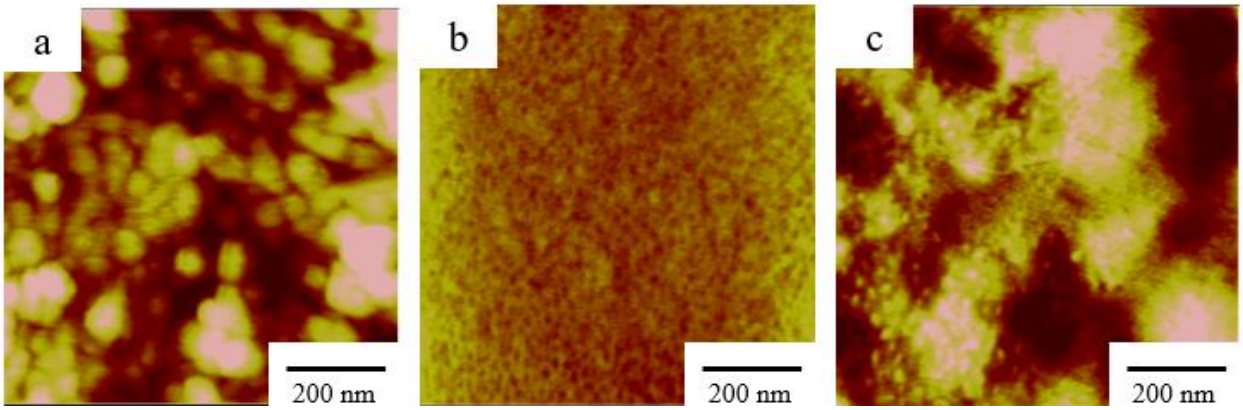

Figure 6.3: Tapping-mode AFM images (1 × 1 μm^2; Δz = 10 nm) of the surfaces of PS-*hv*-PEO films on silicon substrates after SVA with THF for (a) 1 h, (b) 2.5 h, and (c) 4 h, followed by UV/methanol treatment (UV wavelength 360 nm).

The formation of pores was observed when THF:H_2O (10:1) was used for SVA (Figure 6.4a). However, pores were not cylindrical or uniform. Also, pore structures were distorted after longer SVA time (3 h and 4 h; Figure 6.4c and d), possibly due to the extensive swelling of the thin films by the solvent.

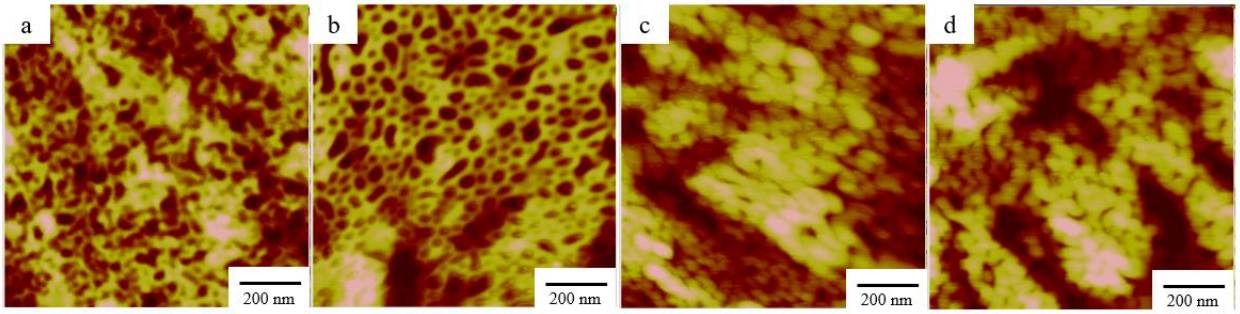

Figure 6.4: Tapping-mode AFM images (1 × 1 μm^2; Δz = 10 nm) of the surfaces of PS-*hv*-PEO films on silicon substrates (a) after the spin coating and after SVA with THF/H_2O (10:1) for (b) 3 h, (c) 5 h, and (d) 7 h, followed by UV/methanol treatment (UV wavelength 360 nm).

The use of THF:H_2O (5:1) as a SVA solvent gave vertically-oriented cylindrical pores after SVA for 60 min (Figure 6.5a) and 150 min (Figure 6.5b). However, the size of the domains was not uniform. In addition, the pore size and morphology shown in Figure 6.5 were not reproducibly obtained.

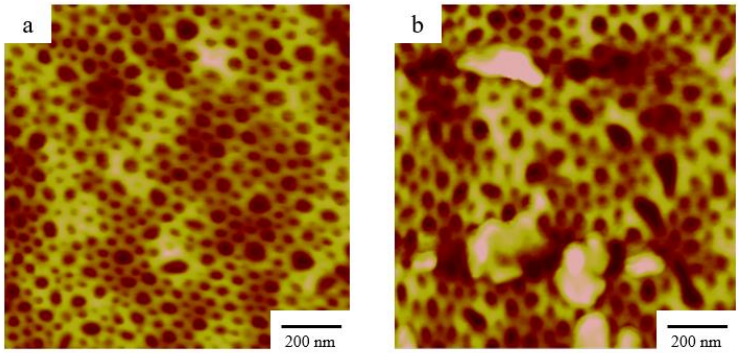

Figure 6.5: Tapping-mode AFM images (1 × 1 μm^2; Δz = 10 nm) of the surfaces of PS-*hv*-PEO films on silicon substrates after SVA with THF/H_2O (5:1) for (a) 60 min and (b) 150 min, followed by UV/methanol treatment (UV wavelength 360 nm).

In contrast to these solvent systems, benzene:H_2O, in which benzene and water were placed in separate containers within a desiccator, gave the more uniform, vertically-oriented domains (Figure 6.6). The relative humidity of SVA chamber was 70-80% when SVA was done. Interestingly, benzene:H_2O gave smaller domains (19.9, 19.1, and 18.5 nm in diameter after SVA

for 1, 2, and 3 h, respectively). Longer SVA time from 60 min to 180 min improved domain formation (Figure 6.6a,b,c); therefore, 180 min was selected as an appropriate SVA time (Figure 6.6c).

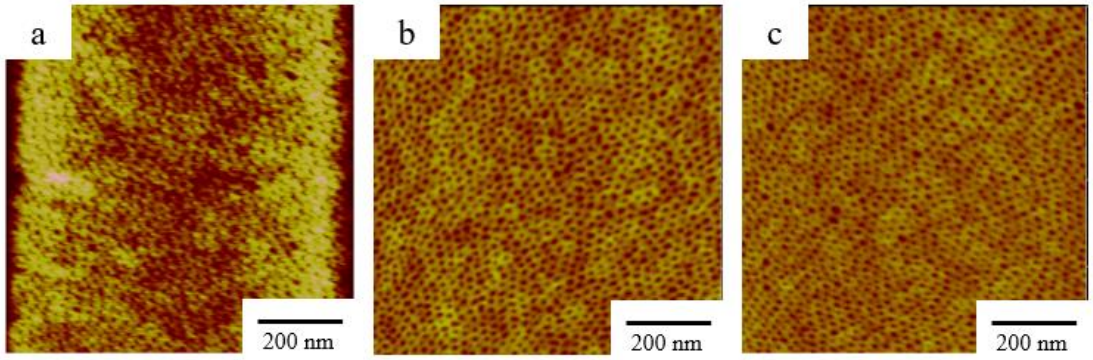

Figure 6.6: Tapping-mode AFM images (1 × 1 μm^2; Δz = 50 nm) of the surfaces of PS-*hv*-PEO films on gold substrates after SVA with benzene/H_2O for (a) 60 min, (b) 120 min, and (c) 180 min, followed by UV/methanol treatment for 30 min (UV wavelength 360 nm).

Figure 6.7 showed AFM images of thin films on gold substrates after spin-coating (Figure 6.7a), after SVA with benzene/H_2O for 3h (Figure 6.7b) and after UV irradiation for 30 min and then treatment with methanol/H_2O. This SVA condition gave vertically-oriented pores on the film surface.

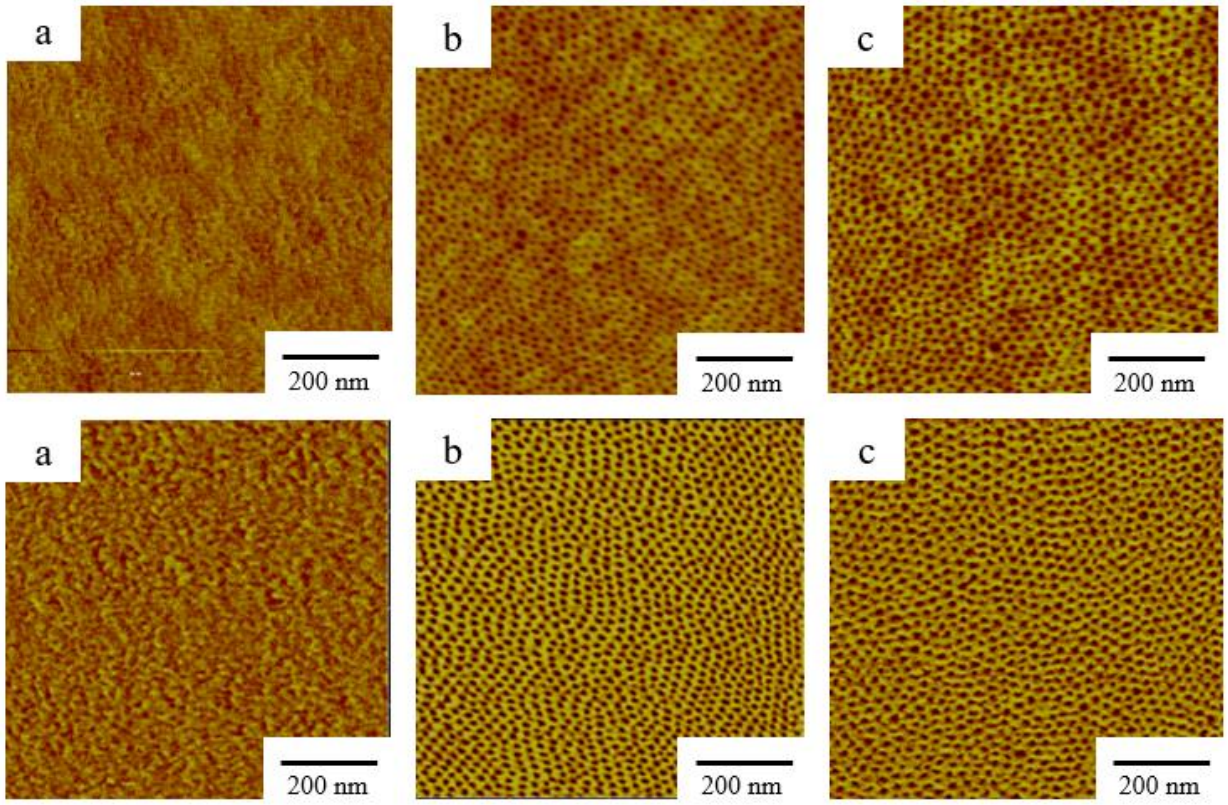

Figure 6.7: Tapping-mode height (upper) and phase (lower) images (1×1 μm^2; Δz = 50 nm) of the surfaces of PS-*hv*-PEO films on gold substrates (a) after spin coating, (b) after SVA with benzene/H_2O for 180 min, and (c) after UV/methanol treatment (UV wavelength 360 nm).

Ellipsometry was used to measure film thickness before, after SVA, and after PEO removal. The results are shown in Table 6.1. Film thickness slightly increased after SVA possibly because the film was swollen by a solvent, and then decreased after UV/methanol treatment because of the successful removal of PEO. It was difficult to get any conclusions about the refractive index of the thin film after spin coating, SVA, and UV/methanol treatment.

Table 6-1: Thickness, *d* (nm) and refractive index (*n*) of PS-*hv*-PEO thin film on gold substrates. Data shown in this table were obtained from 7 different samples.

After spin coating		**After SVA for 3h**		**After PEO removal**	
d (nm)	*n*	*d (nm)*	*n*	*d (nm)*	*n*
58.66	1.573	59.82	1.568	54.75	1.577
61.20	1.576	61.85	1.572	57.34	15.76

60.46	1.574	60.71	1.575	56.83	1.570
60.23	1.572	60.71	1.569	56.67	1.566
59.92	1.575	60.67	1.572	56.60	1.570
59.10	1.575	59.75	1.570	55.78	1.573
60.18	1.571	60.38	1.569	56.44	1.570

6.4.2. An Aqueous-Phase Amidation of PS-*hv*-PEO-Derived Nanoporous Thin Film

Different amidation methods were examined for the surface of PS-*hv*-PEO-derived nanoporous thin film on silicon and gold substrates. These films are expected to have surface-COOH groups as a result of a photocleavage reaction (Figure 6.8).[17]

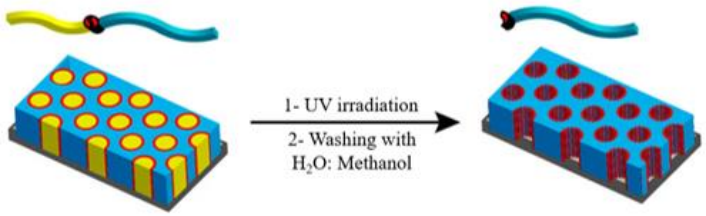

Figure 6.8: Photocleavage reaction of an *o*-nitrobenzyl ester group (shown in red) in PS-*hv*-PEO upon exposure to UV light, followed by the removal of the PEO microdomains shown in yellow. The reaction scheme is shown in Figure 6.1. Reprinted with permission from ref (17), Copyright © 2015, American Chemical Society

The reaction yield of amidation was explored by measuring -COOH density using cation exchange processes before and after an amidation reaction according to a procedure reported previously (Figure 6.9).[18] Figure 6.9 also shows probe molecules used to measure and calculate -COOH density before and after modification.

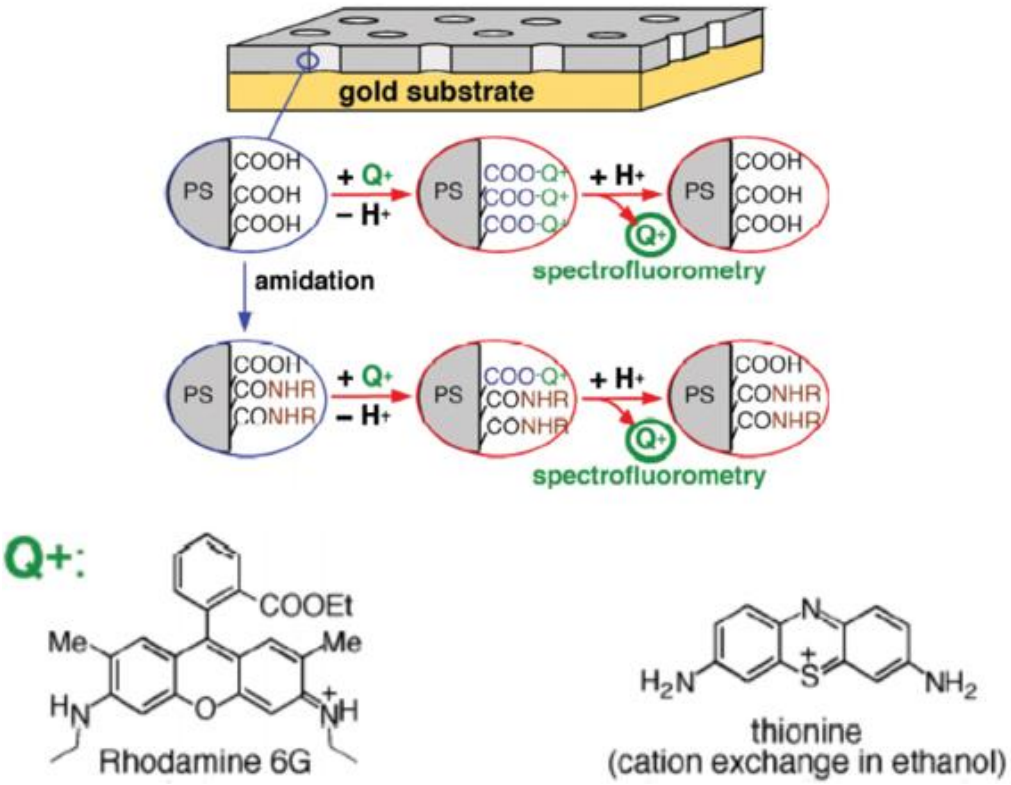

Figure 6.9: Experimental procedures used to measure surface free -COOH groups via ion-exchange proves with probe cations (Q^+).[18] A decrease in the amount of Q^+ as a result of amidation was used to quantify the yield of surface amidation.

The density of free -COOH molecule was calculated using Equation. 6.1.

$$(-COOH\ density) = \frac{the\ amount\ of\ probe\ cations\ released\ to\ 0.01\ M\ HCl}{\Pi dLN} \quad \text{(eq. 6.1)}$$

where *d* is pore diameter, *L* is pore length, and *N* is the total number of pores. Here, *d* (= 25 nm) and *N* obtained from AFM images and *L* is assumed to be equal to the ellipsometric thickness of a film after SVA[24] *N* was calculated from pore density from AFM images (945 pores/μm^2) and the diameter of an O-ring that defined the contact area with the solutions. This equation can be applied under two assumptions. First, the surface -COOH groups are completely deprotonated at pH 7, and each deprotonated -COOH group forms an ion pair with one probe cation. Second, all the domains

have a cylindrical shape with uniform length and diameter that are oriented from top of the film through the surface of substrate.[25]

At the beginning, silicon substrates were used to prepare thin films. Unfortunately, a PS-*hv*-PEO-derived thin film detached from the substrate after the amidation procedure with EDC/NHS in HEPES buffer (Figure 6.10). Indeed, the ellipsometric thickness of the thin films decreased to 3-9 nm after amidation (Table 6.2) due to the weak adhesion of the thin films to the silicon substrates. The results confirm the detachment of the thin films after amidation reaction.

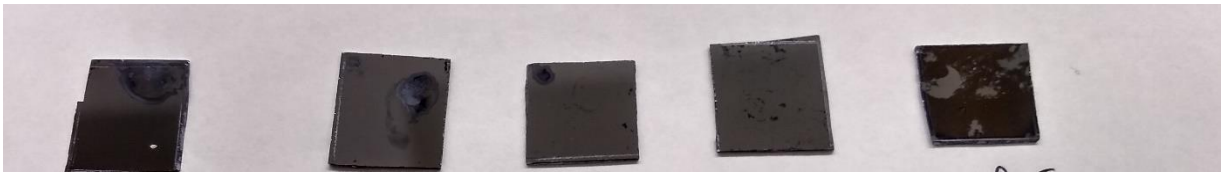

Figure 6.10: Picture of PS-*hv*-PEO-derived nanoporous films on Si substrates after the amidation procedure with EDC/NHS in HEPES (pH 7).

Table 6-2 Thickness, *d* (nm), and refractive index, *n*, of PS-*hv*-PEO-derived nanoporous thin film on silicon for three different samples.

After spin coating		**After SVA**		**After PEO removal**		**After amidation**
d(nm)	*n*	*d(nm)*	*n*	*d*(nm)	*n*	*d* (nm)
61.64	1.594	62.26	1.593	58.86	1.574	3.38
62.57	1.592	62.96	1.597	60.05	1.582	8.97
63.60	1.605	64.29	1.606	60.59	1.591	5.0

Thus, the surfaces of Si substrates were treated with 1,1,1,3,3,3-hexamethyldisilazane vapor to improve the adhesion of the thin films. The cleaned substrates were exposed to the vapor of 1,1,1,3,3,3-hexamethyldisilazane for 20 minutes at room temperature. Then they were heated in an oven at 120◦C for 1 hour.[26] However, the treatment did not improve the adhesion of thin films. Therefore, gold substrates were examined for further experiments. PS-*hv*-PEO-derived

nanoporous thin films on gold substrates were stable under three amidation conditions examined here. Table 6-3 shows -COOH density measured before and after amidation with propargylamine.

Table 6-3: COOH density on PS-*hv*-PEO-derived nanoporous thin films after amidation

-COOH density/nm^2 before amidation	-COOH density/nm^2 after amidation	Reaction yield%	Method
0.252	0.0852	66.2	1[a]
0.252	0.101	59.7	1[a]
0.252	0.105	58.4	1[a]
0.212	0.068	67.7	1[a]
0.212	0.091	57.0	2[a]
0.212	0.074	65.1	2[a]
0.130	0.077	40.3	3[a]
0.101	0.039	61.3	1 (HEPES buffer)[b]
0.034	0.0185	45.6	1 (PBS buffer)[b]
0.026	0.021	21.0	1 (PBS buffer)[b]

[a]: -COOH measurement was performed using thionine acetate as a dye
[b]: -COOH measurement was performed using Rhodamine 6G as a dye

The free -COOH group density of a thin film was measured using Rhodamine 6G or thionine acetate. The calculated -COOH density using Rhodamine 6G (0.014 ± 0.002 -COOH/nm^2) was lower than that using thionine acetate (0.30 ± 0.08 -COOH/nm^2). Figure 6.9 shows the molecular structure of Rhodamine 6G which has an iminium ion. The proton of iminium ion does not participate in acid-base equilibrium. It means Rhodamine 6G is cationic regardless of pH in aqueous solution.[27] The lower -COOH density obtained with Rhodamine 6G might be due to the use of water for the ion-exchange and washing process. Therefore, thionine acetate was used to calculate -COOH density. The -COOH density (0.30 ± 0.08 -COOH/nm^2) obtained at the intact films, which was smaller than that obtained for PS-*b*-PMMA-derived nanoporous films,[18] was close to that estimated from the number of ONB groups in the PS-*hv*-PEO films. Method 1 gave 58-68% yield in HEPES buffer, in contrast to 21-45% in phosphate buffer. Phosphate buffer is

commonly used for amidation reaction, but gave a low reaction yield because of the reduction of the half-life of EDC.[28] Method 2 gave 57-65% yield, and Method 3 gave 40% yield. Thus. Method 1 was selected to prepare alkyne-functionalized samples for click reaction.

6.4.3. Click Reaction

Alkyne-functionalized nanoporous films on gold substrates were used to modify the surface with fluorescent molecules by click reaction, Cu(I)-catalyzed azide-alkyne cycloaddition. After click reaction with Azide-fluor 545, samples were dried in the air, and then were used for recording fluorescence emission spectra to verify the immobilization of the fluorescent probe onto the samples. However, no specific peak related to Azide-fluor 545 emission was observed around 565 nm in the presence and absence of Cu(I) (Figure 6.11), indicating the inefficient immobilization of the dye on the film. Figure 6.11 shows a peak around 575-580 nm in all of the spectra that are related to the gold substrate or cuvette. It is necessary to optimize the conditions for the click reaction and also for fluorescence measurements.

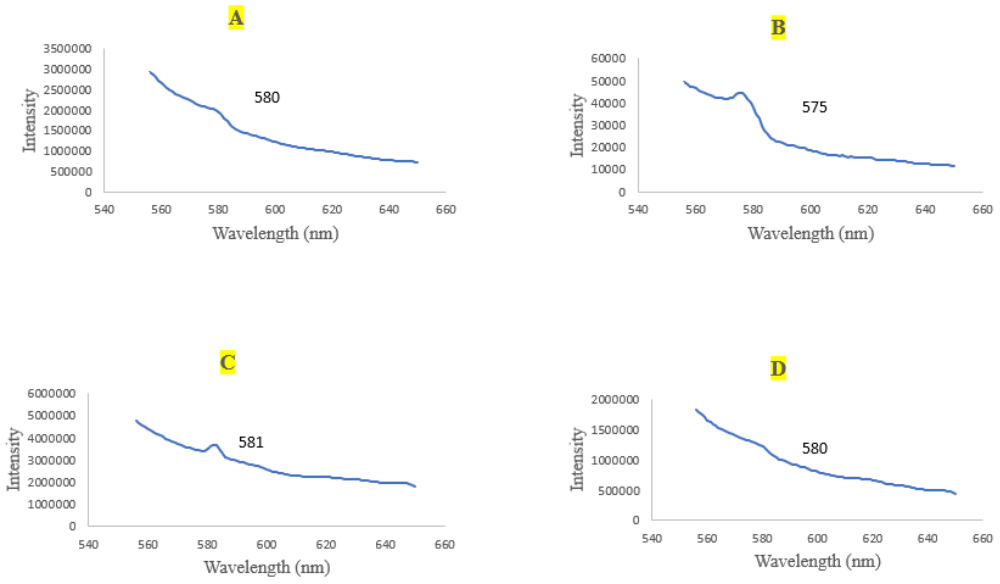

Figure 6.11: Fluorescence spectra of A) a cleaned gold substrate, B) a gold substrate coated with nanoporous thin film, C) a film-coated substrate after click reaction with Cu(I), and D) a film-coated substrate after click reaction without Cu(I). The excitation wavelength was 546 nm.

Also, the effect of the solvent on fluorescence spectra of carboxytetramethylrhodamine (TAMRA) fluorophore was assessed. 2 µL TAMRA (0.046 M) was added to different solvents including methanol (10 ml), ethanol (10 ml), H_2O (10 ml), methanol:ethanol (1:1) (5ml: 5ml), methanol:H_2O (1:1) (5ml: 5ml), and ethanol:H_2O (1:1) (5ml: 5ml). The resulting fluorescence spectra of the fluorophore are shown in Figure 6.12. It is clear that there is a solvatochromic effect for TAMRA in different solvents or solvent mixtures. The shift of emission wavelength is shown in Table 6-4. It can be concluded that the fluorescence emission shift is significant from water to organic solvents, but is relatively small for the organic solvents.

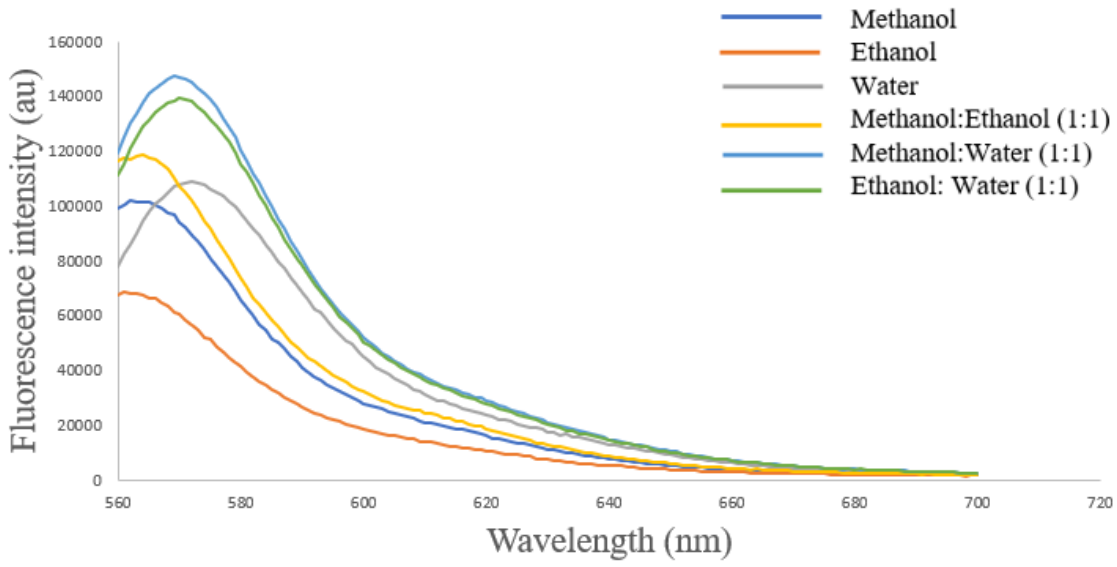

Figure 6.12: Fluorescence emission spectra of TAMRA in different solvents (excitation wavelength 554 nm).

Table 6-4: Maximum emission wavelength (nm) of TAMRA in different solvents

Solvent	Max Emission wavelength (nm)
Methanol	562
Ethanol	561
Water	572
Methanol: Ethanol (1:1)	564
Methanol: Water (1:1)	569
Ethanol: Water (1:1)	570

Here, TAMRA was used to assess the effect of solvent on fluorescence spectra because TAMRA is fluorophore of Azide-fluor 545. It means the resulte which is obtaiebd by TAMRA is same as the result which can be found using Azide-fluor 545. Figure 6.13 shows the chemical structure of TAMRA and assess the effect of solvent on fluorescence spectra because TAMRA is fluorophore of Azide-fluor 545.

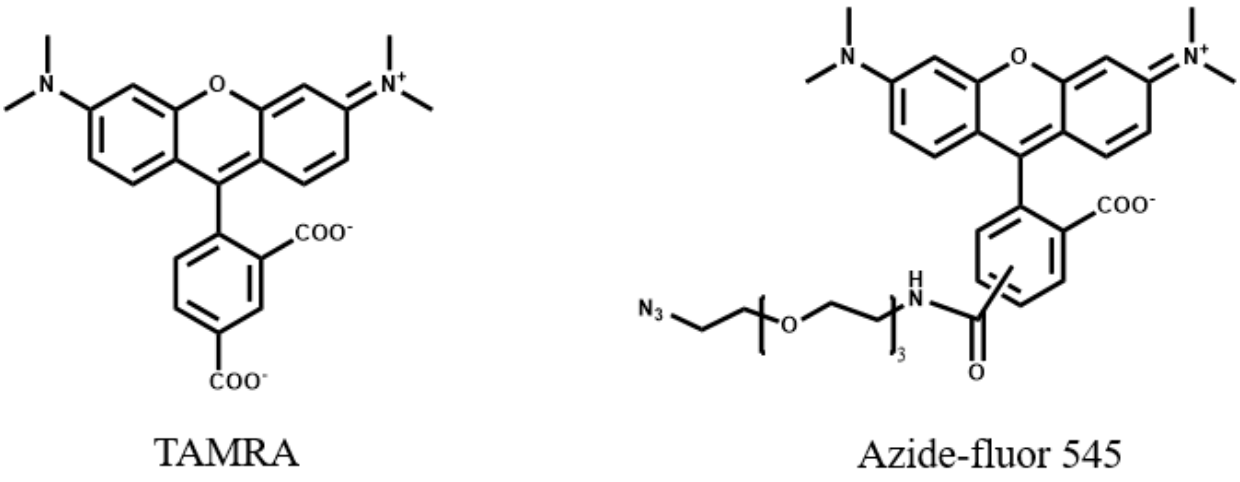

Figure 6.13: Chemical structure of TAMRA and Azide-fluor 545

6.5. Conclusion

PS-*hv*-PEO gave vertically-oriented PEO microdomains by SVA with benzene/H_2O for 3 hours. Subsequent UV/MeOH treatment gave nanoporous structures with the surface -COOH groups (apparent density: 0.30 ± 0.08 -COOH/nm^2). However, the low density of -COOH groups suggests that the pores did not penetrate through the film. Amidation of the surface -COOH groups with propargylamine was highest (58-68%) by the use of EDC/NHS in HEPES buffer (pH 7). It is required to optimize click reaction conditions for functionalizing the resulting alkyne on the polymer surface. Ultimately, the nanoporous films derived from PS-*hv*-PEO will be used to investigate the effects of polymer-based nanospaces on chemical recognition with novel receptor molecules for the future development of separation membranes and chemical sensors.

6.6. Reference

(1) Matsushita, Y. Microphase Separation (of Block Copolymers). In *Encyclopedia of Polymeric Nanomaterials*; Kobayashi, S., Müllen, K., Eds.; Springer Berlin Heidelberg: Berlin, Heidelberg, 2014; pp 1–6. https://doi.org/10.1007/978-3-642-36199-9_149-1.

(2) Mai, Y.; Eisenberg, A. Self-Assembly of Block Copolymers. *Chem. Soc. Rev.* **2012**, *41* (18), 5969–5985. https://doi.org/10.1039/C2CS35115C.

(3) Jeng, U.-S.; Sun, Y.-S.; Lee, H.-Y.; Hsu, C.-H.; Liang, K. S.; Yeh, S.-W.; Wei, K.-H. Binding Effect of Surface-Modified Cadmium Sulfide on the Microstructure of PS-b-PEO Block Copolymers. *Macromolecules* **2004**, *37* (12), 4617–4622. https://doi.org/10.1021/ma049722r.

(4) Kim, D. H.; Kim, S. H.; Lavery, K.; Russell, T. P. Inorganic Nanodots from Thin Films of Block Copolymers. *Nano Lett.* **2004**, *4* (10), 1841–1844. https://doi.org/10.1021/nl049063w.

(5) Hirota, K.; Tajima, K.; Hashimoto, K. Facile Preparation of Nanoelectrode Ensembles Using Amphiphilic Block Copolymer Film. *Langmuir* **2005**, *21* (25), 11592–11595. https://doi.org/10.1021/la0522810.

(6) Mokarian-Tabari, P.; Collins, T. W.; Holmes, J. D.; Morris, M. A. Brushless and Controlled Microphase Separation of Lamellar Polystyrene-b-Polyethylene Oxide Thin Films for Block Copolymer Nanolithography. *Journal of Polymer Science Part B: Polymer Physics* **2012**, *50* (13), 904–909. https://doi.org/10.1002/polb.23082.

(7) Park, S.; Lee, D. H.; Xu, J.; Kim, B.; Hong, S. W.; Jeong, U.; Xu, T.; Russell, T. P. Macroscopic 10-Terabit–per–Square-Inch Arrays from Block Copolymers with Lateral Order. *Science* **2009**, *323* (5917), 1030–1033. https://doi.org/10.1126/science.1168108.

(8) Sinturel, C.; Vayer, M.; Morris, M.; Hillmyer, M. A. Solvent Vapor Annealing of Block Polymer Thin Films. *Macromolecules* **2013**, *46* (14), 5399–5415. https://doi.org/10.1021/ma400735a.

(9) Albalak, R. J.; Capel, M. S.; Thomas, E. L. Solvent Swelling of Roll-Cast Triblock Copolymer Films. *Polymer* **1998**, *39* (8), 1647–1656. https://doi.org/10.1016/S0032-3861(97)00497-7.

(10) Kim, G.; Libera, M. Morphological Development in Solvent-Cast Polystyrene−Polybutadiene−Polystyrene (SBS) Triblock Copolymer Thin Films. *Macromolecules* **1998**, *31* (8), 2569–2577. https://doi.org/10.1021/ma971349i.

(11) Kim, S. H.; Misner, M. J.; Xu, T.; Kimura, M.; Russell, T. P. Highly Oriented and Ordered Arrays from Block Copolymers via Solvent Evaporation. *Advanced Materials* **2004**, *16* (3), 226–231. https://doi.org/10.1002/adma.200304906.

(12) Kim, S. H.; Misner, M. J.; Xu, T.; Kimura, M.; Russell, T. P. Highly Oriented and Ordered Arrays from Block Copolymers via Solvent Evaporation. *Advanced Materials* **2004**, *16* (3), 226–231. https://doi.org/10.1002/adma.200304906.

(13) Bang, J.; Kim, B. J.; Stein, G. E.; Russell, T. P.; Li, X.; Wang, J.; Kramer, E. J.; Hawker, C. J. Effect of Humidity on the Ordering of PEO-Based Copolymer Thin Films. *Macromolecules* **2007**, *40* (19), 7019–7025. https://doi.org/10.1021/ma0710737.

(14) Harandizadeh, Z.; Ito, T. Block Copolymer-Derived Recessed Nanodisk-Array Electrodes as Platforms for Folding-Based Electrochemical DNA Sensors. *ChemElectroChem* **2019**, *6* (22), 5627–5632. https://doi.org/10.1002/celc.201901562.

(15) Zhao, H.; Gu, W.; Sterner, E.; Russell, T. P.; Coughlin, E. B.; Theato, P. Highly Ordered Nanoporous Thin Films from Photocleavable Block Copolymers. *Macromolecules* **2011**, *44* (16), 6433–6440. https://doi.org/10.1021/ma201416b.

(16) Kang, M.; Moon, B. Synthesis of Photocleavable Poly(Styrene-Block-Ethylene Oxide) and Its Self-Assembly into Nanoporous Thin Films. *Macromolecules* **2009**, *42* (1), 455–458. https://doi.org/10.1021/ma802434g.

(17) Altinpinar, S.; Zhao, H.; Ali, W.; Kappes, R. S.; Schuchardt, P.; Salehi, S.; Santoro, G.; Theato, P.; Roth, S. V.; Gutmann, J. S. Distortion of Ultrathin Photocleavable Block Copolymer Films during Photocleavage and Nanopore Formation. *Langmuir* **2015**, *31* (32), 8947–8952. https://doi.org/10.1021/acs.langmuir.5b00750.

(18) Li, F.; Diaz, R.; Ito, T. Quantitative Investigation of Surface Functionalization of Cylindrical Nanopores Derived from Polystyrene-Poly(Methylmethacrylate) Diblock Copolymers. *RSC Adv.* **2011**, *1* (9), 1732–1736. https://doi.org/10.1039/C1RA00471A.

(19) Rzayev, J.; Hillmyer, M. A. Nanochannel Array Plastics with Tailored Surface Chemistry. *J. Am. Chem. Soc.* **2005**, *127* (38), 13373–13379. https://doi.org/10.1021/ja053731d.

(20) Jiang, K.; Schadler, L. S.; Siegel, R. W.; Zhang, X.; Zhang, H.; Terrones, M. Protein Immobilization on Carbon Nanotubes via a Two-Step Process of Diimide-Activated Amidation. *J. Mater. Chem.* **2004**, *14* (1), 37–39. https://doi.org/10.1039/B310359E.

(21) Papra, A.; Hicke, H.-G.; Paul, D. Synthesis of Peptides onto the Surface of Poly(Ethylene Terephthalate) Particle Track Membranes. *Journal of Applied Polymer Science* **1999**, *74* (7), 1669–1674. https://doi.org/10.1002/(SICI)1097-4628(19991114)74:7<1669::AID-APP9>3.0.CO;2-W.

(22) Kim, S. H.; Misner, M. J.; Xu, T.; Kimura, M.; Russell, T. P. Highly Oriented and Ordered Arrays from Block Copolymers via Solvent Evaporation. *Advanced Materials* **2004**, *16* (3), 226–231. https://doi.org/10.1002/adma.200304906.

(23) Barton, A. F. M. *Handbook of Polymer-Liquid Interaction Parameters and Solubility Parameters*; CRC Press, 1990.

(24) Li, F.; Diaz, R.; Ito, T. Quantitative Investigation of Surface Functionalization of Cylindrical Nanopores Derived from Polystyrene-Poly(Methylmethacrylate) Diblock Copolymers. *RSC Adv.* **2011**, *1* (9), 1732–1736. https://doi.org/10.1039/C1RA00471A.

(25) Ibrahim, S.; Ito, T. Surface Chemical Properties of Nanoscale Domains on UV-Treated Polystyrene−Poly(Methyl Methacrylate) Diblock Copolymer Films Studied Using Scanning Force Microscopy. *Langmuir* **2010**, *26* (3), 2119–2123. https://doi.org/10.1021/la902677e.

(26) Harandizadeh, Z.; Xie, J.; Moore, M. M.; Hohn, K. L.; Ito, T. Sensitization with Stannous Acetate in Dimethyl Sulfoxide for Silver Electroless Deposition. *J. Electrochem. Soc.* **2018**, *165* (10), D488–D493. https://doi.org/10.1149/2.1391810jes.

(27) Gilliland, J. W.; Yokoyama, K.; Yip, W. T. Effect of Coulombic Interactions on Rotational Mobility of Guests in Sol−Gel Silicate Thin Films. *Chem. Mater.* **2004**, *16* (20), 3949–3954. https://doi.org/10.1021/cm049250v.

(28) Gilles, M. A.; Hudson, A. Q.; Borders, C. L. Stability of Water-Soluble Carbodiimides in Aqueous Solution. *Analytical Biochemistry* **1990**, *184* (2), 244–248. https://doi.org/10.1016/0003-2697(90)90675-Y.

Chapter 7 - General Conclusion

This dissertation explores different applications of two diblock copolymers. PS-*b*-PMMA derived thin film with cylindrical horizontal domains was used as a substrate for silver electroless deposition using $Sn(OAc)_2$/DMSO (0.5 mM). The results showed that successful preferential silver deposition was achieved on the nanoscale ridges of the polymer after 10 minutes electroless deposition using very low concentration of $Sn(OAc)_2$ (0.5 mM) in DMSO solution (as a sensitizer). However, in contrast, Ag-NPs were negligibly deposited on the polymer film sensitized with 0.5 mM $SnCl_2$/DMSO. In other word, we were able to get deposited silver nanoparticles using very low concentration of sensitization solution ($Sn(OAc)_2$/DMSO). If we wanted to get successful silver deposition using conventional sensitization solution ($SnCl_2/H_2O$) we needed to use higher Sn(II) concentration ($\geq$ 5 mM). The result can be explained by the reduced formation of tin(II) hydroxide in the DMSO solution, enabling the more efficient use of the Sn(II) for the sensitization, and by the incorporation of Sn(II) in the solvent-swollen surface of the thin film. This sensitization method is simple, fast and cost-effective, and applicable for the deposition of other metals such as gold and palladium. The ELD method can be used to deposit silver or gold nanoparticles for preparing surface-enhanced Raman scattering-active substrates. SERS is a sensitive technique to detect a trace concentration of adsorbed analyte.

In the second project, we prepared folding-based E-DNA sensors using gold substrates coated with thin nanoporous films derived from PS-*b*-PMMA. We investigated the effects of electrode coating with a thin film (30 nm thick) with vertically-oriented cylindrical nanopores on sensor performance. The sensors were fabricated by immobilizing a stem-loop DNA probe with a terminal methylene blue (MB) tag on the underlying gold surface. Cyclic voltammetry was used to measure the faradaic currents of the MB tag before and after adding complementary target DNA.

Electron transfer rate constant before (k_s) and after (k_s') hybridization with target DNA was larger for film-coated sensors than that for film-free sensors. This result was explained by the confinement of DNA molecules inside the nanopores, which restricted the motion of DNA molecules. More importantly, the limit of detection was improved using film-coated sensors comparing to film-free sensors. The improvement was attributed to the restricted flexibility of the DNA probes by electrostatic interactions with the negatively charged nanopore surface due to the deprotonation of the surface -COOH groups. We tried to use the film-coated sensors (30 nm in pore diameter) for measurements in real whole blood. Our results suggest that the nanopores of the thin film could sterically exclude relatively large interfering species, but not smaller redox-active species. Today, biosensors are considered as essential tools in the areas of clinical diagnostics, and our sensor platform may be applicable for such purposes. However, further improvements are necessary. For example, further modification of the nanopore surface should be explored to enhance the electrostatic exclusion of charges species for the use of the sensors in an undiluted blood sample. The reproducibility of the sensor response must be improved significantly, and miniaturizing the sensor should be considered.

In the last project, nanoporous thin films were prepared from PS-*hv*-PEO. A thin PS-*hv*-PEO film underwent SVA using benzene/H_2O with 70-80% humidity for 3 h to obtain vertically oriented PEO microdomains on the film surface. The thin film was irradiated by UV light (360 nm) for 30 min to photocleave the ONB group, and washed film in methanol:H_2O (8:1) to remove the PEO. AFM images showed the formation of vertically oriented cylindrical nanopores (25 nm in diameter), but the apparent -COOH density values indicated that the nanopores did not penetrate through the film. The yield of aqueous-phase amidation for the surface -COOH groups with propargylamine was 58-68%. The resulting alkyne-decorated nanopores can be further

functionalized using click reaction. Unfortunately, immobilization of Azide-fluor 545 on the nanopore surface was unclear. Azide-fluor 545 will be used as a probe to evaluate the physical environment of the nanopores based on its solvatochromic property.